arXiv:1102.3353v2 [q-bio.NC] 17 Feb 2011

Symmetry-based analysis of the coordinated optimization of visual cortical maps

Lars Reichl[1,2,3,4,*], Dominik Heide[1,5], Siegrid Löwel[3,6], Justin C. Crowley[7], Matthias Kaschube[8], Fred Wolf[1,2,3,4*]
1 Max-Planck-Institute for Dynamics and Self-Organization, Göttingen, Germany
2 Bernstein Center for Computational Neuroscience, Göttingen, Germany
3 Bernstein Focus Neurotechnology, Göttingen, Germany
4 Faculty of Physics, Georg-August University, Göttingen, Germany
5 Frankfurt Institute of Advanced Studies, Frankfurt, Germany
6 School of Biology, Georg-August University, Göttingen, Germany
7 Carnegie Mellon University, Department of Biological Sciences, Pittsburgh PA, USA
8 Physics Department and Lewis-Sigler Institute, Princeton University, Princeton NJ, USA
∗ **E-mail: reichl@nld.ds.mpg.de; fred-wl@nld.ds.mpg.de**

Abstract

In the primary visual cortex of primates and carnivores, functional architecture can be characterized by maps of various stimulus features such as orientation preference (OP), ocular dominance (OD), direction preference, spatial frequency, and retinotopy. It is a long-standing question in theoretical neuroscience whether the observed maps should be interpreted as optima of a specific energy functional that summarizes the design principles of cortical functional architecture. Because the existence of such an optimization principle should be inferred from the biological data, the optimization approach to explain cortical functional architecture raises the following questions: i) Is there a model independent way to analyze the coordinated organization of cortical maps predicted by a general optimization principle? ii) What are the genuine ground states of candidate energy functionals and how can they be calculated with precision and rigor? iii) How do differences in the energy functional impact on the observable map structure and conversely what can be learned about the underlying optimization principle from observations of map structures? To answer these questions we developed a general dynamical systems approach to the combined optimization of visual cortical maps of OP and another scalar feature such as OD or spatial frequency preference. Based on basic symmetry assumptions we obtain a comprehensive phenomenological classification of possible inter-map coupling energies and examine four representative examples: A low and a high order gradient-type coupling energy as well as a low and high order product-type coupling energy. A rigorous evaluation of the coordinated optimization hypothesis is particularly demanded by recent evidence that the functional architecture of orientation columns follows a set of universal quantitative laws [1]. We systematically assess whether these or similar laws can result from the coordinated optimization of orientation columns with other feature maps. OP maps are characterized by singularities, called pinwheel centers [2]. We show that all coupling energies above a critical inter-map coupling strength predict spatially periodic and pinwheel-rich OP maps which represent energetic ground states i.e. global optima of the system. Each individual coupling energy leads to a different class of OP solutions with different correlations among the maps such that inferences about the optimization principle from map layout appear possible.

Introduction

Neurons in the primary visual cortex are selective to a multidimensional set of visual stimulus features, including visual field position, contour orientation, ocular dominance, direction of motion, and spatial frequency. In many mammals, these response properties form spatially complex, two-dimensional patterns called visual cortical maps. The functional advantage of a two dimensional mapping of stimulus selectivities is currently unknown [3,4]. What determines the precise spatial organization of these maps? It is a plausible hypothesis that natural selection should shape visual cortical maps to build efficient representations of visual information improving the 'fitness' of the organism. Cortical maps are therefore often viewed as optima of some cost function. For instance, it has been proposed that cortical maps optimize the cortical wiring length [5,6] or represent an optimal compromise between stimulus coverage and map continuity [7–12]. If map structure was largely genetically determined map structure might be optimized through genetic variation and Darwinian selection on an evolutionary timescale. Optimization may, however, also occur during the ontogenetic maturation of the individual organism for instance by the activity-dependent refinement of neuronal circuits. If such an activity-dependent refinement of cortical architecture realizes an optimization strategy its outcome should be interpreted as the convergence towards a ground state of a specific energy functional. This hypothesized optimized functional, however, remains currently unknown. As several different functional maps coexist in the visual cortex candidate energy functionals are expected to reflect various response properties in the visual cortex. Cortical maps, in fact, are not independent of each other and various studies proposed a coordinated optimization of different feature maps [7,8,10–17]. Coordinated optimization appears consistent with the observed distinct spatial relationships between different maps such as the tendency of iso-orientation lines to intersect OD borders perpendicularly or the preferential positioning of orientation pinwheels at locations of maximal eye dominance [12,18–23]. Specifically these geometric correlations have thus been proposed to indicate the optimization of a cost function given by a compromise between stimulus coverage and continuity [7–12], see however [24].

Visual cortical maps are often spatially complex patterns that can contain defect structures such as point singularities and line discontinuities (fractures) [2,25–30]. It is conceivable that this spatial complexity arises from geometric frustration resulting from the coordinated optimization of several feature maps in which not all inter-map interactions can be simultaneously satisfied [31–35]. In many optimization models, however, the resulting map layout is spatially not complex or lacks some of the basic features such as topological defects [5,31,32,36,37]. In other studies coordinated optimization was reported to preserve defects that would otherwise decay [31]. An attempt to rigorously study the hypothesis that the structure of cortical maps is explained by an optimization process thus raises a number of questions: i) Is there a model independent approach to analyze the simultaneous organization of cortical maps predicted by such a general optimization principle? ii) What are the genuine ground states of such hypothetical energy functionals and how can they be calculated with precision and rigor? iii) How do different choices of energy functionals impact on the predicted map structure and conversely what can be learned about the underlying optimization principle from observations of map structures? If theoretical neuroscience was able to answer these questions with greater confidence, the interpretation and explanation of visual cortical architecture could build on a more solid foundation than available. To start laying such a foundation, we examine how symmetry principles constrain the form of optimization models and introduce a formalism to analyze map optimization independent of the specific energy functional assumed. Minima of a given energy functional can be found by gradient descent which is naturally represented by a dynamical system describing a formal time evolution of the maps. Response properties in visual cortical maps are arranged in repetitive modules of a typical spatial length called hypercolumns. Optimization models that reproduce this typical length scale are therefore effectively pattern forming systems. In the theory of pattern formation, it is well known that symmetries play a crucial role [38,39]. Some symmetries are widely considered biologically plausible for cortical maps, for instance the invariance under spatial translations and rotations or a global shift of orientation preference [40–42]. Here, we show that such symmetries and an approach that utilizes the analogy between map optimization and pattern forming systems can open up a novel and systematic approach to the coordinated optimization of visual cortical representations.

A recent study found strong evidence for a common design in functional architecture of orientation columns [1]. Different species, widely separated in evolution, share a universal set of quantities such as the average pinwheel density or the distribution of minimal pinwheel distances. Such universal laws can be reproduced in a self-organization model if long-range neuronal interactions are dominant [1]. However, it is unclear whether the common design is a result of intrinsic OP properties or whether it can result from interactions with other feature maps. We therefore also examine whether the coordinated optimization of the OP map and another feature map can reproduce the quantitative laws defining the common design.

The presentation of our study is organized in three parts. In **part I**, we introduce a formalism to analyze the coordinated optimization of complex and real valued scalar fields. Complex valued fields can represent for instance orientation preference (OP) or direction preference maps [43, 44]. Real valued fields may represent for instance ocular dominance (OD) [45], spatial frequency maps [18, 46] or ON-OFF segregation [47]. We construct several optimization models such that an independent optimization of each map in isolation results in a regular stripe pattern. A model-free, symmetry-based analysis of potential optimization principles that couple the real and complex valued fields provides a comprehensive overview of conceivable coordinated optimization models and identifies representative forms of coupling energies. For analytical treatment of the optimization problem we adapt a perturbation method from pattern formation theory called weakly nonlinear analysis [48–51]. This method reduces the dimensionality of the system and leads to amplitude equations as an approximate description of the system. We identify a limit in which inter-map interactions become unidirectional. In this limit, one can neglect the backreaction of the complex map on the layout of the co-evolving scalar feature map. We show how to treat low and high order versions of inter-map coupling energies which enter at different order in the perturbative expansion.

In **part II**, we apply the derived formalism by calculating optima of four representative examples of coordinated optimization models and examine how they impact on the resulting map layout. For concreteness, we illustrate the coordinated optimization of visual cortical maps for the most widely studied example of a complex OP map and a real feature map such as the OD map. In particular, we address the problem of pinwheel stability in OP maps [31, 52]. OP maps are characterized by pinwheels, regions in which columns preferring all possible orientations are organized around a common center in a radial fashion [2]. As shown previously, many theoretical models of visual cortical development and optimization fail to predict OP maps possessing stable pinwheels [5, 31, 32, 36]. The OP maps we obtained as optima of different optimization principles are therefore analyzed for the occurrence of pinwheels. We show that in case of the low order energies, a strong inter-map coupling will typically lead to OP map suppression, causing the orientation selectivity of all neurons to vanish. In contrast, for the high order versions, orientation selectivity is preserved for arbitrarily strong inter-map coupling. For all considered optimization models, we identify stationary solutions of the resulting dynamics and mathematically demonstrate their stability. We further calculate phase diagrams as a function of the inter-map coupling strength and the amount of overrepresentation of certain stimuli of the co-evolving scalar feature map. We show that the optimization of any of the analyzed coupling energies can lead to spatially relatively complex patterns. Moreover, in case of OP maps, these patterns are pinwheel-rich. The phase diagrams, however, differ for each considered coupling energy, in particular leading to coupling energy specific ground states. We therefore thoroughly analyze the spatial layout of energetic ground states and in particular their geometric inter-map relationships. Our analysis identifies a apparently general condition for pinwheel-rich OP optima namely a bias in the response properties of the co-evolving scalar feature map.

In **part III**, we complement our analytical results by numerical studies and characterize the dynamics of coordinated optimization models. In particular, we study the kinetics and conditions of pinwheel crystallization and the creation of pinwheels from a pinwheel-free initial pattern. This process is a general signature of systems in which a pinwheel-rich state corresponds to the energetic ground state and can be easily assessed in more complex models that evade analytical treatment. We further explore the impact of inter-map wavelength differences, as observed in certain species, on the structure of predicted optima. Finally, we extend the presented models to explore the coordinated optimization of more than two feature maps.

Results

Part I: Modeling the coordinated optimization of multiple maps

The response properties of neurons in the visual cortex can be described by two-dimensional scalar order parameter fields which are either complex valued or real valued. A complex valued field $z(\mathbf{x})$ can for instance describe OP or direction preference of a neuron located at position $\mathbf{x}$. A real valued field $o(\mathbf{x})$ can describe for instance OD or the spatial frequency preference. Although we introduce a model for the coordinated optimization of general real and complex valued order parameter fields we consider $z(\mathbf{x})$ as the field of OP and $o(\mathbf{x})$ as the field of OD throughout this article. In this case, the pattern of preferred stimulus orientation ϑ is obtained by

$$\vartheta(\mathbf{x}) = \frac{1}{2}\arg(z). \tag{1}$$

The modulus $|z(\mathbf{x})|$ is a measure of the selectivity at cortical location $\mathbf{x}$.

OP maps are characterized by so-called *pinwheels*, regions in which columns preferring all possible orientations are organized around a common center in a radial fashion. The centers of pinwheels are point discontinuities of the field $\vartheta(\mathbf{x})$ where the mean orientation preference of nearby columns changes by 90 degrees. Pinwheels can be characterized by a topological charge q which indicates in particular whether the orientation preference increases clockwise or counterclockwise around the pinwheel center,

$$q_i = \frac{1}{2\pi}\oint_{C_i} \nabla\vartheta(\mathbf{x}) d\mathbf{s}\,, \tag{2}$$

where C_i is a closed curve around a single pinwheel center at $\mathbf{x}_i$. Since ϑ is a cyclic variable in the interval $[0,\pi]$ and up to isolated points is a continuous function of $\mathbf{x}$, q_i can only have values

$$q_i = \frac{n}{2}\,, \tag{3}$$

where n is an integer number [53]. If its absolute value $|q_i| = 1/2$, each orientation is represented only once in the vicinity of a pinwheel center. In experiments, only pinwheels with a topological charge of $\pm 1/2$ are observed, which are simple zeros of the field $z(\mathbf{x})$.

OD maps can be described by a real valued two-dimensional field $o(\mathbf{x})$, where $o(\mathbf{x}) < 0$ indicates ipsilateral eye dominance and $o(\mathbf{x}) > 0$ contralateral eye dominance of the neuron located at position $\mathbf{x}$. The magnitude indicates the strength of the eye dominance and thus the zeros of the field correspond to the borders of OD.

In this article, we interpret visual cortical maps as optima of some energy functional E. The time evolution of these maps can be described by the gradient descent of this energy functional. The field dynamics thus takes the form

$$\begin{aligned} \partial_t\, z(\mathbf{x},t) &= F[z(\mathbf{x},t), o(\mathbf{x},t)] \\ \partial_t\, o(\mathbf{x},t) &= G[z(\mathbf{x},t), o(\mathbf{x},t)], \end{aligned} \tag{4}$$

where $F[z,o]$ and $G[z,o]$ are nonlinear operators given by $F[z,o] = -\frac{\delta E}{\delta \bar{z}}$, $G[z,o] = -\frac{\delta E}{\delta o}$. The system then relaxes towards the minima of the energy E. The convergence of this dynamics towards an attractor is assumed to represent the process of maturation and optimization of the cortical circuitry. Various biologically detailed models have been cast to this form [9, 31, 54].

All visual cortical maps are arranged in repetitive patterns of a typical wavelength Λ. We splitted the energy functional E into a part that ensures the emergence of such a typical wavelength for each map and

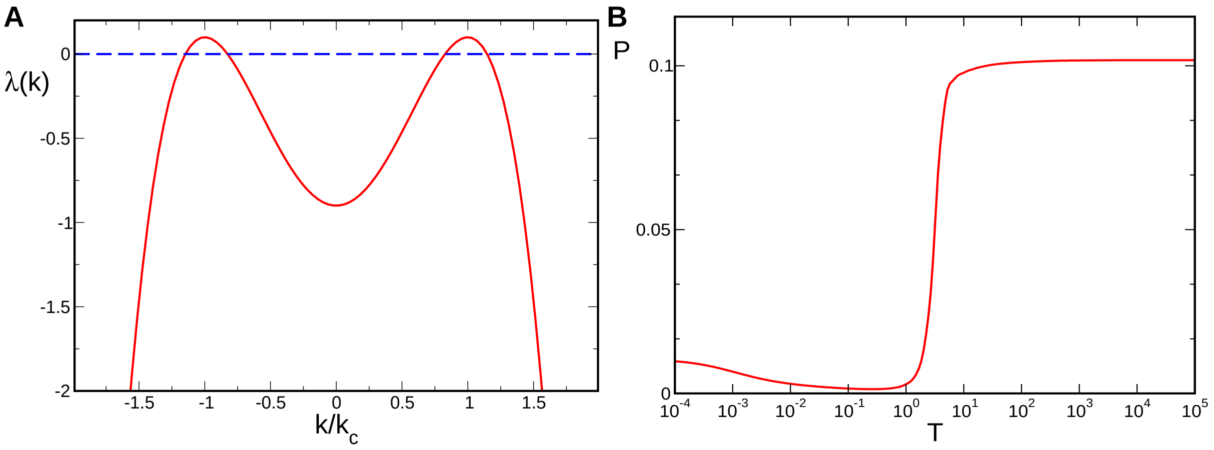

Figure 1. Swift-Hohenberg equation, **A** Cross section through the spectrum $\lambda(k)$ of the Swift-Hohenberg operator Eq. (8), $r = 0.1$. **B** Time evolution of the Power Eq. (9).

into a part which describes the coupling among different maps. A well studied model reproducing the emergence of a typical wavelength by a pattern forming instability is of the Swift-Hohenberg type [38,55]. Many other pattern forming systems occurring in different physical, chemical, and biological contexts (see for instance [48–51]) have been cast into a dynamics of this type. Its dynamics in case of the OP map is of the form

$$\partial_t\, z(\mathbf{x},t) = \hat{L} z(\mathbf{x},t) - |z|^2 z\,, \tag{5}$$

with the linear Swift-Hohenberg operator

$$\hat{L} = r - \left(k_c^2 + \Delta\right)^2\,, \tag{6}$$

$k_c = 2\pi/\Lambda$, and $N[z(\mathbf{x},t)]$ a nonlinear operator. The energy functional of this dynamics is given by

$$E = -\int d^2x \left(\overline{z}(\mathbf{x})\hat{L}z(\mathbf{x}) - \frac{1}{2}|z(\mathbf{x})|^4\right)\,. \tag{7}$$

In Fourier representation, $\hat{L}$ is diagonal with the spectrum

$$\lambda(k) = r - \left(k_c^2 - k^2\right)^2\,. \tag{8}$$

The spectrum exhibits a maximum at $k = k_c$, see Fig. 1(a). For $r < 0$, all modes are damped since $\lambda(k) < 0$, $\forall k$ and only the homogeneous state $z(\mathbf{x}) = 0$ is stable. This is no longer the case for $r > 0$ when modes on the *critical circle* $k = k_c$ acquire a positive growth rate and now start to grow, resulting in patterns with a typical wavelength $\Lambda = 2\pi/k_c$. Thus, this model exhibits a supercritical bifurcation where the homogeneous state looses its stability and spatial modulations start to grow.

While the linear part of the dynamics establishes a typical wavelength the nonlinearity in the dynamics leads to the selection of the final pattern. The time $T = rt$ is given in units of the intrinsic timescale which is associated with the growth rate of the linear part Eq. (6). Considering the time evolution of Eq. (5) initialized with a random OP map and low selectivity several different stages of the dynamics can be distinguished. The linear part forces modes on the critical circle to grow with rate r while strongly suppressing modes off the critical circle, see Fig. 1**A**. The OP map becomes more and more ordered in this linear phase as one dominant wavelength is selected. The total power of the field is given by

$$P(t) = \langle |z(\mathbf{x},t)|^2\rangle_{\mathbf{x}}\,, \tag{9}$$

where $\langle\rangle_{\mathbf{x}}$ denotes spatial average. The time dependence of the power reflects the different growth rates among modes. The time evolution of the power is depicted in Fig. 1**B**. Initially, the power decreases slightly due to the suppression of modes outside the circle of positive growth rate. At $T \approx 1$ there is a rapid increase and then a saturation of the power. The amplitudes of the Fourier modes reach their stationary values and $P \propto r$. At this stage of the evolution the influence of the nonlinear part is comparable to that of the linear part. Once the modes saturate the phase of nonlinear competition between the active modes along with a reorganization of the structure of the OP map starts. The competition between active modes leads to pattern selection. The final pattern then consists of distinct modes in Fourier space [38, 56]. Once the active modes are selected a relaxation of their phases takes place.

Inter-map coupling can influence the time evolution on all stages of the development depending on whether this coupling affects only the nonlinear part or also the linear one. When incorporating additional maps into the system in all cases we rescaled the dynamics by the bifurcation parameter of the OP map i.e. $T = r_z t$. The coupled dynamics we considered is of the form

$$\begin{aligned} \partial_t \, z(\mathbf{x},t) &= \hat{L}_z \, z(\mathbf{x},t) - |z|^2 z - \frac{\delta U}{\delta \overline{z}} \\ \partial_t \, o(\mathbf{x},t) &= \hat{L}_o \, o(\mathbf{x},t) - o^3 - \frac{\delta U}{\delta o} + \gamma \,, \end{aligned} \tag{10}$$

where $\hat{L}_{\{o,z\}} = r_{\{o,z\}} - \left(k^2_{c,\{o,z\}} + \Delta\right)^2$, and γ is a constant. To account for the species differences in the wavelengths of the pattern we chose two typical wavelengths $\Lambda_z = 2\pi/k_{c,z}$ and $\Lambda_o = 2\pi/k_{c,o}$. The dynamics of $z(\mathbf{x},t)$ and $o(\mathbf{x},t)$ is coupled by interaction terms which can be derived from a coupling energy U. In the uncoupled case this dynamics leads to pinwheel free OP stripe patterns.

Symmetries constrain inter-map coupling energies

How many inter-map coupling energies U exist? Using a phenomenological approach the inclusion and exclusion of various terms has to be strictly justified. We did this by symmetry considerations. The constant γ breaks the inversion symmetry $o(\mathbf{x}) = -o(\mathbf{x})$ of inputs from the ipsilateral ($o(\mathbf{x}) < 0$) or contralateral ($o(\mathbf{x}) > 0$) eye. The inter-map coupling energy U was assumed to be invariant under this inversion. The primary visual cortex shows no anatomical indication that there are any prominent regions or directions parallel to the cortical layers [40]. Besides invariance under translations $\hat{T}_{y} z(\mathbf{x}) = z(\mathbf{x} - \mathbf{y})$ and rotations $\hat{R}_\phi z(\mathbf{x}) = z(R^{-1}_\phi \mathbf{x})$ of both maps we required that the dynamics should be invariant under orientation shifts $z(\mathbf{x}) \to e^{\imath\vartheta} z(\mathbf{x})$. Note, that the assumption of shift symmetry is an idealization that uncouples the OP map from the map of visual space [57]. Numerous optimization and developmental models have been proposed that exhibit this symmetry. A general coupling energy term can be expressed by integral operators which can be written as a Volterra series

$$E = \sum_{u=u_o+u_z}^{\infty} \int \prod_{i=1}^{u_o} d^2x_i \, o(\mathbf{x}_i) \prod_{j=u_o+1}^{u_o+u_z/2} d^2x_j \, z(\mathbf{x}_j) \prod_{k=u_o+u_z/2+1}^{u} d^2x_k \, \overline{z}(\mathbf{x}_k) \, K_u(\mathbf{x}_1, \ldots, \mathbf{x}_u) \,, \tag{11}$$

with an u-th. order integral kernel K_u. Inversion symmetry and orientation shift symmetry require u_o to be even and that the number of fields z equals the number of fields $\overline{z}$. The lowest order term, mediating an interaction between the fields o and z is given by $u = 4, u_o = 2$ i.e.

$$E_4 = \int d^2x_1 d^2x_2 d^2x_3 d^2x_4 \, o(\mathbf{x}_1) o(\mathbf{x}_2) z(\mathbf{x}_3) \overline{z}(\mathbf{x}_4) \, K_4(\mathbf{x}_1, \mathbf{x}_2, \mathbf{x}_3, \mathbf{x}_4) \,. \tag{12}$$

Next, we rewrite Eq. (12) as an integral over an energy density U. We use the invariance under translations to introduce new coordinates

$$\begin{aligned} \mathbf{x}_m &= (1/4)\sum_j^4 \mathbf{x}_i \\ \mathbf{y}_1 &= \mathbf{x}_1 - \mathbf{x}_m \\ \mathbf{y}_2 &= \mathbf{x}_2 - \mathbf{x}_m \\ \mathbf{y}_3 &= \mathbf{x}_3 - \mathbf{x}_m \, . \end{aligned} \tag{13}$$

This leads to

$$\begin{aligned} E_4 &= \int d^2x_m \int d^2y_1 d^2y_2 d^2y_3 \, o(\mathbf{y}_1 + \mathbf{x}_m) o(\mathbf{y}_2 + \mathbf{x}_m) z(\mathbf{y}_3 + \mathbf{x}_m) \\ &\quad \overline{z}(\mathbf{x}_m - \sum_i^3 (\mathbf{y}_i - \mathbf{x}_m)) K(\mathbf{y}_1, \mathbf{y}_2, \mathbf{y}_3) \\ &= \int d^2x_m \, U_4(\mathbf{x}_m) \, . \end{aligned} \tag{14}$$

The kernel K may contain local and non-local contributions. Map interactions were assumed to be local. For local interactions the integral kernel is independent of the locations $\mathbf{y}_i$. We expanded both fields in a Taylor series around $\mathbf{x}_m$

$$z(\mathbf{x}_m + \mathbf{y}_i) = z(\mathbf{x}_m) + \nabla z(\mathbf{x}_m)\mathbf{y}_i + \ldots, \quad o(\mathbf{x}_m + \mathbf{y}_i) = o(\mathbf{x}_m) + \nabla o(\mathbf{x}_m)\mathbf{y}_i + \ldots \tag{15}$$

For a local energy density we could truncate this expansion at the first order in the derivatives. The energy density can thus be written

$$\begin{aligned} U_4(\mathbf{x}_m) &= \int d^2y_1 d^2y_2 d^2y_3 \left(o(\mathbf{x}_m) + \nabla o(\mathbf{x}_m)\mathbf{y}_1\right)\left(o(\mathbf{x}_m) + \nabla o(\mathbf{x}_m)\mathbf{y}_2\right) \\ &\quad \left(z(\mathbf{x}_m) + \nabla z(\mathbf{x}_m)\mathbf{y}_3\right) \left(\overline{z}(\mathbf{x}_m) - \nabla \overline{z}(\mathbf{x}_m) \sum_i (\mathbf{y}_i - \mathbf{x}_m)\right) K(\mathbf{y}_1, \mathbf{y}_2, \mathbf{y}_3) \, . \end{aligned} \tag{16}$$

Due to rotation symmetry this energy density should be invariant under a simultaneous rotation of both fields. From all possible combinations of Eq. (16) only those are invariant in which the gradients of the fields appear as scalar products. The energy density can thus be written as

$$\begin{aligned} U_4 &= f(c_1, c_2, \ldots, c_8) \\ &= f(o^2, z^2, z\overline{z}, oz, \nabla o \nabla o, \nabla z \nabla z, \nabla z \nabla \overline{z}, \nabla o \nabla z) \, , \end{aligned} \tag{17}$$

where we suppress the argument $\mathbf{x}_m$. All combinations c_j can also enter via their complex conjugate. The general expression for U_4 is therefore

$$U_4 = \sum_{i>j} l_{ij}^{(1)} c_i c_j + \sum_{i>j} l_{ij}^{(2)} \overline{c}_i \overline{c}_j + \sum_{i,j} l_{ij}^{(3)} c_i \overline{c}_j \, . \tag{18}$$

From all possible combinations we selected those which are invariant under orientation shifts and eye inversions. This leads to

$$\begin{aligned}
U_4 \quad = \quad & l_1 o^4 + l_2|z|^4 + l_3(\nabla o \nabla o)^2 + l_4|\nabla z \nabla z|^2 \\
& + l_5(\nabla z \nabla \overline{z})^2 + l_6(\nabla o \nabla o) o^2 + l_7(\nabla z \nabla \overline{z})|z|^2 \\
& + l_8(\nabla z \nabla z)\overline{z}^2 + l_9(\nabla \overline{z} \nabla \overline{z}) z^2 \\
& + l_{10}(\nabla o \nabla z) o \overline{z} + l_{11}(\nabla o \nabla \overline{z}) o z \\
& + l_{12} o^2|z|^2 + l_{13}|\nabla o \nabla z|^2 + l_{14}(\nabla z \nabla \overline{z}) o^2 \\
& + l_{15}(\nabla o \nabla o)|z|^2 + l_{16}(\nabla z \nabla \overline{z})(\nabla o \nabla o)\,. \qquad (19)
\end{aligned}$$

The energy densities with prefactor l_1 to l_9 do not mediate a coupling between OD and OP fields and can be absorbed into the single field energy functionals. The densities with prefactors l_8 and l_9 (also with l_{10} and l_{11}) are complex and can occur only together with $l_8 = l_9$ ($l_{10} = l_{11}$) to be real. These energy densities, however, are not bounded from below as their real and imaginary parts can have arbitrary positive and negative values. The lowest order terms which are real and positive definite are thus given by

$$U_4 = l_{12} o^2 |z|^2 + l_{13}|\nabla o \nabla z|^2 + l_{14} o^2 \nabla z \nabla \overline{z} + l_{15} \nabla o \nabla o |z|^2 + l_{16}\left(\nabla z \nabla \overline{z}\right)\left(\nabla o \nabla o\right) . \qquad (20)$$

The next higher order energy terms are given by

$$U_6 = o^2|z|^4 + |z|^2 o^4 + o^4 \nabla z \nabla \overline{z} + \ldots \qquad (21)$$

Here the fields $o(\mathbf{x})$ and $z(\mathbf{x})$ enter with an unequal power. In the corresponding field equations these interaction terms enter either in the linear part or in the cubic nonlinearity. We will show in this article that interaction terms that enter in the linear part of the dynamics can lead to a suppression of the pattern and possibly to an instability of the pattern solution. Therefore we considered also higher order interaction terms.

These higher order terms contain combinations of terms in Eq. (20) and are given by

$$\begin{aligned}
U_8 \quad = \quad & o^4|z|^4 + |\nabla o \nabla z|^4 + o^4\left(\nabla z \nabla \overline{z}\right)^2 + \left(\nabla o \nabla o\right)^2 |z|^4 \\
& + \left(\nabla z \nabla \overline{z}\right)^2 \left(\nabla o \nabla o\right)^2 + o^2|z|^2|\nabla o \nabla z|^2 + \ldots \qquad (22)
\end{aligned}$$

As we will show below examples of coupling energies

$$U = \alpha\, o^2|z|^2 + \beta\,|\nabla z \nabla o|^2 + \tau\, o^4|z|^4 + \epsilon\,|\nabla z \nabla o|^4\,, \qquad (23)$$

form a representative set that can be expected to reproduce experimentally observed map relationships. For this choice of energy the corresponding interaction terms in the dynamics Eq. (10) are given by

$$\begin{aligned}
-\frac{\delta U}{\delta \overline{z}} \quad &= \quad N_\alpha[o,o,z] + N_\beta[o,o,z] + N_\epsilon[o,o,o,o,z,z,\overline{z}] + N_\tau[o,o,o,o,z,z,\overline{z}] \\
&= \quad -\alpha o^2 z + \beta \nabla\left(a \nabla o\right) + \epsilon\, 2\nabla\left(|a|^2 a \nabla o\right) - 2\tau\, o^4|z|^2 z, \\
-\frac{\delta U}{\delta o} \quad &= \quad \widetilde{N}_\alpha[o,z,\overline{z}] + \widetilde{N}_\beta[o,z,\overline{z}] + \widetilde{N}_\epsilon[o,o,o,z,z,\overline{z},\overline{z}] + \widetilde{N}_\tau[o,o,o,z,z,\overline{z},\overline{z}] \\
&= \quad -\alpha o|z|^2 + \beta \nabla\left(\overline{a} \nabla z\right) + \epsilon\, 2\nabla\left(|a|^2 \overline{a} \nabla z\right) - 2\tau\, o^3|z|^4 + c.c. \qquad (24)
\end{aligned}$$

with $a = \nabla z \nabla o$ and *c.c.* denoting the complex conjugate. In general, all coupling energies in U_4, U_6, and U_8 can occur in the dynamics and we restrict to those energies which are expected to reproduce the observed geometric relationships between OP and OD maps. It is important to note that with this restriction we did not miss any essential parts of the model. When using weakly nonlinear analysis the

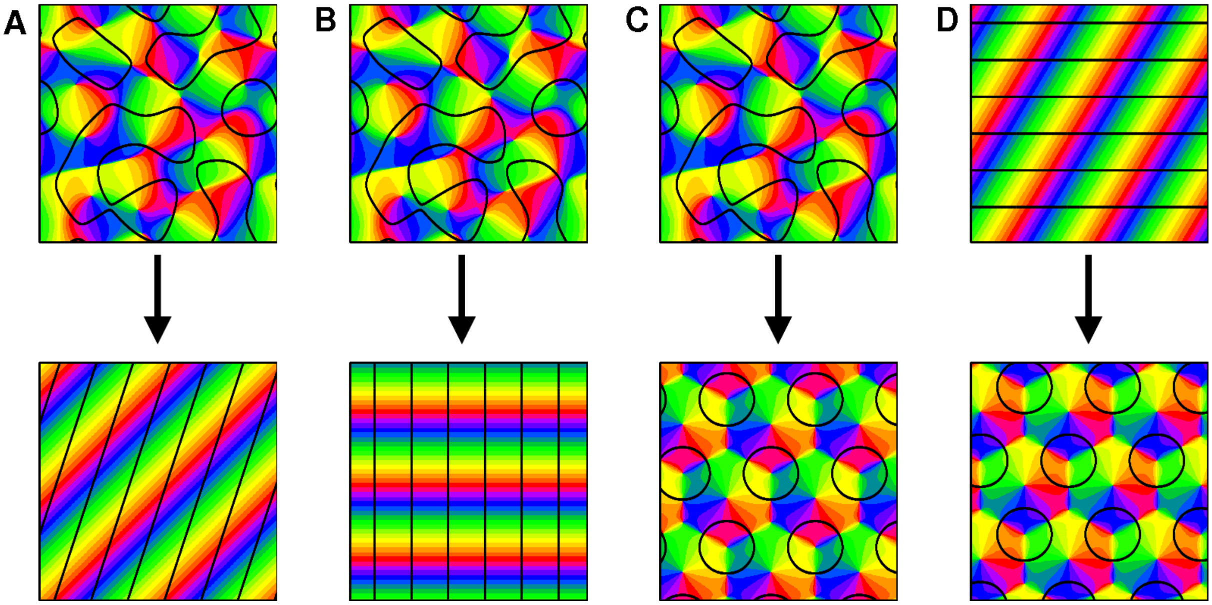

Figure 2. Pinwheel annihilation, preservation, and generation in numerical simulations for different strengths of inter-map coupling and OD bias, $r_o = 0.2, r_z = 0.02$. Color code of OP map with zero contours of OD map superimposed. **A** $\gamma = 0, \epsilon = 0$ **B** $\gamma = 0, \epsilon = 2000$ **C** and **D** $\gamma = 0.15, \epsilon = 2000$. Initial conditions identical in **A - C**, $T_f = 10^4\, r_z^{-1}$.

general form of the near threshold dynamics is insensitive to the used type of coupling energy and we therefore expect similar results also for the remaining coupling energies.

Numerical simulations of the dynamics Eq. (10) with the coupling energy Eq. (23) and $\alpha = \beta = \tau = 0$ are shown in Fig. 2. The initial conditions and final states are shown for different bias terms γ and inter-map coupling strengths ϵ. We observed that for a substantial contralateral bias and above a critical inter-map coupling pinwheels are preserved from random initial conditions or are generated if the initial condition is pinwheel free. Without a contralateral bias the final states were pinwheel free stripe solutions irrespective of the strength of the inter-map coupling.

Calculating ground states by coupled amplitude equations

We studied Eq. (10) with the inter-map coupling energies Eq. (23) using weakly nonlinear analysis. To obtain coupled amplitude equations for the fields $z(\mathbf{x},t)$ and $o(\mathbf{x},t)$ we expanded both fields in powers of the small expansion parameter μ. To account for the fact that one bifurcation parameter can be substantially smaller than the other we expanded the fields as

$$\begin{aligned} o(\mathbf{x},t) &= \mu o_1(\mathbf{x},t) + \mu^2 o_2(\mathbf{x},t) + \mu^3 o_3(\mathbf{x},t) + \dots \\ z(\mathbf{x},t) &= (\kappa\mu) z_1(\mathbf{x},t) + (\kappa\mu)^2 z_2(\mathbf{x},t) + (\kappa\mu)^3 z_3(\mathbf{x},t) + \dots \end{aligned} \tag{25}$$

We further expanded both control parameters as

$$\begin{aligned} r_o &= \mu \tilde{r}_1 + \mu^2 \tilde{r}_2 + \mu^3 \tilde{r}_3 + \dots \\ r_z &= (\kappa\mu) r_1 + (\kappa\mu)^2 r_2 + (\kappa\mu)^3 r_3 + \dots \end{aligned} \tag{26}$$

We introduced a common slow timescale $T = r_z t$ and insert the expansions in Eq. (10) and get

$$\begin{aligned} 0 \;=\;& \mu\kappa \hat{L}^0 z_1 \\ &+\mu^2\kappa^2 \left(-\hat{L}^0 z_2 + r_1 z_1 - r_1 \partial_T z_1\right) \\ &+\mu^3\kappa^3 \left(-r_2\partial_T z_1 + r_2 z_1 + r_1 z_2 - r_1 \partial_T z_2 - \hat{L}^0 z_3 - N_{3,u}[z_1, z_1, \overline{z}_1]\right) \\ &+\mu^3\kappa \left(-\alpha N_{3,c}[z_1, o_1, o_1]\right) \\ &\vdots \\ &+\mu^7\kappa^7 \left(-\hat{L}^0 z_7 + r_2 z_5 + r_4 z_3 + r_6 z_1 + \dots - N_{3,u}[z_3, z_1, \overline{z}_3] + N_{3,u}[z_5, z_1, \overline{z}_1] + \dots\right) \\ &+\mu^7 \left(-\alpha\kappa^5 N_{3,c}[z_5, o_1, o_1] - \kappa^3 \alpha N_{3,c}[z_3, o_3, o_1] - \dots\right) \\ &+\mu^7\kappa^3 \left(-\epsilon N_{7,c}[z_1, z_1, \overline{z}_1, o_1, o_1, o_1, o_1]\right) \\ &\vdots \end{aligned} \tag{27}$$

and

$$\begin{aligned} 0 \;=\;& \mu \hat{L}^0 o_1 \\ &+\mu^2 \left(-\hat{L}^0 o_2 + \tilde{r}_1 o_1 - \kappa r_1 \partial_T o_1 + \sqrt{\mu \tilde{r}_1 + \mu^2 \tilde{r}_2 + \dots}\, \tilde{N}_{2,u}[o_1, o_1]\right) \\ &+\mu^3 \left(-\kappa^2 r_2 \partial_T o_1 + \tilde{r}_2 o_1 + \tilde{r}_1 o_2 - \kappa r_1 \partial_T o_2 - \hat{L}^0 o_3 - \tilde{N}_{3,u}[o_1, o_1, o_1]\right) \\ &+\mu^3 \left(-\kappa^2 \alpha \tilde{N}_{3,c}[z_1, \overline{z}_1, o_1]\right) \\ &\vdots \\ &+\mu^7 \left(-\hat{L}^0 o_7 + \tilde{r}_2 o_5 + \tilde{r}_4 o_3 + \tilde{r}_6 o_1 + \dots - \tilde{N}_{3,u}[o_3, o_1, o_1] - \tilde{N}_{2,u}[o_1, o_5] - \dots\right) \\ &+\mu^7 \left(-\kappa^5 \alpha \tilde{N}_{3,c}[z_5, o_1, o_1] - \kappa^3 \alpha \tilde{N}_{3,c}[z_3, o_3, o_1] - \dots\right) \\ &+\mu^7\kappa^4 \left(-\epsilon \tilde{N}_{7,c}[z_1, z_1, \overline{z}_1, \overline{z}_1, o_1, o_1, o_1]\right) \\ &\vdots \end{aligned} \tag{28}$$

with the nonlinearities $\tilde{N}_{2,u} = o^2$, $N_{3,u} = |z|^2 z$, $\tilde{N}_{3,u} = o^3$, and $N_{3,c}$, $N_{7,c}$, $\tilde{N}_{3,c}$, $\tilde{N}_{7,c}$ the nonlinearities of the inter-map coupling energy Eq. (24).

We further scaled out the inter-map coupling strength α and ϵ. We consider amplitude equations up to seventh order as this is the order where the nonlinearity of the higher order coupling energy enters first. For Eq. (27) and Eq. (28) to be fulfilled each individual order in μ has to be zero. At linear order in μ we get the two homogeneous equations

$$\hat{L}^0 z_1 = 0\,, \quad \hat{L}^0 o_1 = 0\,. \tag{29}$$

Thus z_1 and o_1 are elements of the kernel of $\hat{L}^0$. The kernel contains linear combinations of modes with a wavevector on the critical circle i.e.

$$\begin{aligned} z_1(\mathbf{x}, T) &= \sum_j^n \left(A_j^{(1)}(T) e^{\imath \vec{k}_j \vec{x}} + A_{j^-}^{(1)}(T) e^{-\imath \vec{k}_j \vec{x}}\right) \\ o_1(\mathbf{x}, T) &= \sum_j^n \left(B_j^{(1)}(T) e^{\imath \vec{k}_j \vec{x}} + \overline{B}_j^{(1)}(T) e^{-\imath \vec{k}_j \vec{x}}\right), \end{aligned} \tag{30}$$

with the complex amplitudes $A_j^{(1)} = \mathcal{A}_j e^{\imath\phi_j}$, $B_j^{(1)} = \mathcal{B}_j e^{\imath\psi_j}$. In view of the hexagonal or stripe layout of the OD pattern shown in Fig. 2 $n = 3$ is an appropriate choice. Since in cat visual cortex the typical wavelength for OD and OP maps are approximately the same [58, 59] i.e. $k_{c,o} = k_{c,z}$ the Fourier components of the emerging pattern are located on a common critical circle $\vec{k}_j = \vec{k}'_j = (\cos\alpha_j, \sin\alpha_j)\, k_c$. To account for species differences we also studied models with detuned OP and OD wavelengths. At second order in μ we get

$$\begin{aligned} \hat{L}^0 z_2 + r_1 z_1 - r_1 \partial_T z_1 &= 0 \\ \hat{L}^0 o_2 + \tilde{r}_1 o_1 - \kappa r_1 \partial_T o_1 &= 0\,. \end{aligned} \tag{31}$$

As z_1 and o_1 are elements of the kernel $r_1 = \tilde{r}_1 = 0$. At third order, when applying the solvability condition (see Methods), we get

$$\begin{aligned} r_2 \partial_T\, z_1 &= r_2 z_1 - \hat{P}_c N_{3,u}[z_1, z_1, \overline{z}_1] - \frac{\alpha}{\kappa^2} \hat{P}_c N_{3,c}[z_1, o_1, o_1] \\ \kappa^2 r_2 \partial_T\, o_1 &= \tilde{r}_2 o_1 - \sqrt{\tilde{r}_2}\, \hat{P}_c \tilde{N}_{2,u}[o_1, o_1] - \hat{P}_c \tilde{N}_{3,u}[o_1, o_1, o_1] - \kappa^2 \alpha \hat{P}_c \tilde{N}_{3,c}[z_1, \overline{z}_1, o_1]\,. \end{aligned} \tag{32}$$

We insert the leading order fields Eq. (30) and obtain the amplitude equations

$$\begin{aligned} r_2 \partial_T A_i^{(1)} = \quad & r_2 A_i^{(1)} - \sum_j g_{ij} |A_j^{(1)}|^2 A_i^{(1)} - \sum_j f_{ij} A_j^{(1)} A_{j^-}^{(1)} \overline{A}_{i^-}^{(1)} - \frac{\alpha}{\kappa^2} \sum_j h_{ij} |B_j^{(1)}|^2 A_i^{(1)} \\ \kappa^2 r_2 \partial_T B_i^{(1)} = \quad & \tilde{r}_2 B_i^{(1)} - 2\sqrt{\tilde{r}_2}\, \overline{B}_{i+1}^{(1)} \overline{B}_{i+2}^{(1)} - \sum_j \tilde{g}_{ij} |B_j^{(1)}|^2 B_i^{(1)} - \alpha\kappa^2 \sum_j h_{ij} |A_j^{(1)}|^2 B_i^{(1)}\,. \end{aligned} \tag{33}$$

For simplicity we have written only the simplest coupling terms. Depending on the configuration of active modes additional contributions may enter the amplitude equations. In addition there are coupling terms which contain the constant δ, see Methods. The coupling coefficients are given by

$$\begin{aligned} g_{ij} &= e^{-\imath\vec{k}_i\vec{x}} \left(N_{3,u}[e^{\imath\vec{k}_i\vec{x}}, e^{\imath\vec{k}_j\vec{x}}, e^{-\imath\vec{k}_j\vec{x}}] + N_{3,u}[e^{\imath\vec{k}_j\vec{x}}, e^{\imath\vec{k}_i\vec{x}}, e^{-\imath\vec{k}_j\vec{x}}] \right) \\ g_{ii} &= e^{-\imath\vec{k}_i\vec{x}}\, N_{3,u}[e^{\imath\vec{k}_i\vec{x}}, e^{\imath\vec{k}_i\vec{x}}, e^{-\imath\vec{k}_i\vec{x}}] \\ g_{ij^-} &= e^{-\imath\vec{k}_i\vec{x}} \left(N_{3,u}[e^{\imath\vec{k}_i\vec{x}}, e^{-\imath\vec{k}_j\vec{x}}, e^{\imath\vec{k}_j\vec{x}}] + N_{3,u}[e^{-\imath\vec{k}_j\vec{x}}, e^{\imath\vec{k}_i\vec{x}}, e^{\imath\vec{k}_j\vec{x}}] \right) \\ f_{ij} &= e^{-\imath\vec{k}_i\vec{x}} \left(N_{3,u}[e^{\imath\vec{k}_j\vec{x}}, e^{-\imath\vec{k}_j\vec{x}}, e^{\imath\vec{k}_i\vec{x}}] + N_{3,u}[e^{-\imath\vec{k}_j\vec{x}}, e^{\imath\vec{k}_j\vec{x}}, e^{\imath\vec{k}_i\vec{x}}] \right) \\ f_{ii} &= 0 \\ h_{ij} &= e^{-\imath\vec{k}_i\vec{x}} N_{3,c}[e^{\imath\vec{k}_i\vec{x}}, e^{\imath\vec{k}_j\vec{x}}, e^{-\imath\vec{k}_j\vec{x}}] \\ h_{ii} &= e^{-\imath\vec{k}_i\vec{x}}\, N_{3,c}[e^{\imath\vec{k}_i\vec{x}}, e^{\imath\vec{k}_i\vec{x}}, e^{-\imath\vec{k}_i\vec{x}}]\,. \end{aligned} \tag{34}$$

When we set $r_2 = 1/\kappa^2$ and $\tilde{r}_2 = 1$ we get

$$\begin{aligned} \partial_T A_i^{(1)} &= \left(1 - \alpha \sum_j h_{ij} |B_j^{(1)}|^2 \right) A_i^{(1)} - \kappa^2 \sum_j \left(g_{ij} |A_j^{(1)}|^2 A_i^{(1)} + f_{ij} A_j^{(1)} A_{j^-}^{(1)} \overline{A}_{i^-}^{(1)} \right) \\ \partial_T B_i^{(1)} &= B_i^{(1)} - 2\overline{B}_{i+1}^{(1)} \overline{B}_{i+2}^{(1)} - \sum_j \tilde{g}_{ij} |B_j^{(1)}|^2 B_i^{(1)} - \kappa^2 \alpha \sum_j h_{ij} |A_j^{(1)}|^2 B_i^{(1)}\,. \end{aligned} \tag{35}$$

For $\kappa \to 0$ the inter-map coupling term in the dynamics of the modes $B^{(1)}$ vanishes, leading to an uncoupled OD dynamics. In the dynamics for the modes $A^{(1)}$ the uncoupled cubic nonlinearities vanishes

in this limit. Thus the dynamics is governed by the linear terms only. Inter-map coupling thus influences the growth rate of the Fourier modes. For large enough inter-map coupling strength α the growth rate becomes negative. In this case only the homogeneous solution $A_j^{(1)} = 0$, $\forall j$ is stable.
Alternatively, we can set $r_2 = \tilde{r}_2 = 1$ in Eq. (33), scale back to the fast time t, and rescale the amplitudes as $A_i = \sqrt{r_z} A_i^{(1)}$, $B_i = \sqrt{r_o} B_i^{(1)}$. This leads to the amplitude equations

$$\begin{aligned}
\partial_t A_i &= r_z A_i - \sum_j g_{ij} |A_j|^2 A_i - \sum_j f_{ij} A_j A_{j^-} \overline{A}_{i^-} - \frac{\alpha}{\kappa^2} \frac{r_z}{r_o} \sum_j h_{ij} |B_j|^2 A_i \\
\kappa^2 \frac{r_o}{r_z} \partial_t B_i &= r_o B_i - 2 \overline{B}_{i+1} \overline{B}_{i+2} - \sum_j \tilde{g}_{ij} |B_j|^2 B_i - \alpha \kappa^2 \frac{r_o}{r_z} \sum_j h_{ij} |A_j|^2 B_i \,.
\end{aligned} \tag{36}$$

Since $r_z / r_o = \kappa^2 + \left(\kappa^4 r_4 - \kappa^2 \tilde{r}_4\right) \mu^2 + \ldots$ we get at leading order

$$\begin{aligned}
\partial_t A_i &= \left(r_z - \alpha \sum_j h_{ij} |B_j|^2 \right) A_i - \sum_j g_{ij} |A_j|^2 A_i - \sum_j f_{ij} A_j A_{j^-} \overline{A}_{i^-} \\
\partial_t B_i &= r_o B_i - 2 \overline{B}_{i+1} \overline{B}_{i+2} - \sum_j \tilde{g}_{ij} |B_j|^2 B_i - \alpha \sum_j h_{ij} |A_j|^2 B_i \,.
\end{aligned} \tag{37}$$

At higher order we obtain corrections to the uncoupled dynamics of $z(\mathbf{x}, t)$ and $o(\mathbf{x}, t)$. In addition we get corrections to the third order coupling energy terms. Finally, at seventh order enters the nonlinearity of the higher order coupling energy term. The amplitude equations up to seventh order are thus derived from

$$\begin{aligned}
\kappa^3 r_2 \partial_T z_1 &= \kappa^3 r_2 z_1 - \kappa^3 \hat{P} N_{3,u}[z_1, z_1, \overline{z}_1] - \kappa \alpha \hat{P} N_{3,c}[z_1, o_1, o_1] \\
\kappa^5 r_2 \partial_T z_3 &= \kappa^5 r_2 z_3 - \cdots - \kappa^5 \hat{P} N_{3,u}[z_1, z_1, \overline{z_3}] \\
\kappa^7 r_2 \partial_T z_5 &= \kappa^7 r_2 z_5 - \cdots - \kappa^7 \hat{P} N_{3,u}[z_3, z_1, \overline{z_3}] - \epsilon \kappa^3 \hat{P} N_{7,c}[z_1, z_1, \overline{z}_1, o_1, o_1, o_1, o_1] \,,
\end{aligned} \tag{38}$$

and corresponding equations for the fields o_1, o_3, and o_5. The field z_1 is given in Eq. (30) and its amplitudes $A^{(1)}$ and $B^{(1)}$ are determined at third order. The field z_3 contains contributions from modes off the critical circle $z_{3,off}$, $|\vec{k}_{off}| \neq k_c$ and on the critical circle i.e. $z_3 = z_{3,off} + \sum_j^n \left(A_j^{(3)}(T) e^{\imath \vec{k}_j \vec{x}} + A_{j^-}^{(3)}(T) e^{-\imath \vec{k}_j \vec{x}} \right)$. Its amplitude $A^{(3)}$ are determined at fifth order. The field z_5 also contains contributions from modes off the critical circle $z_{5,off}$ and on the critical circle i.e. $z_5 = z_{5,off} + \sum_j^n \left(A_j^{(5)}(T) e^{\imath \vec{k}_j \vec{x}} + A_{j^-}^{(5)}(T) e^{-\imath \vec{k}_j \vec{x}} \right)$. Its amplitude $A^{(5)}$ are determined at seventh order. This leads to a series of amplitude equations

$$\begin{aligned}
\kappa^3 r_2 \partial_T A_i^{(1)} &= \kappa^3 r_2 A_i^{(1)} - \kappa^3 \sum_j g_{ij} |A_j^{(1)}|^2 A_i^{(1)} - \kappa^3 \sum_j f_{ij} A_j^{(1)} A_{j^-}^{(1)} \overline{A}_{i^-}^{(1)} - \kappa \alpha \sum_j h_{ij} A_i^{(1)} |B_j^{(1)}|^2 \\
\kappa^5 r_2 \partial_T A_i^{(3)} &= \kappa^5 r_2 A_i^{(3)} - \cdots - \kappa^5 \sum_j g_{ij} |A_j^{(1)}|^2 \overline{A}_i^{(3)} \\
\kappa^7 r_2 \partial_T A_i^{(5)} &= \kappa^7 r_2 A_i^{(5)} - \cdots - \kappa^7 \sum_j g_{ij} |A_j^{(3)}|^2 A_i^{(1)} - \epsilon \kappa^3 \sum_{jlk} h_{ijlk} |A^{(1)}|^2 |B^{(1)}|^2 |B^{(1)}|^2 A_i^{(1)} \,,
\end{aligned} \tag{39}$$

which are solved order by order. To derive amplitude equations at seventh order we use the higher order coupling energies and neglect the low order coupling energies i.e. set $\alpha = 0$. The higher order corrections to the uncoupled part are proportional to κ^5 and κ^7 while the inter-map coupling part is proportional to κ^3. For $\kappa \ll 1$ we thus can neglect fifth and seventh order corrections in the uncoupled dynamics.

We set $r_2 = \tilde{r}_2 = 1$ and rescale the amplitudes as $A^{(1)} = r_z^{1/2} A^{(1)}, A^{(3)} = r_z^{3/2} A^{(3)}, A^{(5)} = r_z^{5/2} A^{(5)}$, $B^{(1)} = r_o^{1/2} B^{(1)}, B^{(3)} = r_o^{3/2} B^{(3)}, B^{(5)} = r_o^{5/2} B^{(5)}$ and rescale to the fast time. This leads to

$$\begin{aligned}
\partial_t A_i^{(1)} &= r_z A_i^{(1)} - \sum_j g_{ij} |A_j^{(1)}|^2 A_i^{(1)} - \sum_j f_{ij} A_j^{(1)} A_{j^-}^{(1)} \overline{A}_{i^-}^{(1)} \\
\partial_t A_i^{(3)} &= r_z A_i^{(3)} - \cdots - \sum_j g_{ij} |A_j^{(1)}|^2 \overline{A}_i^{(3)} \\
\partial_t A_i^{(5)} &= r_z A_i^{(5)} - \cdots - \sum_j g_{ij} |A_j^{(3)}|^2 A_i^{(1)} - \epsilon \frac{1}{\kappa^4} \sum_{jlk} h_{ijlk} |A^{(1)}|^2 |B^{(1)}|^2 |B^{(1)}|^2 A_i^{(1)} \,.
\end{aligned} \tag{40}$$

We can combine the amplitude equations up to seventh order by introducing the amplitudes $A_j = A_j^{(1)} + A_j^{(3)} + A_j^{(5)}$ and $B_j = B_j^{(1)} + B_j^{(3)} + B_j^{(5)}$. This leads to the amplitude equations

$$\begin{aligned}
\partial_t\, A_i &= r_z A_i - \sum_j g_{ij} |A_j|^2 A_i - \sum_j f_{ij} A_j A_{j^-} \overline{A}_{i^-} \\
&\quad - \epsilon \frac{r_z^2}{r_o^2 \kappa^4} \sum_{jlk} h_{ijlk} |A_j|^2 |B_l^2| |B_k|^2 A_i \,.
\end{aligned} \tag{41}$$

Since $r_z / r_o = \kappa^2 + \left(\kappa^4 r_4 - \kappa^2 \tilde{r}_4\right) \mu^2 + \ldots$ we finally obtain

$$\begin{aligned}
\partial_t\, A_i &= r_z A_i - \sum_j g_{ij} |A_j|^2 A_i - \sum_j f_{ij} A_j A_{j^-} \overline{A}_{i^-} \\
&\quad - \epsilon \sum_{jlk} h_{ijlk} |A_j|^2 |B_l^2| |B_k|^2 A_i \\
\partial_t\, B_i &= r_o B_i - 2 \overline{B}_{i+1} \overline{B}_{i+2} - \sum_j \tilde{g}_{ij} |B_j|^2 A B_i \\
&\quad - \epsilon \sum_{jlk} h_{ijlk} |B_j|^2 |A_l^2| |A_k|^2 B_i \,.
\end{aligned} \tag{42}$$

In this article we used the amplitude equations (37) when considering the low order inter-map coupling energies and the amplitude equations (42) when considering the higher order inter-map coupling energies.

Interpretation of coupling energies

Using symmetry considerations we derived inter-map coupling energies up to eighth order in the fields, see Eq. (20), Eq.(21), and Eq.(22). Which of these various optimization principles could reproduce realistic inter-map relationships such as a uniform coverage of all stimulus features? We identified two types of optimization principles that can be expected to reproduce realistic inter-map relationships and good stimulus coverage. First, product-type coupling energies of the form $U = o^{2n} |z|^{2n}$, $n = 1, 2, ...$ These energies favor configurations in which regions of high gradients avoid each other and thus leading to high coverage. Second, gradient-type coupling energies of the form $U = |\nabla o \nabla z|^{2n}$, $n = 1, 2, ...$ In experimentally obtained maps, iso-orientation lines show the tendency to intersect the OD borders perpendicularly. Perpendicular intersection angles lead to high coverage as large changes of the field z in one direction lead to small changes of the field o in that direction. To see that the gradient-type coupling energy favors perpendicular intersection angles we decompose the complex field $z(\mathbf{x})$ into the selectivity $|z|$ and the preferred orientation ϑ. We obtain

$$U = |\nabla z \nabla o|^{2n} = |z|^{2n} \left(|\nabla o \nabla \ln |z||^2 + 4 |\nabla o \nabla \vartheta|^2 \right)^n \,. \tag{43}$$

If the orientation selectivity is locally homogeneous, i.e. $\nabla \ln|z| \approx 0$, then the energy is minimized if the direction of the iso-orientation lines ($\nabla\vartheta$) is perpendicular to the OD borders. In our symmetry-based analysis we further identified terms that are expected to lead to the opposite behavior for instance mixture terms such as $U = o^2 \nabla z \nabla \overline{z}$.

Pinwheels are prominent features in OP maps. We therefore also analyze how different optimization principles impact on the pinwheel positions with respect to the co-evolving feature maps. The product-type coupling energies are expected to favor pinwheels at OD extrema. Pinwheels are zeros of z and are thus expected to reduce this energy term. They will reduce energy the most when $|o|$ is maximal which should repel pinwheels from OD borders, where $o(\mathbf{x})$ is zero. Also the gradient-type coupling energy is expected to couple the OD pattern with the position of pinwheels. To see this we decompose the field z into its real and imaginary part

$$U = \left(|\nabla o\, \nabla \mathrm{Re} z|^2 + |\nabla o\, \nabla \mathrm{Im} z|^2\right). \tag{44}$$

At pinwheel centers the zero contours of $\mathrm{Re}\, z$ and $\mathrm{Im}\, z$ cross. Since there $\nabla \mathrm{Re}\, z$ and $\nabla \mathrm{Im}\, z$ are almost constant and not parallel the energy can be minimized only if $|\nabla o|$ is small at the pinwheel centers, i.e. the extrema or saddle-points of $o(\mathbf{x})$.

Part II: Optima of particular optimization principles

The impact of inter-map coupling: Low order coupling terms

As indicated by numerical simulations and weakly nonlinear analysis of the uncoupled OD dynamics, see Methods, we discussed the influence of the OD stripe, hexagon, and constant solutions on the OP map using the coupled amplitude equations derived in the previous section. A potential backreaction onto the dynamics of the OD map can be neglected if the modes A_j of the OP map are much smaller than the modes B_j of the OD map. This can be achieved if $r_z \ll r_o$. We first give a brief description of the uncoupled OP solutions. Next, we study the impact of the low order coupling energies in Eq. (23) on these solutions. We demonstrate that these energies can lead to a complete suppression of orientation selectivity. In the uncoupled case there are for $r_z > 0$ two stable stationary solutions to the amplitude equations Eq. (37), namely OP stripes

$$z_{\mathrm{st}} = \mathcal{A} e^{\imath(kx+\phi)}, \quad \mathcal{A} = \sqrt{r_z}\,, \tag{45}$$

and OP rhombic solutions

$$z_{\mathrm{rh}} = \mathcal{A} \sum_{j=1}^{2} \left(e^{\imath k_j x + \phi_j} + e^{-\imath k_j x + \phi_{j^-}} \right), \tag{46}$$

with $\phi_1 + \phi_{1^-} = \phi_0$, $\phi_2 + \phi_{2^-} = \phi_0 + \pi$, ϕ_0 an arbitrary phase, and $\mathcal{A} = \sqrt{r_z/5} \approx 0.447\sqrt{r_z}$. In the uncoupled case the angle $\alpha = \arccos \vec{k_1}\vec{k_2}/k_c^2$ between the Fourier modes is arbitrary. The stripe solutions are pinwheel free while the pinwheel density for the rhombic solutions varies as $\rho = 4\sin\alpha$ and thus $0 \le \rho \le 4$. For the rhombic solutions pinwheels are located on a regular lattice. We therefore refer to these and other pinwheel rich solutions which are spatially periodic as pinwheel crystals (PWC). In particular, we refer to pinwheel crystals with as rhombic spatial layout as rPWC solutions and pinwheel crystals with a hexagonal layout as hPWC solutions. Without inter-map coupling, the potential of the two solutions reads $V_{\mathrm{st}} = -\frac{1}{2} r_z^2 < V_{\mathrm{rh}} = -\frac{2}{5} r_z^2$, thus the stripe solutions are always energetically preferred compared to rhombic solutions.

In the following we study three scenarios in which inter-map coupling can lead to pinwheel stabilization. First, a deformation of the stripe solution can lead to the creation of pinwheels in this solution. Second, inter-map coupling can energetically prefer the (deformed) rhombic solutions compared to the stripe

solutions. Finally, inter-map coupling can lead to the stabilization of new PWC solutions.
For the low order interaction terms the amplitude equations are given by $\partial_t A_i = -\delta V/\delta \overline{A}_i$, $\partial_t B_i = -\delta V/\delta \overline{B}_i$ with the potential

$$\begin{aligned} V &= V_A + V_B + \sum_j^3 \alpha\delta |A_j|^2 + \sum_j^3 \alpha\delta |A_{j^-}|^2 \\ &\quad +2\alpha\delta A_1 \overline{A}_{2^-} B_3 + 2\alpha\delta A_1 \overline{A}_{3^-} B_2 + 2\alpha\delta A_{1^-} \overline{A}_2 \overline{B}_3 + 2\alpha\delta A_{1^-} \overline{A}_3 \overline{B}_2 \\ &\quad + \sum_{i,j} g_{ij}^{(1)} |A_i|^2 |B_j|^2 + \sum_{i\neq j} g_{ij}^{(2)} A_i \overline{A}_j \overline{B}_i B_j + \sum_{i\neq j} g_{ij}^{(2)} A_{i^-} \overline{A}_{j^-} B_i \overline{B}_j \\ &\quad + \sum_{i,j} g_{ij}^{(3)} A_i \overline{A}_{j^-} \overline{B}_i \overline{B}_j + \sum_{i,j} g_{ij}^{(3)} \overline{A}_i A_{j^-} B_i B_j \,, \end{aligned} \tag{47}$$

with the uncoupled contributions

$$\begin{aligned} V_A &= -r_z \sum_j^3 |A_j|^2 + \frac{1}{2} \sum_{i,j}^3 g_{ij} |A_i|^2 |A_j|^2 + \frac{1}{2} \sum_{i,j}^3 f_{ij} A_i A_{i^-} \overline{A}_j \overline{A}_{j^-} \\ V_B &= -r_o \sum_j^3 |B_j|^2 + \frac{1}{2} \sum_{i,j}^3 \widetilde{g}_{ij} |B_i|^2 |B_j|^2 \,. \end{aligned} \tag{48}$$

The coupling coefficients read $g_{ij}^{(1)} = 2\alpha + 2\beta\cos^2(\alpha_{ij})$, $g_{ij}^{(2)} = 2\alpha + \beta\left(1+\cos^2(\alpha_{ij})\right)$, $g_{ij}^{(3)} = 2\alpha + \beta\left(1+\cos^2(\alpha_{ij})\right)$, $g_{ii}^{(3)} = \alpha + \beta$, where α_{ij} is the angle between the wavevector $\vec{k}_i$ and $\vec{k}_j$.

Product-type energy $U = \alpha o^2 |z|^2$

We first studied the impact of the low order product-type coupling energy. Here, the constant $\delta(\gamma)$ enters explicitly in the amplitude equations.

Stationary solutions and their stability

In the case of OD stripes, see Methods, with $B_1 = B, B_2 = B_3 = 0$ we get the following amplitude equations

$$\begin{aligned} \partial_t A_1 &= \left(r_z - \alpha\delta^2 - 2\alpha|B|^2\right) A_1 - \alpha B^2 A_{1^-} + \text{nct.} \\ \partial_t A_2 &= \left(r_z - \alpha\delta^2 - 2\alpha|B|^2\right) A_2 - 2\alpha\delta A_{3^-} \overline{B} + \text{nct.} \\ \partial_t A_3 &= \left(r_z - \alpha\delta^2 - 2\alpha|B|^2\right) A_3 - 2\alpha\delta A_{2^-} \overline{B} + \text{nct.} \end{aligned} \tag{49}$$

where nct. refers to non inter-map coupling terms $-\sum_j^3 g_{ij}|A_j|^2 A_i - \sum_{j\neq i}^3 f_{ij} A_j A_{j^-} \overline{A}_{i^-}$, resulting from the potential V_A, see Eq. (48). The equations for the modes A_{i^-} are given by interchanging the modes A_i and A_{i^-} as well as interchanging the modes B_i and $\overline{B}_i$. The OP stripe solution in case of inter-map coupling is given by

$$z = \mathcal{A}_1 e^{\imath(\vec{k}_1\vec{x}+\phi_1)} + \mathcal{A}_{1^-} e^{-\imath(\vec{k}_1\vec{x}+\phi_{1^-})} \,, \tag{50}$$

with $\mathcal{A}_1 = p^{3/2}/(2\sqrt{2}B^2\alpha)$, $\mathcal{A}_{1^-} = p/\sqrt{2}$, and
$p = r_z - 2B^2\alpha - \alpha\delta^2 - \sqrt{(r_z-\alpha\delta^2)(r_z-\alpha(4B^2+\delta^2))}$ and the phase relation
$\phi_1 - \phi_{1^-} = 2\psi_1 + \pi$. In the uncoupled case ($\alpha = 0$) they reduce to $\mathcal{A}_{1^-} = 0$ and $\mathcal{A}_1 = \sqrt{r_z}$. With increasing inter-map coupling the amplitude $\mathcal{A}_{1^-}$ grows and the solutions are transformed, reducing the

representation of all but two preferred orientations. The parameter dependence of this solution is shown in Fig. 3**A** for different values of the bias γ. Both amplitudes become identical at $\alpha = r_z/(4B^2 + \delta^2)$ with

$$\mathcal{A}_1 = \mathcal{A}_{1^-} = \sqrt{\frac{r_z - \alpha B^2 - \alpha\delta^2}{3}}\,. \tag{51}$$

This pattern solution finally vanishes at

$$\alpha_c = r_z/(B^2 + \delta^2) = 3\, r_z/r_o\,. \tag{52}$$

This existence border is thus independent of the OD bias γ. Above this coupling strength only the trivial solution $A_j = 0,\, \forall j$ is stable.

In addition to the OP stripe patterns there exist rhombic OP solutions, see Fig. 3**B**. These rhombic solutions are pinwheel rich with a pinwheel density of $\rho = 4 \sin \pi/3 \approx 3.46$ but are energetically not preferred compared to the stripe solutions, see Fig. 3**E**. The rhombic solutions in the uncoupled case $\mathcal{A}_1 = \mathcal{A}_{1^-} = \mathcal{A}_2 = \mathcal{A}_{2^-}$, $\mathcal{A}_3 = \mathcal{A}_{3^-} = 0$ are transformed by inter-map coupling. The phase relations are given by

$$\begin{aligned}
\phi_1 + \phi_{1^-} &= \phi_0 \\
\phi_2 + \phi_{2^-} &= \phi_0 + \pi \\
\phi_3 + \phi_{3^-} &= \phi_0 + \pi \\
\phi_1 - \phi_{1^-} &= 2\psi_1 + \pi \\
\psi_1 + \phi_2 + \phi_3 &= \phi_0\,,
\end{aligned} \tag{53}$$

where ϕ_0 is an arbitrary phase. Stationary amplitudes are given by

$$\begin{aligned}
\mathcal{A}_1 = \mathcal{A}_{1^-} &= \sqrt{\frac{r_z + \alpha(\mathcal{B}^2 - \delta^2)}{5}} \\
\mathcal{A}_2 = \mathcal{A}_{2^-} &= \sqrt{\frac{3r_z - 12\mathcal{B}^2\alpha - 3\alpha\delta^2 - 1/3q}{30}} \\
\mathcal{A}_3 = \mathcal{A}_{3^-} &= \mathcal{A}_2 \frac{3r_z - 12\mathcal{B}^2\alpha - 3\alpha\delta^2 + 1/3q}{20\mathcal{B}\alpha\delta}\,,
\end{aligned} \tag{54}$$

with $q = \sqrt{-3600\mathcal{B}^2\alpha^2\delta^2 + (-9r_z + 36\mathcal{B}^2\alpha + 9\alpha\delta^2)^2}$. With increasing inter-map coupling strength α the amplitudes $A_2 = A_{2^-}$ are suppressed, see Fig. (3)**B**. In addition, for nonzero bias γ, there is an increase of the amplitudes $A_3 = A_{3^-}$. The amplitudes A_2 and A_3 collapse at $\alpha/r_z = 3/(12\mathcal{B}^2 + 20\mathcal{B}\delta + 3\delta^2)$. A further increase of the inter-map coupling strength leads to a suppression of these amplitudes and finally to the OP stripe pattern where $\mathcal{A}_2 = \mathcal{A}_3 = 0$.

In the case the OD map is a constant, Eq. (117), the amplitude equations simplify to

$$\partial_t\, A_i = \left(r_z - \alpha\delta^2\right) A_i - \sum_j g_{ij} |A_j|^2 A_i - \sum_j f_{ij} A_j A_{j^-} \overline{A}_{i^-}\,. \tag{55}$$

Thus inter-map coupling in this case only renormalizes the bifurcation parameter and the energetic ground state is thus a stripe pattern with an inter-map coupling dependent reduction of the amplitudes

$$\mathcal{A}_1 = \sqrt{r_z - \alpha\delta^2}\,, \mathcal{A}_2 = \mathcal{A}_3 = 0\,. \tag{56}$$

Therefore at $\alpha_c = r_z/\delta^2$ the stripe pattern ceases to exist and the only stable solution is the trivial one i.e. $A_i = 0$. In addition, there is the rhombic solution with the stationary amplitudes

$$\mathcal{A}_1 = \mathcal{A}_{1^-} = \mathcal{A}_2 = \mathcal{A}_2 = \sqrt{\frac{r_z - \alpha\delta^2}{5}}\,, \mathcal{A}_3 = 0\,. \tag{57}$$

In the case of OD hexagons $B_i = \mathcal{B}e^{\imath\psi_i}$, Eq. (116), the amplitude equations read

$$\begin{aligned}\partial_t\, A_i \;=\;& \left(r_z - 6\alpha\mathcal{B}^2 - \alpha\delta^2\right) A_i - \alpha\mathcal{B}^2 \left(A_{i^-} e^{2\imath\psi_i} + 2A_{(i+1)^-} e^{\imath(\psi_i+\psi_{i+1})} + 2A_{(i+2)^-} e^{\imath(\psi_i+\psi_{i+2})}\right)\\ & -2\alpha\mathcal{B}^2 \left(A_{i+1} e^{\imath(\psi_i-\psi_{i+1})} + A_{i+2} e^{\imath(\psi_i-\psi_{i+2})}\right)\\ & -2\alpha\delta\mathcal{B}\left(A_{(i+1)^-} e^{-\imath\psi_{i+2}} + A_{(i+2)^-} e^{-\imath\psi_{i+1}}\right) + \text{nct.}\,, \qquad (58)\end{aligned}$$

where the indices are cyclic i.e. $i+3=i$. These amplitude equations have stripe-like solutions as well as solutions with a rhombic layout of the form $\mathcal{A}_1 = \mathcal{A}_{1^-} = \mathcal{A}_2 = \mathcal{A}_{2^-}$, $\mathcal{A}_3 = \mathcal{A}_{3^-}$. For both solutions the stationary phases depend on the inter-map coupling strength α. In this case stationary solutions of Eq. (58) are calculated numerically using a Newton method and initial conditions close to these solutions. In contrast to the case of OD stripes and OD constant solutions the amplitude equations (58) have an additional type of PWC solution which have uniform amplitudes, $A_j = \mathcal{A}e^{\imath\phi_i}$. The dynamics of their phases is given by

$$\begin{aligned}\partial_t\, \phi_i \;=\;& 2\mathcal{A}^2 \sum_{j\neq i} \sin\left(\phi_i + \phi_{i^-} - \phi_j - \phi_{j^-}\right)\\ & -\mathcal{B}^2\alpha \sum_{j\neq i}\left(2\sin\left(\phi_i - \phi_j - \psi_i + \psi_j\right) + 2\sin\left(\phi_i - \phi_{j^-} - \psi_i - \psi_j\right)\right)\\ & -\mathcal{B}^2\alpha \sin\left(\phi_i - \phi_{i^-} - 2\psi_i\right)\\ & -2\delta\alpha\mathcal{B}\left(\sin\left(\phi_i - \phi_{(i+1)^-} + \psi_{i+2}\right) + \sin\left(\phi_i - \phi_{(i+2)^-} + \psi_{i+1}\right)\right)\,. \qquad (59)\end{aligned}$$

When solving the amplitude equations numerically we observe that the phase relations vary with the inter-map coupling strength for non-uniform solutions. But for the uniform solution the phase relations are independent of the inter-map coupling strength. The phases of the uniform solution are determined up to a free phase φ which results from the orientation shift symmetry $z \to z\, e^{\imath\varphi}$ of Eq. (10). We therefore choose $\phi_1 = \psi_1$. As an ansatz for the uniform solutions we use

$$\begin{aligned}\mathcal{A}_j &= \mathcal{A}_{j^-} = \mathcal{A}, \quad j = 1,2,3\\ \phi_j &= \psi_j + (j-1)2\pi/3 + \Delta\,\delta_{j,2}\\ \phi_{j^-} &= -\psi_j + (j-1)2\pi/3 + \Delta\ (\delta_{j,1} + \delta_{j,3})\,, \qquad (60)\end{aligned}$$

where $\delta_{i,j}$ is the Kronecker delta and Δ a constant parameter. Note, that $z(\mathbf{x})$ cannot become real since $\phi_j \neq -\phi_{j^-}$. The equation for the uniform amplitudes is then given by

$$\partial_t\, \mathcal{A} = r_z\mathcal{A} - 9\mathcal{A}^3 - 4\alpha\mathcal{B}^2\mathcal{A} - \alpha\delta^2\mathcal{A} + \mathcal{A}\mathcal{B}\alpha\left(\mathcal{B} - 2\delta\right)\cos\Delta\,, \qquad (61)$$

while the phase dynamics reads

$$\partial_t\phi_j = -\mathcal{B}\alpha\left(\mathcal{B} - 2\delta\right)\sin\Delta\,. \qquad (62)$$

The stationarity condition is fulfilled for an arbitrary δ only if $\Delta = 0$ or $\Delta = \pi$. The corresponding amplitudes are given by solving the stationarity condition for the real part and read

$$\mathcal{A}_{\Delta=0} = \sqrt{\frac{r_z - \alpha\left(3\mathcal{B}^2 + 2\mathcal{B}\delta + \delta^2\right)}{9}}\,, \quad \mathcal{A}_{\Delta=\pi} = \sqrt{\frac{r_z - \alpha\left(5\mathcal{B}^2 - 2\mathcal{B}\delta + \delta^2\right)}{9}}\,. \qquad (63)$$

We calculate the stability properties of all solutions by linear stability analysis considering perturbations of the amplitudes $\mathcal{A}_j \to \mathcal{A} + a_j$, $\mathcal{A}_{j^-} \to \mathcal{A} + a_{j^-}$ and of the phases $\phi_j \to \phi_j + \varphi_j$, $\phi_{j^-} \to \phi_{j^-} + \varphi_{j^-}$. This leads to a perturbation matrix M. Amplitude and phase perturbations in general do not decouple. We calculated the eigenvalues of the perturbation M matrix numerically and checked the results by

direct numerical simulation of the amplitude equations. In case of the uniform solutions Eq. (60) the perturbation matrix M is explicitly stated in the appendix.
The stability of the $\Delta = 0$and $\Delta = \pi$ uniform solutions depends on the coupling strength α and on the sign of $(\mathcal{B} - 2\delta)$. As the solution of $B(\gamma) = 2\delta(\gamma)$ is given by $\gamma = \gamma^*$ in the stability range of OD hexagons there is only one possible stable uniform solution, the $\Delta = \pi$ uniform solution. This solution ceases to exist at $r_z < \alpha\left(5\mathcal{B}^2 - 2\mathcal{B}\delta + \delta^2\right)$. This existence border is in fact independent of the bias γ and given by

$$\alpha_c = 3r_z/r_o\,. \tag{64}$$

Thus the limit $r_z \to 0$ makes the uniform solution unstable for smaller and smaller coupling strengths.

Bifurcation diagram

The course of OP solutions when interacting with OD stripes is shown in Fig. 3**A,B**. In case of OP stripes inter-map coupling suppresses the amplitude A_1 of the stripe pattern while increasing the amplitude of the opposite mode A_{1^-}. This transformation reduces the representation of all but two preferred orientations. When both amplitudes collapse the resulting OP map is selective only to two orthogonal orientations namely $\vartheta = \phi_1$ and $\vartheta = \phi_1 + \pi/2$. We refer to these unrealistic solutions as *orientation scotoma solutions*. The phase relations ensure that OD borders that run parallel to the OP stripes are located at the OP maxima and minima i.e. in the center of the orientation scotoma stripes. With increasing inter-map coupling, this orientation scotoma pattern is suppressed until finally all amplitudes are zero and only the homogeneous solution is stable. In case of OP rhombs inter-map coupling makes the rhombic pattern more stripe-like by reducing the amplitude $A_2 = A_{2^-}$. The mode $A_3 = A_{3^-}$ which is zero in the uncoupled case increases and finally collapses with the mode A_2. Increasing inter-map coupling more suppresses all but the two modes $A_1 = A_{1^-}$, leading again to the orientation scotoma stripe pattern.
The parameter dependence of OP solutions when interacting with OD hexagons is shown in Fig. 3**C,D**. OP stripe solutions became above a critical inter-map coupling strength unstable against PWC solutions. This critical coupling strength strongly depended on the OD bias. OP rhombic solutions also became unstable against PWC but for a lower coupling strength than the OP stripes. Thus there is at intermediate coupling strength a bistability between stripe-like solutions and PWC solutions. The potential of the OP stripe and OP rhombic solutions is shown in Fig. 3**E,F**. Stripes are energetically preferred in the uncoupled case as well as for small inter-map coupling strength for which they are stable.
To summarize, stripe solutions were deformed but no pinwheels were created for this solution. The rhombic solutions were energetically not preferred for low inter-map coupling whereas for intermediate inter-map coupling these solutions lose pinwheels and became stripe solutions. Instead, additional pinwheel rich solutions with a crystal layout became stable for intermediate inter-map coupling. For large inter-map coupling orientation selectivity was completely suppressed.

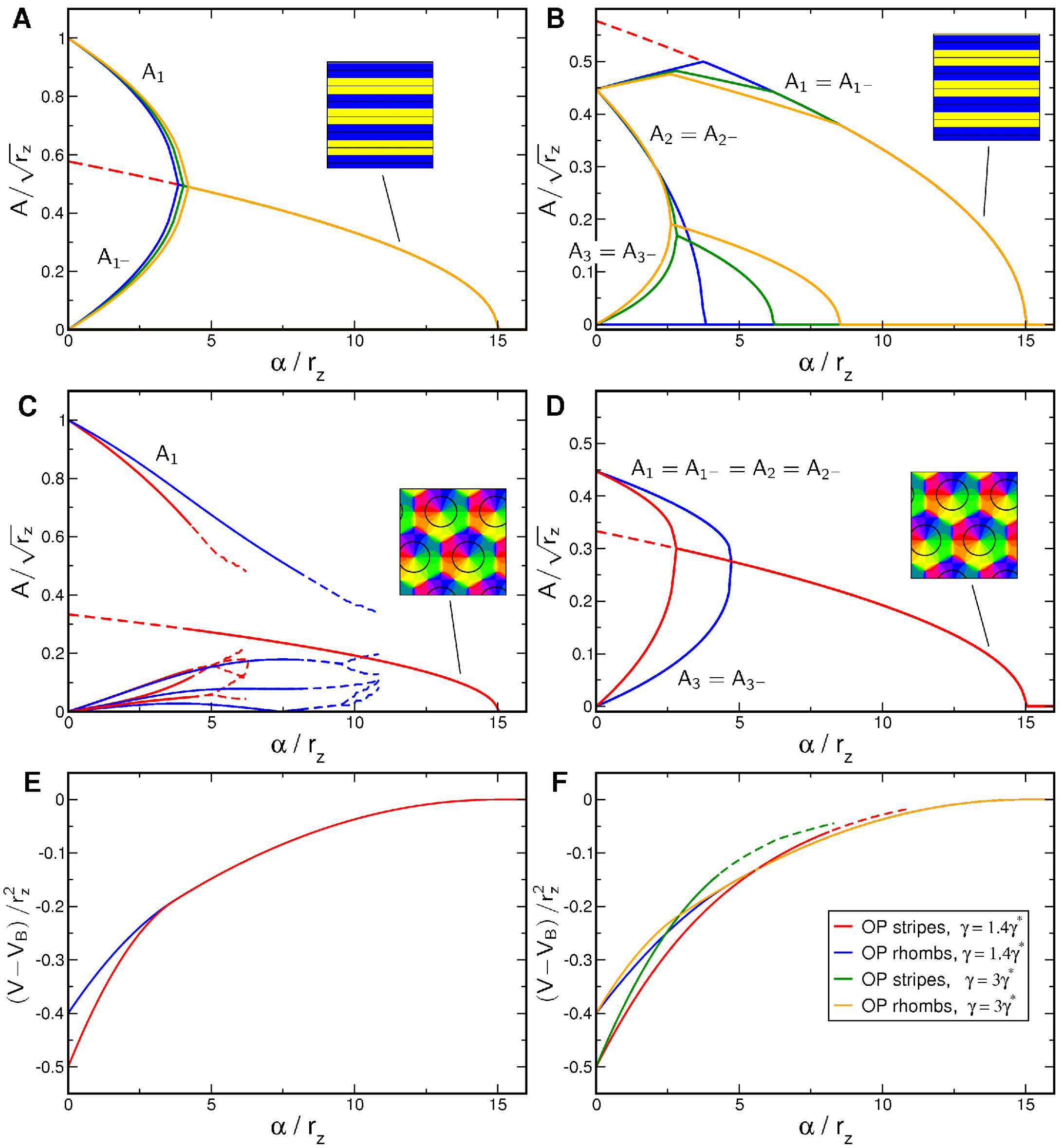

Figure 3. Stationary amplitudes with coupling energy $\mathbf{U} = \alpha\,|\mathbf{z}|^{\mathbf{2}}\mathbf{o}^{\mathbf{2}}$, $r_o = 0.2$. Solid (dashed) lines: stable (unstable) solutions to Eq. (49) (OD stripes) and Eq. (58) (OD hexagons). **A,B** OD stripes, $\gamma = 0$ (blue), $\gamma = \gamma^*$ (green), $\gamma = 1.4\gamma^*$ (orange). **C,D** OD hexagons, $\gamma = 1.4\gamma^*$ (blue), $\gamma = 3\gamma^*$ (red). **E** Potential for OP stripes (red) and OP rhombs (blue) interacting with OD stripes, $\gamma = 0$. **F** Potential for OP stripes and OP rhombs interacting with OD hexagons.

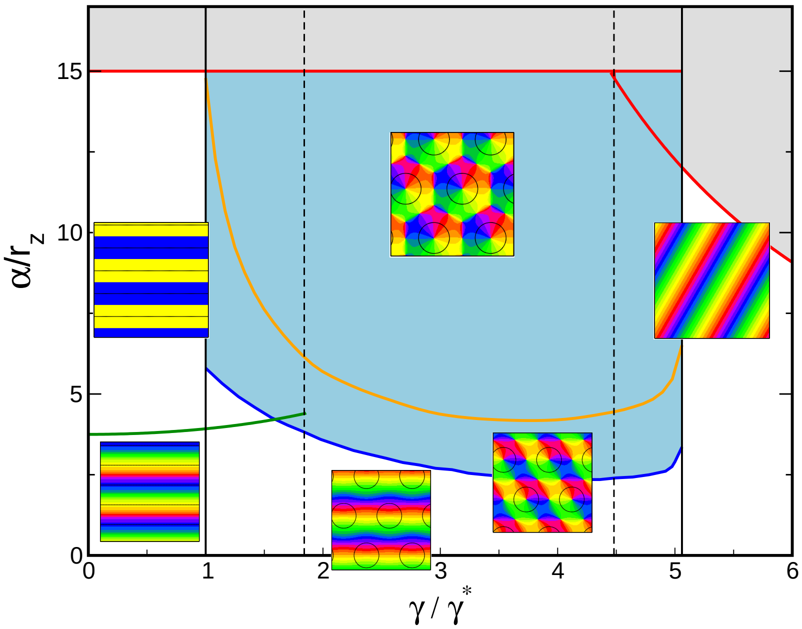

Figure 4. Phase diagram with the coupling energy $\mathbf{U} = \alpha\,\mathbf{o^2|z|^2}$, $r_o = 0.2, r_z \ll r_o$. Vertical lines: stability range of OD stripes, hexagons, and constant solution. Green line: transition to the orientation scotoma solution. Blue line: stability border for the $\Delta = \pi$ uniform solution (hPWC). Orange line: stability line of stripe-like solutions. Red line: pattern solutions ceases to exist, see Eq. (52) and Eq. (64). Blue region: stability region of hPWC, gray region: No pattern solution stable.

Phase diagram

The phase diagram as a function of the OD bias γ and the inter-map coupling strength α for this coupling energy is shown in Fig. 4. When rescaling the inter-map coupling strength as α/r_z the phase diagram is independent of the bifurcation parameter of the OP map r_z. Thus for fixed $r_o \gg r_z$ the phase diagram depends only on two control parameters γ/γ^* and α/r_z. The phase diagram contains the stability borders of the uncoupled OD solutions $\gamma^*, \gamma_2^*, \gamma_3^*, \gamma_4^*$. They correspond to vertical lines, as they are independent of the inter-map coupling in the limit $r_z \ll r_o$. At $\gamma = \gamma^*$ hexagons become stable. Stripe solutions become unstable at $\gamma = \gamma_2^*$. At $\gamma = \gamma_3^*$ the homogeneous solution becomes stable while at $\gamma = \gamma_4^*$ hexagons lose their stability. In the units γ/γ^* the borders $\gamma_2^*, \gamma_3^*, \gamma_4^*$ vary slightly with r_o , see Fig. 26, and are drawn here for $r_o = 0.2$. Colored lines correspond to the stability and existence borders of OP solutions. In the region of stable OD stripes the OP stripes run parallel to the OD stripes. With increasing inter-map coupling strength the orientation preference of all but two orthogonal orientations is suppressed. In the region of stable OD hexagons stripe-like OP solutions dominate for low inter-map coupling strength. Above a critical bias dependent coupling strength the $\Delta = \pi$ uniform solution becomes stable (blue line). There is a region of bistability between stripe-like and uniform solutions until the stripe-like solutions lose their stability (orange line). OP rhombic solutions lose their stability when the uniform solution becomes stable. Thus there is no bistability between OP rhombs and OP uniform solutions. As in the case of OD stripes the uniform solution becomes unstable at $\alpha = r_z/(3\mathcal{B}^2)$. Also in the case of OD hexagons the inter-map coupling leads to a transition towards the trivial solution where there is no OP pattern at all. In case of the OD constant solution the OP map is a stripe solution. Pinwheel rich solutions thus occur only in the region of stable OD hexagons. In the following we discuss the properties of these solutions.

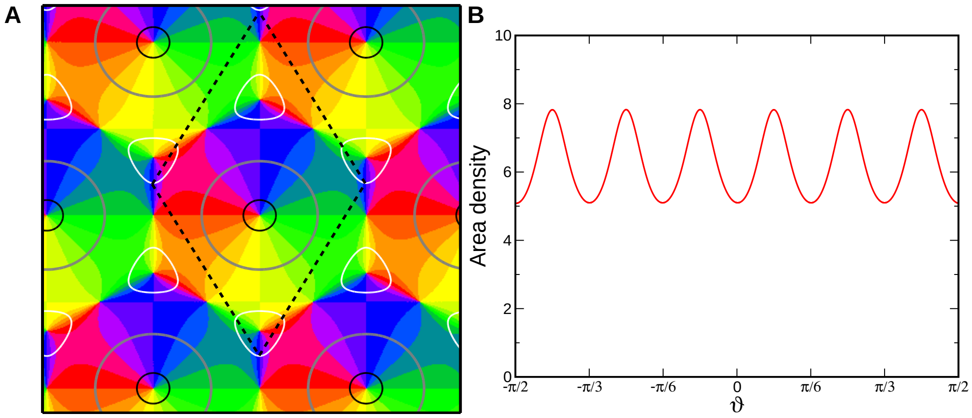

Figure 5. Ipsi-center pinwheel crystal. **A** OP map, superimposed are the OD borders (gray), 90% ipsilateral eye dominance (black), and 90% contralateral eye dominance (white), $r_o = 0.2, \gamma = 3\gamma^*$. Dashed lines mark the unit cell of the regular pattern. **B** Distribution of preferred orientations.

Interaction induced pinwheel crystals

The uniform solution Eq. (60) with $\Delta = \pi$ is illustrated in Fig. 5. For all stationary solutions the positions of the pinwheels are fixed by the OD map and there are no translational degrees of freedom. The unit cell (dashed line) contains 6 pinwheels which leads to a pinwheel density of $\rho = 6\,\cos\pi/6 \approx 5.2$. Two of them are located at OD maxima (contra center) while one is located at an OD minimum (ipsi center). The remaining three pinwheels are located at OD saddle-points. Therefore, all pinwheels are located where the gradient of the OD map is zero. The pinwheel in the center of the OP hexagon is at the ipsilateral OD peak. Because these pinwheels organize most of the map while the others essentially only match one OP hexagon to its neighbors we refer to this pinwheel crystal as the *Ipsi-center pinwheel crystal*. The iso-orientation lines intersect the OD borders (gray) exactly with a right angle. The intersection angles are, within the stability range of OD hexagons, independent of the bias γ. The remarkable property of perfect intersection angles cannot be deduced directly from the coupling energy term. The solution is symmetric under a combined rotation by 60° and an orientation shift by $-60°$. The symmetry of the pattern is reflected by the distribution of preferred orientations, see Fig. 5**B**. Although the pattern is selective to all orientations the six orientations $\vartheta + n\frac{\pi}{6}$, $n = 0, ..., 5$ are slightly overrepresented.

To summarize, the low order product-type inter-map coupling leads in case of OD hexagons to a transition from pinwheel free stripe solutions towards pinwheel crystals. The design of the PWC is an example of an orientation hypercolumn dominated by one pinwheel. With increasing inter-map coupling the PWC solution is suppressed until only the homogeneous solution is stable. In case of OD stripes or the constant solution the OP solutions are pinwheel free stripe pattern.

Gradient-type energy $U = \beta|\nabla z \nabla o|^2$

When using a gradient-type inter-map coupling energy the interaction terms are independent of the OD shift δ. In this case, the coupling strength can be rescaled as $\beta\mathcal{B}^2$ and is therefore independent of the bias γ. The bias in this case only determines the stability of OD stripes, hexagons or the constant solution.

Stationary solutions and their stability

A coupling to OD stripes is easy to analyze in the case of a gradient-type inter-map coupling. The energetically preferred solutions are OP stripes with the direction perpendicular to the OD stripes for which $U = 0$. This configuration corresponds to the Hubel and Wiesel Ice-cube model [45]. In addition there are rPWC solutions with the stationary amplitudes $\mathcal{A}_1 = \mathcal{A}_{1^-} = \sqrt{(r_z + 2\mathcal{B}^2\beta)/5}$, $\mathcal{A}_2 = \mathcal{A}_{2^-} = \sqrt{(r_z - \mathcal{B}^2\beta)/5}$, $\mathcal{A}_3 = \mathcal{A}_{3^-} = 0$, and the stationary phases as in Eq. (53). Increasing inter-map coupling strength β leads to an increase of the amplitudes $\mathcal{A}_1 = \mathcal{A}_{1^-}$ while decreasing the amplitudes $\mathcal{A}_2 = \mathcal{A}_{2^-}$ thus making the rhombic solution more stripe-like.

In the case the OD map is a constant, Eq. (117), the gradient-type inter-map coupling leaves the OP dynamics unaffected. The stationary states are therefore OP stripes with an arbitrary direction and rPWC solutions as in the uncoupled case.

In the case of OD hexagons the amplitude equations read

$$\begin{aligned} \partial_t\, A_i \;=\;& \left(r_z - 3\beta\mathcal{B}^2\right) A_i + \frac{5}{4}\beta\mathcal{B}^2 \left(A_{i+1} e^{\imath(\psi_i - \psi_{i+1})} + A_{i+2} e^{\imath(\psi_i - \psi_{i+2})}\right) \\ & - \beta\mathcal{B}^2 \left(A_{i^-} e^{2\imath\psi_i} + \frac{5}{4} A_{(i+1)^-} e^{\imath(\psi_i + \psi_{i+1})} + \frac{5}{4} A_{(i+2)^-} e^{\imath(\psi_i + \psi_{i+2})}\right) + \text{nct.}\,. \end{aligned} \tag{65}$$

Using $A_i = \mathcal{A}_i e^{\imath\phi_i}$ we obtain the phase equations

$$\begin{aligned} \mathcal{A}_i \partial_t\, \phi_i \;=\;& \sum_{j \neq i} \mathcal{A}_j \mathcal{A}_{j^-} \mathcal{A}_{i^-} \sin\left(\phi_i + \phi_{i^-} - \phi_j - \phi_{j^-}\right) \\ & - \mathcal{B}^2\beta \sum_{j \neq i} \left(\frac{5}{4}\mathcal{A}_j \sin\left(\phi_i - \phi_j - \psi_i + \psi_j\right) + \frac{5}{4}\mathcal{A}_{j^-} \sin\left(\phi_i - \phi_{j^-} - \psi_i - \psi_j\right)\right) \\ & - \mathcal{B}^2\beta\mathcal{A}_{i^-} \sin\left(\phi_i - \phi_{i^-} - 2\psi_i\right)\,. \end{aligned} \tag{66}$$

These amplitude equations have stripe-like and rhombic solutions with inter-map coupling dependent phase relations. We therefore calculate their stationary phases and amplitudes numerically using a Newton method and initial conditions close to these solutions. Besides stripe-like and rhombic solutions these amplitude equations have uniform solutions. Again we find that the ansatz Eq. (60) can satisfy the stationarity condition. The phase dynamics in this case reads

$$\partial_t\, \phi_i = -\frac{1}{4}\mathcal{B}^2\beta \sin\Delta\,. \tag{67}$$

As in the case of the product-type inter-map coupling energy stationary solutions are $\Delta = 0$ and $\Delta = \pi$ with the stationary amplitudes

$$\mathcal{A}_{\Delta=0} = \sqrt{\frac{r_z - 3/2\mathcal{B}^2\beta}{9}}\,, \quad \mathcal{A}_{\Delta=\pi} = \sqrt{\frac{r_z - 2\mathcal{B}^2\beta}{9}}\,. \tag{68}$$

We studied the stability properties of both stationary solutions by linear stability analysis where amplitude and phase perturbations in general do not decouple. The stability matrix of the uniform solutions is given in the appendix. The eigenvalues are calculated numerically. It turned out that the $\Delta = \pi$ solution is unstable for $\beta > 0$ while the $\Delta = 0$ solution becomes stable for $\beta \approx 0.05 r_z/\mathcal{B}^2$. The $\Delta = 0$ solution loses its stability above

$$\beta_c\, \mathcal{B}^2 = 2r_z/3\,. \tag{69}$$

From thereon only the homogeneous solution $A_j = 0$ is stable.

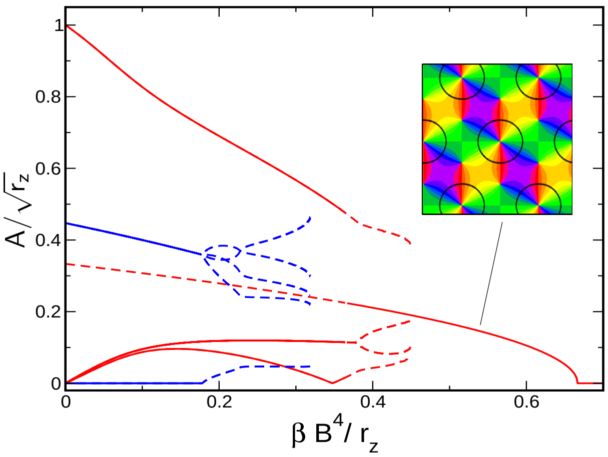

Figure 6. Stationary amplitudes with $\mathbf{U} = \beta|\nabla \mathbf{z} \nabla \mathbf{o}|^2$ and OD hexagons. Solid (dashed) lines: Stable (unstable) solutions to Eq. (65). Transition from OP stripes towards the uniform solution (red), transition from OP rhombs towards the uniform solution (blue).

Bifurcation diagram

The course of the stationary amplitudes when interacting with OD hexagons is shown in Fig. 6. The OP rhombic solution is almost unchanged by inter-map coupling but above a critical coupling strength the rhombs decay into a stripe-like solution. The amplitude of the OP stripe solution is suppressed by inter-map coupling and finally becomes unstable against the $\Delta = 0$ uniform solution. Thus for large inter-map coupling only the uniform solution is stable. A further increase in the inter-map coupling suppresses the amplitude of this uniform solution until finally only the homogeneous solution is stable.

Phase diagram

The phase diagram of this coupling energy is shown in Fig. 7. We rescaled the inter-map coupling strength as $\beta\mathcal{B}^2/r_z$, where $\mathcal{B}$ is the stationary amplitude of the OD hexagons. The stability borders are then independent of the OD bias in the OD solutions and further independent of the bifurcation parameter r_z. This simplifies the analysis since the OP solutions and their stability depend on γ only indirect via the amplitudes B. In case of OD stripes or OD constant solution there is no pinwheel crystallization. Instead the OP solutions are pinwheel free stripes. In case of OD hexagons hPWCs become stable above $\beta \approx 0.05 r_z/\mathcal{B}^2$ (blue line). Rhombic OP patterns become unstable at $\beta\mathcal{B}^4/r_z \approx 0.17$ and decay into a stripe-like solution (green line). At $\beta\mathcal{B}^4/r_z \approx 0.36$ these stripe-like solutions become unstable (orange line). Thus above $\beta\mathcal{B}^4/r_z \approx 0.36$ the hPWC is the only stable solution. At $\beta\mathcal{B}^2/r_z = 2/3$ the pattern solution ceases to exist (red line).

Interaction induced pinwheel crystals

The uniform solution Eq. (60), $\Delta = 0$ is illustrated in Fig. 8. This PWC contains only three pinwheels per unit cell leading to a pinwheel density of $\rho = 3\cos\pi/6 \approx 2.6$. Two of the three pinwheels are located at maxima of the OD map (contra peak) while the remaining pinwheel is located at the minimum (ipsi peak) of the OD map. A remarkable property of this solution is that the pinwheel located at the OD minimum, carries a topological charge of 1 such that each orientation is represented twice around this pinwheel. Pinwheels of this kind have not yet been observed in experimentally recorded OP maps. This

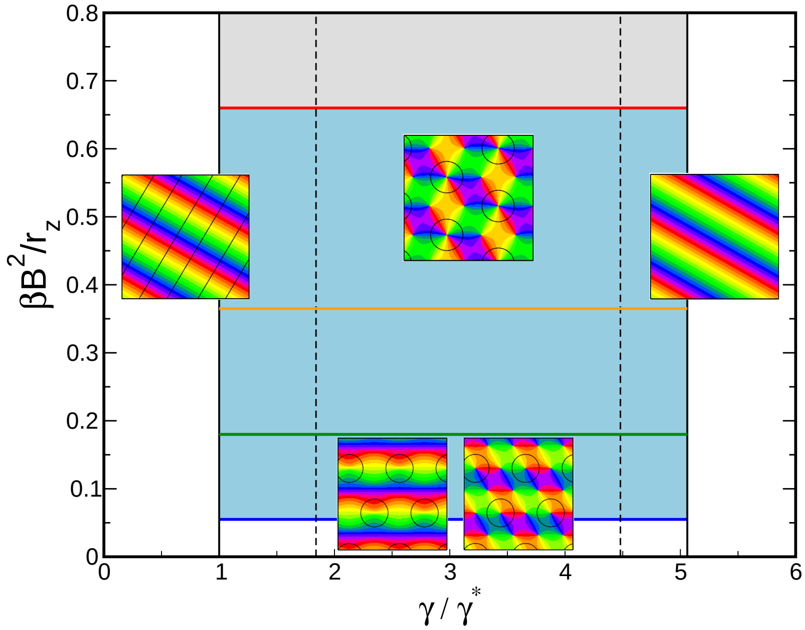

Figure 7. Phase diagram with the coupling energy $\mathbf{U} = \beta|\nabla \mathbf{z} \nabla \mathbf{o}|^{\mathbf{2}}$, $r_z \ll r_o$. Vertical black lines: stability range of OD stripes, hexagons, and constant solution. Blue line: stability border for the $\Delta = 0$ uniform solution. Green line: rhombic solutions become unstable. Orange line: stripe-like solutions become unstable. Red line: pattern solutions cease to exist, see Eq. (68). Gray region: No pattern solution stable.

kind of uniform solution corresponds to the structural pinwheel model by Braitenberg [60]. We therefore refer to this solution as the *Braitenberg pinwheel crystal*.

The iso-orientation lines are again perfectly perpendicular to OD borders and this is independent of the bias γ. The solution is symmetric under a combined rotation by 120° and an orientation shift by $-2\pi/3$. Further it is symmetric under a rotation by 180°. The pattern is selective to all orientations but the distribution of represented orientations is not uniform. The three orientations $\vartheta + n\frac{\pi}{3}$, $n = 0, ..., 2$ are overrepresented, see Fig. 8**B**.

Overall this OP map is dominated by uniform regions around hyperbolic points. In contrast to the ipsi center PWC all pinwheels in this OP map organize a roughly similar fraction of the cortical surface.

The impact of inter-map coupling: Higher order coupling terms

In the last section we demonstrated that the low order coupling terms can lead to a complete suppression of OP selectivity. As the coupling terms are effectively linear they not only influence pattern selection but also whether there is a pattern at all. This is in general not the case for higher order coupling energies using the amplitude equations Eq. (42). In this case the coupling is an effective cubic interaction term and complete selectivity suppression is impossible. Moreover, we could identify the limit $r_z \ll r_o$ in which the backreaction onto the OD map formally becomes negligible. When using the higher order inter-map

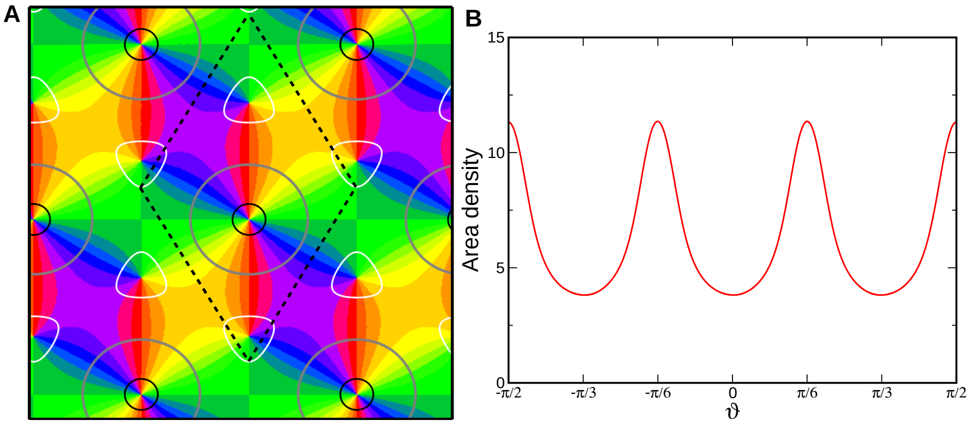

Figure 8. The Braitenberg pinwheel crystal, $\Delta = 0$ uniform solution of Eq. (60). **A** OP map, superimposed are the OD borders (gray), 90% ipsilateral eye dominance (black), and 90% contralateral eye dominance (white), $r_o = 0.2, \gamma = 3\gamma^*$. Dashed lines mark the unit cell of the regular pattern. **B** Distribution of preferred orientations.

coupling terms and assuming $B_i = \mathcal{B}e^{\imath\psi_i}$ the potential reads

$$\begin{aligned} V \quad = \quad & V_A + V_B + \\ & + \epsilon\mathcal{B}^4 \sum_{ijlk}^{3} \Big(h^{(1)}_{ijlk} A_j A_l \overline{A}_k \overline{A}_i + h^{(2)}_{ijlk} A_{j^-} A_{l^-} \overline{A}_{k^-} \overline{A}_i + h^{(3)}_{ijlk} A_j A_{l^-} \overline{A}_k \overline{A}_i \\ & + h^{(4)}_{ijlk} A_{j^-} A_{l^-} \overline{A}_k \overline{A}_i + h^{(5)}_{ijlk} A_j A_l \overline{A}_{k^-} \overline{A}_i + h^{(6)}_{ijlk} A_j A_{l^-} \overline{A}_{k^-} \overline{A}_i \\ & + \tilde{h}^{(1)}_{ijlk} A_{j^-} A_{l^-} \overline{A}_{k^-} \overline{A}_{i^-} + \tilde{h}^{(3)}_{ijlk} A_{j^-} A_l \overline{A}_{k^-} \overline{A}_{i^-} + \tilde{h}^{(4)}_{ijlk} A_j A_l \overline{A}_{k^-} \overline{A}_{i^-} \Big) \,, \end{aligned} \tag{70}$$

where $\tilde{h}^{(u)}_{ijlk}, u = 1, 3, 4$ is given by the coefficient $h^{(u)}_{ijlk}$ for which all phases ψ_m are replaced by $-\psi_m$. The amplitude equations can be derived from a potential given by

$$\begin{aligned} \partial_t\, A_i \quad = \quad & r_z\, A_i - \sum_{j}^{3} g_{ij} |A_j|^2 A_i - \sum_{j \neq i}^{3} f_{ij} A_j A_{j^-} \overline{A}_{i^-} \\ & - \mathcal{B}^4 \sum_{j,l,k}^{3} \Big(h^{(1)}_{ijlk} A_j A_l \overline{A}_k + h^{(2)}_{ijlk} A_{j^-} A_{l^-} \overline{A}_{k^-} + h^{(3)}_{ijlk} A_j A_{l^-} \overline{A}_k \\ & + h^{(4)}_{ijlk} A_{j^-} A_{l^-} \overline{A}_k + h^{(5)}_{ijlk} A_j A_l \overline{A}_{k^-} + h^{(6)}_{ijlk} A_j A_{l^-} \overline{A}_{k^-} \Big) \,, \end{aligned} \tag{71}$$

with $g_{ii} = 1$, $g_{ij} = 2$ and $h^{(u)}_{ijlk}$ effective self-interaction coupling coefficients given in the Appendix. We have not written terms containing the constant δ for simplicity. The phases ψ_j are absorbed into the coupling coefficients. The dynamics for the modes A_{i^-} is given by interchanging A_i and A_{i^-}. For negligible backreaction $\mathcal{B} = \mathcal{B}_{hex}$, $\mathcal{B} = \mathcal{B}_{st}$, or $\mathcal{B} = \mathcal{B}_c$. In the following we identify classes of stationary solutions of the amplitude equations Eq. (71) and provide their stability criteria for the two higher order pendants of the coupling energies.

Product-type energy $U = \tau\, o^4 |z|^4$

First, we studied the higher order product-type inter-map coupling energy in Eq. (23). As for the lower order version of this coupling energy the shift $\delta(\gamma)$ explicitly enters the amplitude equations resulting in a rather complex parameter dependence.

Stationary solutions and their stability

In the case of OD stripes the amplitude equations of OP modes read

$$\begin{aligned}
\partial_t\, A_1 \;&=\; r_z A_1 - \sum_j \left(g^{(1)}_{1j} |A_j|^2 A_1 + g^{(2)}_{1j} |A_j|^2 A_{1^-} + g^{(3)}_{1j} A_j A_{j^-} \overline{A}_{1^-} + g^{(4)}_{1j} A_j A_{j^-} \overline{A}_1 \right) \\
&\quad - B^4 A^2_{1^-} \overline{A}_1 - \sum_{u \neq v \neq w} A_u A_v \overline{A}_w \Big(\left(8\delta^3 B + 24\delta B^2 \overline{B} \right) \delta_{\vec{k}_u + \vec{k}_v - \vec{k}_w, 0} \qquad (72) \\
&\quad + \left(8\delta^3 \overline{B} + 24\delta B \overline{B}^2 \right) \delta_{\vec{k}_u + \vec{k}_v - \vec{k}_w, 2\vec{k}_1} + 8\delta B^3 \delta_{\vec{k}_u + \vec{k}_v - \vec{k}_w, -2\vec{k}_1} \Big) \\
\partial_t\, A_2 \;&=\; r_z A_2 - \sum_j \left(g^{(1)}_{2j} |A_j|^2 A_2 + g^{(3)}_{2j} A_j A_{j^-} \overline{A}_{2^-} \right) \\
&\quad - g^{(2)}_{ii} A_2 A_{1^-} \overline{A}_1 - g^{(5)} A_2 A_1 \overline{A}_{1^-} - 1/2 g^{(2)}_{ii} A^2_{1^-} \overline{A}_{2^-} - 1/2 g^{(5)} A^2_1 \overline{A}_{2^-} \\
&\quad - \sum_{u,v,w} A_u A_v \overline{A}_w \Big(g^{(6)}_{uv} \delta_{\vec{k}_u + \vec{k}_v - \vec{k}_w, \vec{k}_2} + g^{(7)}_{ij} \delta_{\vec{k}_u + \vec{k}_v - \vec{k}_w, \vec{k}_1 + \vec{k}_2} \\
&\quad + g^{(8)}_{ij} \delta_{\vec{k}_u + \vec{k}_v - \vec{k}_w, -\vec{k}_1 + \vec{k}_2} + g^{(9)}_{ij} \delta_{\vec{k}_u + \vec{k}_v - \vec{k}_w, 2\vec{k}_1 + \vec{k}_2} + g^{(10)}_{ij} \delta_{\vec{k}_u + \vec{k}_v - \vec{k}_w, -2\vec{k}_1 + \vec{k}_2} \Big)\,,
\end{aligned}$$

where $\delta_{i,j}$ denotes the Kronecker delta and

$$\begin{array}{rcl}
g^{(1)}_{ii} = & 1 + \delta^4 + 12\delta^2 |B|^2 + 6|B|^4, & g^{(1)}_{ij \neq i} = 2 g^{(1)}_{ii}, \\
g^{(2)}_{ii} = & g^{(2)}_{ij \neq i} = 12\delta^2 B^2 + 8B^3 \overline{B}, & \\
g^{(3)}_{ii} = & 0, & g^{(3)}_{ij \neq i} = 2 + 12|B|^4 + 24\delta^2 |B|^2 + 2\delta^4, \\
g^{(4)}_{ii} = & 0, & g^{(4)}_{ij \neq i} = 12\delta^2 B^2 + 8B^3 \overline{B}, \\
g^{(5)} = & 12\delta^2 \overline{B}^2 + 8B\overline{B}^3, & g^{(6)}_{uu} = 6|B|^4 + 6\delta |B|^2,\ g^{(6)}_{uv \neq u} = 2 g^{(6)}_{uu}, \\
g^{(7)}_{uu} = & 4\overline{B}\delta^3 + 1B\overline{B}^2 \delta, & g^{(7)}_{uv \neq u} = 2 g^{(7)}_{uu}, \\
g^{(8)}_{uu} = & 4B\delta^3 + 1B^2 \overline{B}\delta, & g^{(8)}_{uv \neq u} = 2 g^{(8)}_{uu}, \\
g^{(9)}_{uu} = & 6\overline{B}^2 \delta^2, & g^{(9)}_{uv \neq u} = 2 g^{(9)}_{uu}, \\
g^{(10)}_{uu} = & 6B^2 \delta^2, & g^{(10)}_{uv \neq u} = 2 g^{(10)}_{uu}.
\end{array}$$

The equation for the mode A_3 is given by interchanging the modes A_2 and A_3 in Eq. (72). The equations for the modes A_{i^-} are given by interchanging the modes A_i and A_{i^-} and interchanging the modes B_i and $\overline{B}_i$.
In this case, at low inter-map coupling the OP stripes given by

$$z = \mathcal{A}_1 e^{\imath \left(\vec{k}_1 \vec{x} + \phi_1 \right)} - \mathcal{A}_{1^-} e^{-\imath \left(\vec{k}_1 \vec{x} + \phi_{1^-} \right)}\,, \qquad (73)$$

with $\phi_1 - \phi_{1^-} = 2\psi_1 + \pi$ run parallel to the OD stripes. Their stationary amplitudes are given by

$$\begin{aligned}
A_1^2 \;&=\; \left(u - v - \sqrt{u^2 - 2uv + v^2 - 16w^2} \right)^2 x/32w \\
A_{1^-} \;&=\; x/2\,, \qquad (74)
\end{aligned}$$

with $x = r_z\left(u - v + \sqrt{u^2 - 2uv + v^2 - 16w^2}\right)/(uv - v^2 - 8w^2)$, $u = 2 + 13\mathcal{B}^4\tau + 24\mathcal{B}^2\delta^2\tau + 2\delta^4\tau$, $v = (6\mathcal{B}^4 + 12\mathcal{B}^2\delta^2 + \delta^4)\tau$, $w = (2\mathcal{B}^2 + 3\delta^2)\tau\mathcal{B}^2$. The parameter dependence of these stripe solutions is shown in Fig. 9**A**.

At large inter-map coupling the attractor states of the OP map consist of a stripe pattern containing only two preferred orientations, namely $\vartheta = \phi_1$ and $\vartheta = \phi_1 + \pi/2$. The zero contour lines of the OD map are along the maximum amplitude of orientation preference minimizing the energy term.

In addition there are rhombic solutions

$$z = \mathcal{A}_1 e^{\imath(\vec{k}_1\vec{x}+\psi_1)} + \mathcal{A}_{1^-} e^{-\imath(\vec{k}_1\vec{x}-\psi_1+\pi)} + \mathcal{A}_2 e^{\imath(\vec{k}_2\vec{x}+\psi_1)} + \mathcal{A}_{2^-} e^{-\imath(\vec{k}_2\vec{x}-\psi_1)}\,, \tag{75}$$

which exist also in the uncoupled case, see Fig. 9**B**. However, these rhombic solutions are energetically not favored compared to stripe solutions, see Fig. 9**C**. The inclusion of the inter-map coupling makes these rhombic solution even more stripe-like.

In case of a OD constant solution the amplitude equations read

$$\partial_t A_i = r_z A_i - \sum_j g_{ij}|A_j|^2 A_i - \sum_j f_{ij} A_j A_{j^-} \overline{A}_{i^-}\,, \tag{76}$$

with $g_{ii} = 1 + \delta^4\tau$, $g_{ij} = 2 + 2\delta^4\tau$ and $f_{ij} = 2 + 2\delta^4\tau$. Inter-map coupling thus leads to a renormalization of the uncoupled interaction terms. Stationary solutions are stripes with the amplitude

$$\mathcal{A} = \sqrt{\frac{r_z}{1 + \delta^4\tau}}\,, \tag{77}$$

and rhombic solutions with the stationary phases $\phi_1 + \phi_{1^-} - \phi_2 - \phi_{2^-} = \pi$ and the stationary amplitudes

$$\mathcal{A}_1 = \mathcal{A}_{1^-} = \mathcal{A}_2 = \mathcal{A}_{2^-} = \sqrt{r_z/(5 + 5\delta^4\tau)}\,. \tag{78}$$

In the case of OD hexagons we identify, in addition to stripe-like and rhombic solutions, uniform solutions $\mathcal{A}_i = \mathcal{A}$. When solving the amplitude equations numerically we have seen that the phase relations vary with the inter-map coupling strength τ for non-uniform solutions. But for the uniform solution the phase relations are independent of the inter-map coupling strength. When we use the ansatz Eq. (60) for uniform solutions we get the stationarity condition

$$6\mathcal{A}^2\mathcal{B}\left[4\left(-4B^3 + 7B^2\delta - B\delta^2 + \delta^3\right) + \mathcal{B}\cos\Delta\left(13B^2 - 8B\delta + 6\delta^2\right)\right]\sin\Delta = 0\,. \tag{79}$$

Four types of stationary solutions exist namely the $\Delta = 0, \Delta = \pi$, which we already observed in case of the low order energies, and the solutions

$$\Delta = \Delta(\gamma) = \pm\arccos\left(\frac{4(4\mathcal{B}^3 - 7\mathcal{B}^2\delta + \mathcal{B}\delta^2 - \delta^3)}{\mathcal{B}(13\mathcal{B}^2 - 8\mathcal{B}\delta + 6\delta^2)}\right)\,, \tag{80}$$

which depends on $\mathcal{B}$ and δ and thus on the bias γ. The course of Eq. (80) as a function of γ is shown in Fig. 10**B**. Stationary amplitudes for these solutions are given by

$$\begin{aligned}
\mathcal{A}^2_{\Delta=0} &= \frac{r_z}{3\tau\left(3/\tau + 33\mathcal{B}^4 + 56\mathcal{B}^3\delta + 50\mathcal{B}^2\delta^2 + 16\mathcal{B}\delta^3 + 3\delta^4\right)}\\
\mathcal{A}^2_{\Delta=\pi} &= \frac{r_z}{\tau\left(9/\tau + 483\mathcal{B}^4 - 504\mathcal{B}^3\delta + 246\mathcal{B}^2\delta^2 - 48\mathcal{B}\delta^3 + 9\delta^4\right)}\\
\mathcal{A}^2_{\Delta(\gamma)} &= \frac{r_z(13\mathcal{B}^2 - 8\mathcal{B}\delta + 6\delta^2)}{3\tau\left(411\mathcal{B}^6\tau + 704\mathcal{B}^5\delta\tau - 376\mathcal{B}^4\delta^2\tau + 32\mathcal{B}^3\delta^3\tau + 2\delta^2(9 - 7\delta^4\tau) - 39\mathcal{B}^2(3\delta^4\tau - 1) + 8\mathcal{B}\delta(5\delta^4\tau - 3)\right)}
\end{aligned} \tag{81}$$

We study the stability properties of OP stripe-like, rhombic and uniform solutions using linear stability analysis. The eigenvalues of the stability matrix , see appendix, are calculated numerically. Linear stability analysis shows that for $\tau \geq 0$ the $\Delta = 0$ solution is unstable for all bias values. The stability region of the $\Delta = \pi$ solution and the solution Eq. (80) is bias dependent. The bias dependent solution Eq. (80) is stable for $\gamma > \gamma^*$ and $\gamma < \gamma_c$ for which $\Delta = \pi$, see Fig. 10**B**. For larger bias $\gamma > \gamma_c$ only the $d = \pi$ uniform solution is stable.

Bifurcation diagram

The parameter dependence of OP solutions when interacting with OD stripes is shown in Fig. 9**A,B**. Similar to the low order variant of this coupling energy the amplitude of the stripes pattern A_1 is suppressed while the amplitude of the opposite mode A_{1^-} grows. Finally both amplitudes collapse, leading to an orientation scotoma solution. In contrast to the low order variant this stripe pattern is stable for arbitrary large inter-map coupling. In case of OP rhombic solutions inter-map coupling transforms this solution by reducing the amplitudes $A_2 = A_{2^-}$ while increasing the amplitudes $A_3 = A_{3^-}$. Without OD bias this solution is then transformed into the orientation scotoma stripe pattern, similar to the low order variant of this energy. In contrast to the low order energy, for non-zero bias the amplitudes A_2 and A_3 stay small but non-zero.

The parameter dependence of OP solutions when interacting with OD hexagons is shown in Fig. 9**C,D**. For a small OD bias ($\gamma = \gamma^*$) OP rhombic solutions decay into OP stripe-like patterns. These stripe-like patterns stay stable also for large-inter map coupling. In case of a larger OD bias ($\gamma = 3\gamma^*$), both the OP stripe and the OP rhombic solutions decay into the uniform PWC solution. Thus for small bias there is a bistability between stripe-like and uniform PWC solutions while for larger OD bias the uniform PWC solution is the only stable solution. The potential of OP stripe and OP rhombic solutions is shown in Fig. 9**E,F**. In the uncoupled case as well as for small inter-map coupling strength OP stripe solutions are for all bias values the energetic ground state. For large inter-map coupling and a small bias ($\gamma \approx \gamma^*$) rhombic solutions are unstable and the stripe-like solutions are energetically preferred compared to PWC solutions. For larger bias, however, PWC solutions are the only stable solutions for large inter-map coupling.

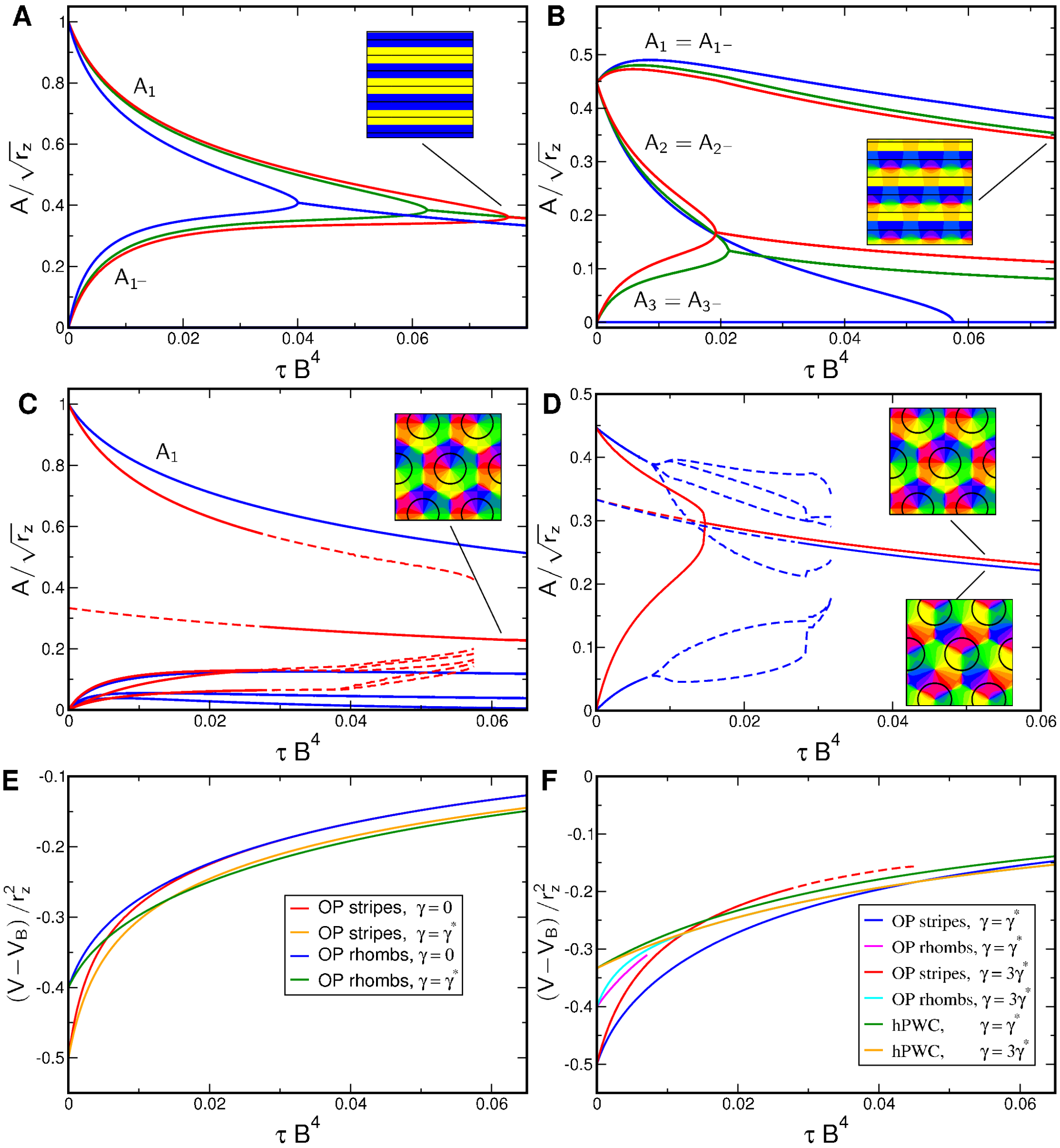

Figure 9. Stationary amplitudes with coupling energy $\mathbf{U} = \tau|\mathbf{z}|^4\mathbf{o}^4$. Solid (dashed) lines: stable (unstable) solutions to Eq. (71). **A,B** OD stripes, $\gamma = 0$ (blue), $\gamma = \gamma^*$ (green), $\gamma = 1.4\gamma^*$ (red). **A** OP stripe-like solutions, **B** OP rhombic solutions, **C,D** OD hexagons, $\gamma = \gamma^*$ (blue), $\gamma = 3\gamma^*$ (red). **C** OP stripe-like solutions, **D** OP rhombic solutions, **E** Potential, Eq. (70), of OP stripes and OP rhombs interacting with OD stripes. **F** Potential, Eq. (70), of OP stripes, OP rhombs, and hPWC interacting with OD hexagons.

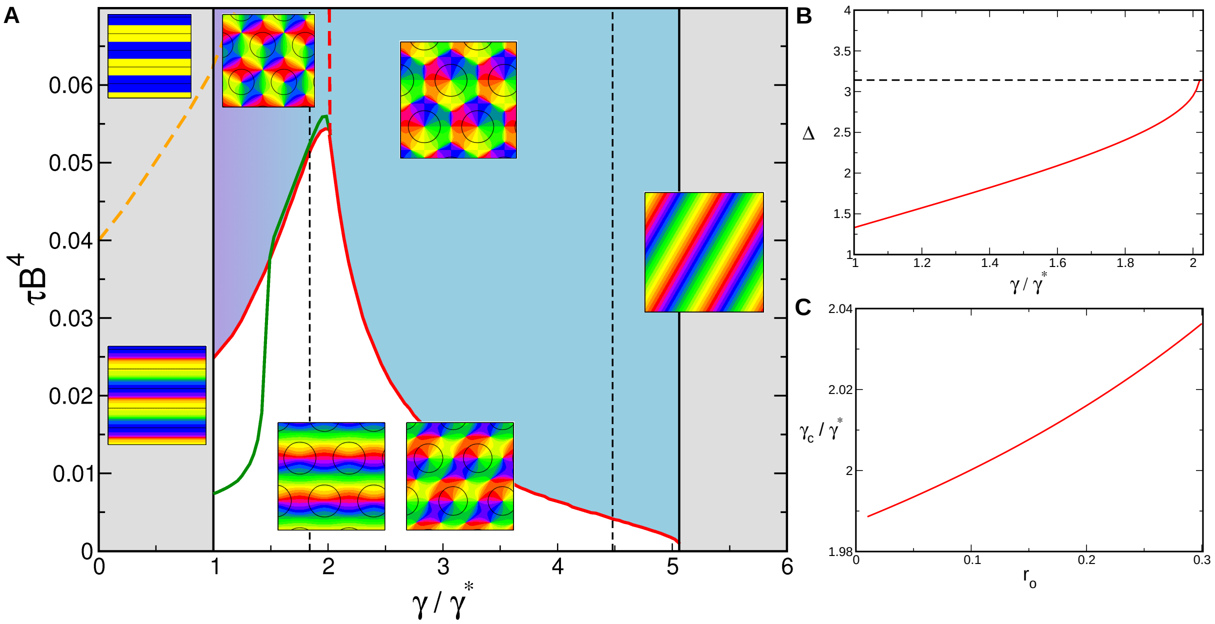

Figure 10. A Phase diagram with coupling energy $\mathbf{U} = \tau \mathbf{o}^4 |\mathbf{z}|^4$, $r_o = 0.2, r_z \ll r_o$. Vertical black lines: stability range of OD stripes, hexagons, and constant solutions. Orange dashed line: Stability border of orientation scotoma stripes. Green solid line: Stability border of rhombic solutions. Red solid line: Stability border of PWC solutions, red dashed line: γ_c, **B** Course of Eq. (80), dashed line: $\Delta = \pi$. **C** Stability border between Eq. (80) solution and the $\Delta = \pi$ solution as a function of r_o (vertical red line in **A**).

Phase diagram

The stability properties of all stationary solutions are summarized in the phase diagram Fig. 10. Compared to the gradient-type interaction energy we cannot scale out the dependence on r_o. The phase diagram is thus plotted for $r_o = 0.2$. We rescale the inter-map coupling strength as $\tau \mathcal{B}^4$ where $\mathcal{B}$ is the stationary amplitude of the OD hexagons. In the regime of stable OD stripes there is a transition from OP stripes towards the orientation scotoma stripe solution. In the regime of stable OD hexagons there is a transition from OP stripes towards PWC solutions (red line). The stability border of PWC solutions is strongly OD bias dependent and has a peak at $\gamma \approx 2\gamma^*$. For small OD bias γ the uniform solution Eq. (80) is stable. With increasing bias there is a smooth transition of this solution until at $\gamma = \gamma_c$ the $d = \pi$ uniform solution becomes stable. In Fig. 10**C** the stability border γ_c between the two types of uniform solutions is plotted as a function of r_o. We observe that there is only a weak dependence on the control parameter and $\gamma_c \approx 2\gamma^*$.

Interaction induced pinwheel crystals

Figure 11 illustrates the uniform solutions Eq. (80) for different values of the OD bias γ. For small bias, the OP pattern has six pinwheels per unit cell. Two of them are located at OD maxima while one is located at an OD minimum. The remaining three pinwheels are located near the OD border. With increasing bias, these three pinwheels are pushed further away from the OD border, being attracted to the OD maxima. With further increasing bias three shifted pinwheels merge with the one at the OD maximum building a single charge 1 pinwheel centered on a contralateral peak. The remaining two

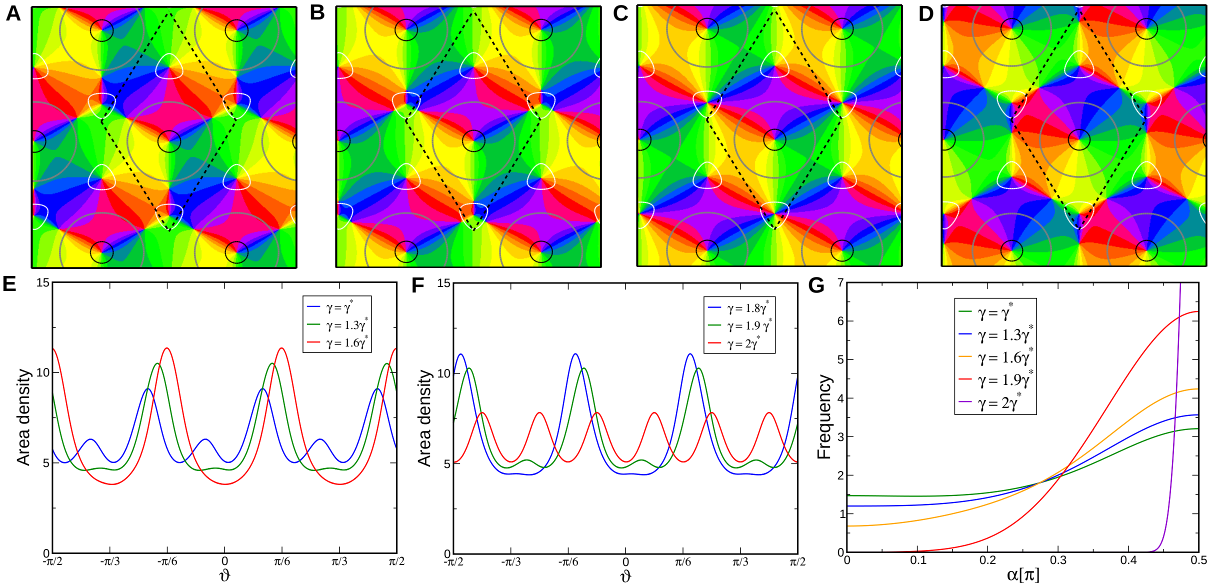

Figure 11. Bias dependent pinwheel crystals, Eq. (80) **A** $\gamma = \gamma^*$, **B** $\gamma = 1.3\,\gamma^*$, **C** $\gamma = 1.6\,\gamma^*$, **D** $\gamma = 2\,\gamma^*$. OP map, superimposed are the OD borders (gray), 90% ipsilateral eye dominance (black), and 90% contralateral eye dominance (white), $r_o = 0.2$. Dashed lines mark the unit cell of the regular pattern. **E,F** Distribution of orientation preference. **G** Intersection angles between iso-orientation lines and OD borders.

pinwheels are located at an ispi and contra peak, respectively. Note, compared to the Braitenberg PWC of the $\Delta = 0$ uniform solution the charge 1 pinwheel here is located at the contralateral OD peak. Finally, the charge 1 pinwheels split up again into four pinwheels. With increasing bias the solution more and more resembles the Ipsi-center PWC ($\Delta = \pi$ solution) which is stable also in the lower order version of the coupling energy. Finally, at $\gamma/\gamma^* \approx 2$ the Ipsi-center PWC becomes stable and fixed for $\gamma > 2\gamma^*$. The distribution of preferred orientations for different values of the bias γ is shown in Fig. 11**E,F**, reflecting the symmetry of each pattern. The distribution of intersection angles is shown in Fig. 11**G**. Remarkably, all solutions show a tendency towards perpendicular intersection angles. This tendency is more pronounced with increasing OD bias. At about $\gamma/\gamma^* \approx 1.9$ parallel intersection angles are completely absent and at $\gamma/\gamma^* \approx 2$ there are exclusively perpendicular intersection angles.

Gradient-type energy $U = \epsilon\,|\nabla o \nabla z|^4$

Finally, we examine the higher order version of the gradient-type inter-map coupling. The interaction terms are independent of the OD shift δ. In this case the coupling strength can be rescaled as $\beta\mathcal{B}^4$ and is therefore independent of the bias γ. The bias in this case only determines the stability of OD stripes, hexagons or the constant solution.

Stationary solutions and their stability

As for its lower order pendant a coupling to OD stripes is relatively easy to analyze. The energetic ground state corresponds to OP stripes with the direction perpendicular to the OD stripes for which $U = 0$. In addition, there are rhombic solutions with the stationary amplitudes $\mathcal{A}_1 = \mathcal{A}_{1^-} = \mathcal{A}_2 = \mathcal{A}_{2^-} = \sqrt{r_z/(5 + 80\epsilon\mathcal{B}^4)}$. In case the OD map is a constant, Eq. (117), the gradient-type inter-map coupling

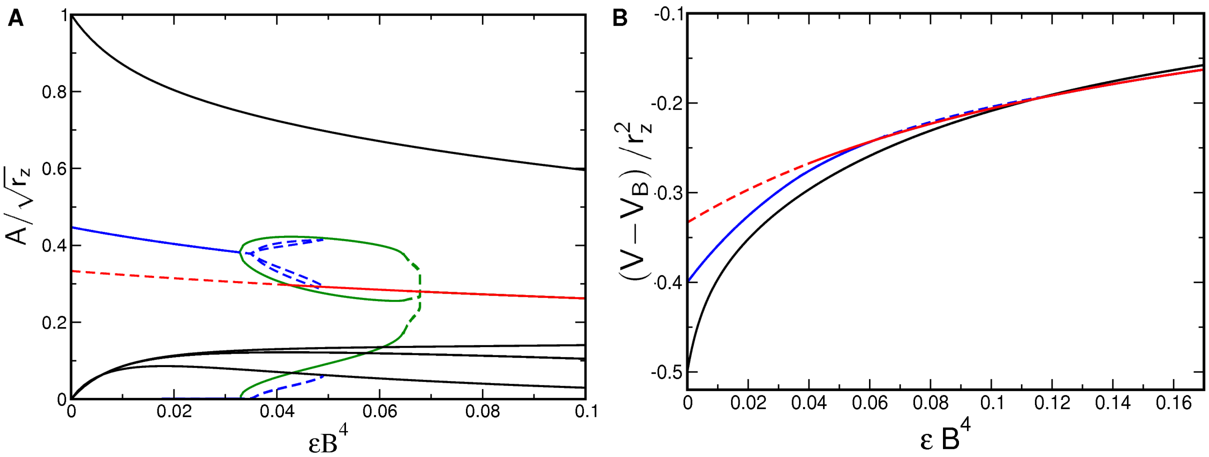

Figure 12. Stationary amplitudes with coupling energy $\mathbf{U} = \epsilon\, |\nabla \mathbf{z} \nabla \mathbf{o}|^4$, A Solid (dashed) lines: Stable (unstable) solutions of Eq. (71). Blue: rPWC, green: distorted rPWC, red: hPWC. Black lines: stripe-like solutions. **B** Potential, Eq. (70), of OP stripes (black), OP rhombs (blue), and hPWC solutions (red).

leaves the OP unaffected. As for its lower order pendant the stationary states are therefore OP stripes running in an arbitrary direction and the uncoupled rhombic solutions.

In case of OD hexagons, Eq. (116), we identified three types of non-uniform solutions. Besides stripe-like solutions of $z(\mathbf{x})$ with one dominant mode we find rPWCs $\mathcal{A}_j = \mathcal{A}_{j^-} = (\mathcal{A}, a, \mathcal{A})$ with $a \ll \mathcal{A}$ and distorted rPWCs $\mathcal{A}_j = (\mathcal{A}_1, \mathcal{A}_2, \mathcal{A}_3)\,, \mathcal{A}_{j^-} = (\mathcal{A}_3, \mathcal{A}_2, \mathcal{A}_1)$ with $\mathcal{A}_1 \neq \mathcal{A}_2 \neq \mathcal{A}_3$. Note, that distorted rPWCs are not stable in case of the product-type coupling energy or the analyzed low-order coupling energies. For these non-uniform solutions the stationary phases are inter-map coupling strength dependent. We therefore calculate the stationary phases and amplitudes numerically using a Newton method and initial conditions close to these solutions.

In case of OD hexagons there are further uniform solutions $A_j = A_{j^-} = \mathcal{A}, B_j = \mathcal{B}$ and $\psi_1 = \psi_3 = 0, \psi_2 = \pi$. The imaginary part of Eq. (71) leads to equations for the phases ϕ_j. The ansatz Eq. (60) leads to the stationarity condition

$$(13\cos\Delta - 5)\sin\Delta = 0\,. \tag{82}$$

The solutions are $\Delta = 0, \Delta = \pi$, and $\Delta = \pm\arccos\left(\frac{5}{13}\right) \approx \pm 1.176$ where the stationary amplitude are given by

$$\mathcal{A} = \sqrt{r_z/\left(9 + \epsilon\mathcal{B}^4\left(61.875 - 7.5\cos\Delta + 4.875\cos(2\Delta)\right)\right)}\,. \tag{83}$$

We calculated the stability properties of all stationary solutions by linear stability analysis considering perturbations of the amplitudes $\mathcal{A}_j \to \mathcal{A} + a_j$, $\mathcal{A}_{j^-} \to \mathcal{A} + a_{j^-}$ and of the phases $\phi_j \to \phi_j + \varphi_j$, $\phi_{j^-} \to \phi_{j^-} + \varphi_{j^-}$. This leads to a perturbation matrix M. In general amplitude and phase perturbations do not decouple. We therefore calculate the eigenvalues of the perturbation M matrix numerically. It turns out that for this type of coupling energy only the uniform solutions with $\Delta = \pm\arccos\left(\frac{5}{13}\right)$ are stable while the $\Delta = 0$ and $\Delta = \pi$ solutions are unstable in general.

Bifurcation diagram

For increasing inter-map coupling strength the amplitudes of the OP stripe and OP rhombic solutions are shown in Fig. 12**A**. In case of stable OD hexagons there is a transition from rPWC (blue) towards distorted rPWC (green). The distorted rPWCs then decay into the hPWC (red). In case of OP stripes (black dashed lines) inter-map coupling leads to a slight suppression of the dominant mode and a growth of the remaining modes. This growth saturates at small amplitudes and thus the solution stays stripe-like. This stripe-like solution remains stable for arbitrary large inter-map coupling. Therefore there is a bistability between hPWC solutions and stripe-like solutions for large inter-map coupling.

The stability borders for the rPWC and distorted rPWC solutions were obtained by calculating their bifurcation diagram numerically from the amplitude equations Eq. (71). With increasing map coupling we observe a transition from a rPWC towards a distorted rPWC at $\epsilon\mathcal{B}^4 \approx 0.033$ (blue dashed line in Fig. 13**A**), see also Fig. 16**A**. The distorted rPWC loses its stability at $\epsilon\mathcal{B}^4 \approx 0.065$ (blue solid line in Fig. 13**A**) and from thereon all amplitudes are equal corresponding to the hPWC. There is a bistability between hPWC, rPWC, and stripe-like solutions. To calculate the inter-map coupling needed for the hexagonal solution to become the energetic ground state we calculated the potential Eq. (70) for the three solutions. In case of the uniform solution Eq. (60) the potential is given by

$$\begin{aligned} V &= -6\mathcal{A}^2 r_z - 3\mathcal{B}^2 r_o + 27\mathcal{A}^4 + \frac{45}{2}\mathcal{B}^4 \\ &\quad + \frac{1}{16}\mathcal{A}^4\mathcal{B}^4\epsilon\left(3210 - 456\cos\Delta + 90\cos(2\Delta)\right) . \end{aligned} \tag{84}$$

The potential in case of the rhombic and stripe-like solutions was obtained by numerically solving the amplitude equations using Newtons method and initial conditions close to these solutions. Above $\epsilon\mathcal{B}^4 \approx 0.12$ the hPWC is energetically preferred compared to stripe-like solutions (red dashed line in in Fig. 13) and thus corresponds to the energetic ground state for large inter-map coupling, see Fig. (12)**B**.

Phase diagram

We calculated the phase diagram of the coupled system in the limit $r_z \ll r_o$, shown in Fig. 13. The phase diagram contains the stability borders of the uncoupled OD solutions $\gamma^*, \gamma_2^*, \gamma_3^*, \gamma_4^*$. They correspond to vertical lines, as they are independent of the inter-map coupling in the limit $r_z \ll r_o$. At $\gamma = \gamma^*$ hexagons become stable. Stripe solutions become unstable at $\gamma = \gamma_2^*$. At $\gamma = \gamma_3^*$ the homogeneous solution becomes stable while at $\gamma = \gamma_4^*$ hexagons loose their stability. In units γ/γ^* the borders $\gamma_2^*, \gamma_3^*, \gamma_4^*$ vary slightly with r_o , see Fig. 26, and are drawn here for $r_o = 0.2$. We rescale the inter-map coupling strength as $\epsilon\mathcal{B}^4$ where $\mathcal{B}$ is the stationary amplitude of the OD hexagons. The stability borders of OP solutions are then horizontal lines. For $\gamma < \gamma^*$ or for $\gamma > \gamma_4^*$ pinwheel free orientation stripes are dynamically selected. For $\gamma^* < \gamma < \gamma_4^*$ and above a critical effective coupling strength $\epsilon\mathcal{B}^4 \approx 0.042$ hPWC solutions are stable and become the energetic ground state of Eq. (70) above $\epsilon\mathcal{B}^4 \approx 0.117$. Below $\epsilon\mathcal{B}^4 \approx 0.065$, rPWC solutions are stable leading to a bistability region between rPWC and hPWC solutions. We find in this region that rhombic solutions transform into distorted rhombic solutions above an effective coupling strength of $\epsilon\mathcal{B}^4 \approx 0.033$.

Interaction induced pinwheel crystals

First, we studied the spatial layout of the rhombic solutions which is illustrated in Fig. 14. The rPWC solutions are symmetric under rotation by 180 degree. The rhombic solution has 4 pinwheels per unit cell and its pinwheel density is thus $\rho = 4\,\cos(\pi/6) \approx 3.5$. One may expect that the energy term Eq. (23) favors pinwheels to co-localize with OD extrema. In case of the rhombic layout there is only one pinwheel at an OD extremum while the other three pinwheels are located at OD saddle-points which are also energetically favorable positions with respect to U. The orientation selectivity $|z(\mathbf{x})|$ for the rPWC is shown in Fig. 14**B**. The pattern of selectivity is arranged in small patches of highly selective regions.

The hexagonal layout of the two stable uniform solutions is shown in Fig. 15. The $\Delta = \pm\arccos(5/13)$ solutions have six pinwheels per unit cell. Their pinwheel density is therefore $\rho = 6\cos\pi/6 \approx 5.2$. Three pinwheels of the same topological charge are located at the extrema of the OD map. Two of these are

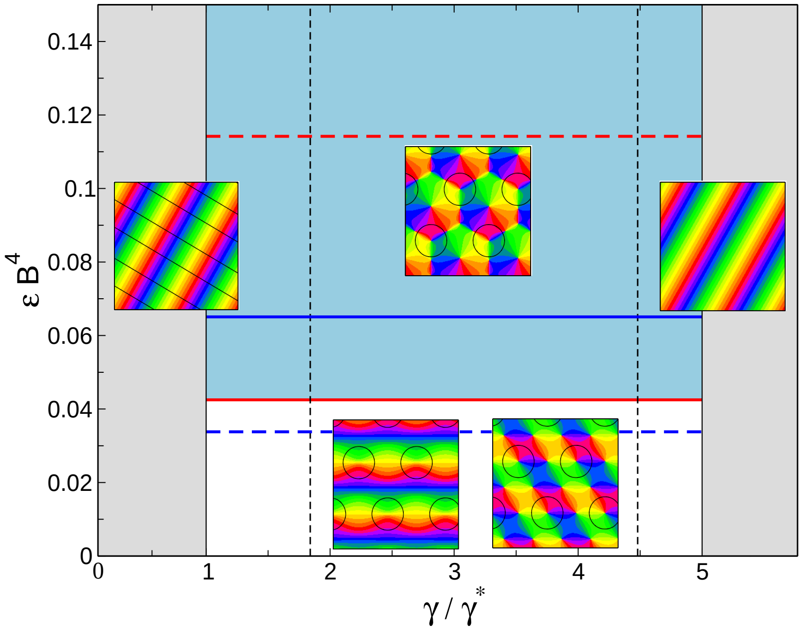

Figure 13. Phase diagram with coupling energy $\mathbf{U} = \epsilon\,|\nabla \mathbf{z} \nabla \mathbf{o}|^{\mathbf{4}}$, for $r_z \ll r_o$. Vertical lines: stability range of OD hexagons, red solid line: stability border of hPWC, blue solid line: stability border of rPWC, blue dashed line: transition from rPWC to distorted rPWC. Dashed red line: hPWC corresponds to ground state of energy.

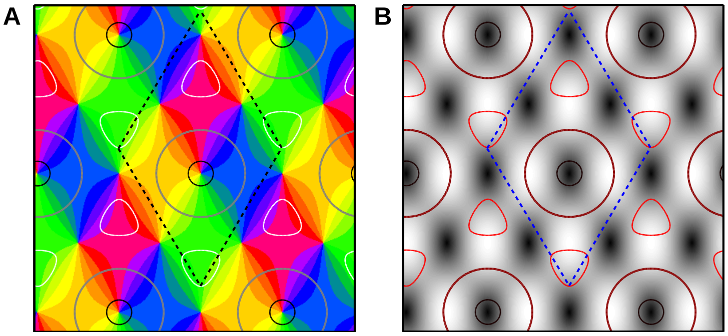

Figure 14. Rhombic pinwheel crystals. **A** OP map with superimposed OD borders (gray), 90% ipsilateral eye dominance (black), and 90% contralateral eye dominance (white), $\gamma = 3\gamma^*, r_o = 0.2$. **B** Selectivity $|z(\mathbf{x})|$, white: high selectivity, black: low selectivity.

located at the OD maximum while one is located at the OD minimum. The remaining three pinwheels are not at an OD extremum but near the OD border. The distance to the OD border depends on the OD bias, see Fig. 15**D**. For a small bias ($\gamma \approx \gamma^*$) these three pinwheels are close to the OD borders and with increasing bias the OD border moves away from the pinwheels. The pinwheel in the center of the OP hexagon is at the contralateral OD peak. Because these pinwheels organize most of the map while the others essentially only match one OP hexagon to its neighbors we refer to this pinwheel crystal as the *Contra-center pinwheel crystal*. Note, that some pinwheels are located at the vertices of the hexagonal pattern. Pinwheels located between these vertices (on the edge) are not in the middle of this edge. Solutions with $\Delta = \pm\arccos(5/13)$ are therefore not symmetric under a rotation by 60 degree but symmetric under a rotation by 120 degree. Therefore the solution $\Delta = +\arccos(5/13)$ cannot be transformed into the solution $\Delta = -\arccos(5/13)$ by a rotation of the OD and OP pattern by 180 degrees. This symmetry is also reflected by the distribution of preferred orientations, see Fig. 15**F**. Six orientations are slightly overrepresented. Compared to the Ipsi-center PWC, which have a 60° symmetry, this distribution illustrates the 120° symmetry of the pattern. The distribution of intersection angles is continuous, see Fig. 15**C**. Although there is a fixed uniform solution with varying OD bias the distribution of intersection angles changes. The reason for this is the bias dependent change in the OD borders, see Fig. 15**D**. For all bias values there is a tendency towards perpendicular intersection angles, although for low OD bias there is an additional small peak at parallel intersection angles. The orientation selectivity $|z(\mathbf{x})|$ for the hPWC is shown in Fig. 15**E**. The pattern shows hexagonal bands of high selectivity.

Finally, we study changes in pinwheel positions during the transition from a rPWC towards a hPWC i.e. with increasing inter-map coupling strength. In case of the higher order gradient-type coupling energy there is a transition towards a contra-center PWC, see Fig. 16**A**. In the regime where the distorted rPWC is stable, three of the four pinwheels of the rPWC are moving either from an OD saddle-point to a position near an OD border (pinwheel 1 and 3) or from an OD saddle-point to an OD extremum (pinwheel 4). One pinwheel (pinwheel 2) is fixed in space. At the transition to the hPWC two additional pinwheels are created, one near an OD border (pinwheel 5) and one at an OD extremum (pinwheel 6). We compare the inter-map coupling strength dependent pinwheel positions of the gradient-type coupling energy with those of the product type coupling energy, see Fig. (16)**B**. In this case three (pinwheel 2,3,4) of the four rPWC pinwheels have a inter-map coupling strength independent position. The remaining pinwheel (pinwheel 1) with increasing inter-map coupling strength splits up into three pinwheels. While one of these three pinwheels (pinwheel 1) is fixed in space the remaining two pinwheels (pinwheel 5,6) move towards the extrema of OD. Thus for large inter-map coupling, where hPWC solutions are stable, all six pinwheels are located at OD extrema.

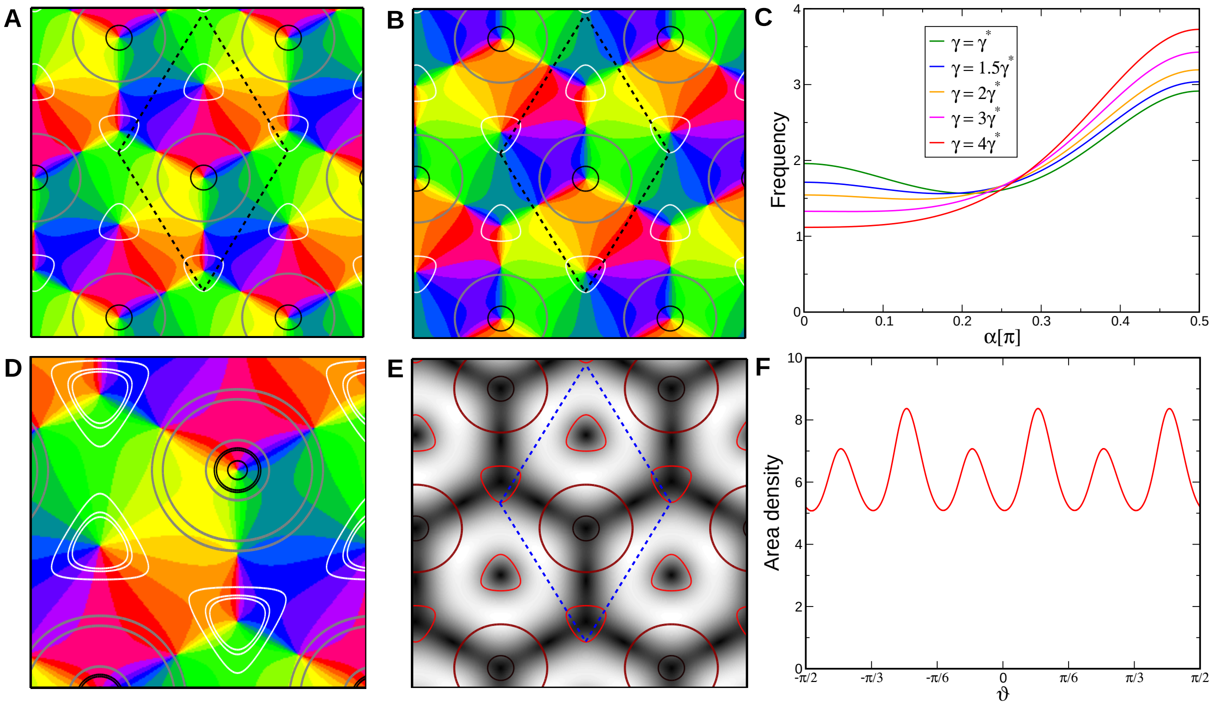

Figure 15. Contra-center pinwheel crystals. **A,B** OP map, superimposed are the OD borders (gray), 90% ipsilateral eye dominance (black), and 90% contralateral eye dominance (white), $r_o = 0.2, \gamma = 3\gamma^*$. **A** $\Delta = \arccos(5/13)$, **B** $\Delta = -\arccos(5/13)$. **C** Distribution of orientation preference. **D** OP map with superimposed OD map for three different values $(\gamma = \gamma^*, \gamma = (\gamma_4^* - \gamma^*)/2 + \gamma^*, \gamma = \gamma_4^*)$ of the OD bias. **E** Selectivity $|z(\mathbf{x})|$, white: high selectivity, black: low selectivity. **F** Distribution of intersection angles.

Synopsis of analytical results

We have examined the impact of four different interaction energies on the structure of local minima and ground states of models for the coordinated optimization of a complex and a real scalar feature map such as OP and OD maps. The models were constructed such that in the absence of interactions, the maps reorganized into simple stripe or blob pattern. In particular, the complex scalar map without interactions would form a periodic stripe pattern without any phase singularity. In all four models, increasing the strength of interactions could eventually stabilize qualitatively different more complex and biologically more realistic patterns containing pinwheels that can become the energetic ground states for strong enough inter-map interactions. The way in which this happens provides fundamental insights into the relationships between map structure and energy functionals in optimization models for visual cortical functional architecture.

Our results demonstrate that the structure of maps shaped by inter-map interactions is in principle informative about the type of coupling energy. Pinwheel positions in rPWCs tracked while increasing inter-map coupling strength were different for different coupling terms examined and thus can in principle serve as a trace of the underlying optimization principle. Furthermore, the organization of the complex scalar map that optimizes the joined energy functional was in general different for all four types of coupling terms examined. This organization, however, was often not inferable by simple qualitative considerations on the energy functional. For instance, the higher order gradient-type interaction term

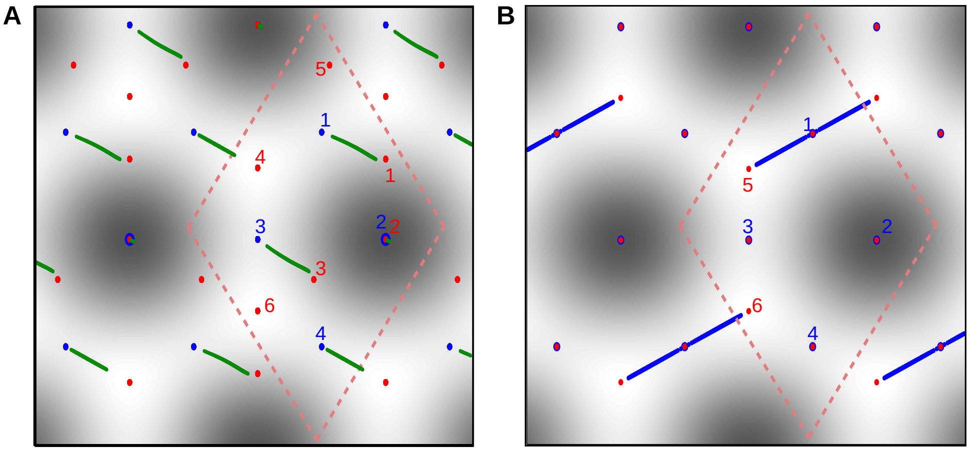

Figure 16. Inter-map coupling strength dependent pinwheel positions. OD map, superimposed pinwheel positions (points) for different inter-map coupling strengths, $\gamma/\gamma^* = 3$. Numbers label pinwheels within the unit cell (dashed lines). Blue (green, red) points: pinwheel positions for rPWC (distorted rPWC, hPWC) solutions. **A** $\mathbf{U} = \epsilon\, |\nabla \mathbf{z} \nabla \mathbf{o}|^{\mathbf{4}}$, using stationary amplitudes from Fig. (12)(a). Positions of distorted rPWCs move continuously (pinwheel 1,3,4). **B** $\mathbf{U} = \tau\, |\mathbf{z}|^{\mathbf{4}} \mathbf{o}^{\mathbf{4}}$, using stationary amplitudes from Fig. (9)**D**. Positions of rPWCs move continuously (pinwheel 5,6).

positioned half of the pinwheels close to OD borders although examination of the interaction term per se suggests that OD extrema should be energetically preferred. Also, in all models, intersection angles of iso-orientation lines and OD borders have a tendency towards perpendicular angles whether the energy term mathematically depends on this angle, as for the gradient-type energies, or not, as for the product-type energies. Intersection angle statistics thus are not a very sensitive indicator of the type of interaction optimized. Mathematically, these phenomena result from the complex interplay between the single map energies and the interaction energies.

The information provided by the map structure appears rather qualitative than quantitative. In three of the four models, hPWC patterns resulting from strong interactions were fixed, not exhibiting any substantial dependence on the precise choice of interaction coefficient. In principle, the spatial organization of stimulus preferences in a map is an infinite dimensional object that could depend and be sensitively in distinct ways on a large number of model parameters. It is thus important to note that this structure often essentially gives no information about the value of coupling constant in our simple models. The situation is reversed when considering the structure of rPWCs. These solutions exist and are stable although energetically not favored in the absence of inter-map interactions. Some of their pinwheel positions continuously depend on the strength of inter-map interactions. These solutions and their parameter dependence however are largely uninformative about the nature of the interaction energy. This reflects that the rPWC state essentially is an uncoupled system solution that is only modified by the inter-map interaction. In summary, although distinct types of coupling energies can leave distinguishing signature on the structure of maps shaped by interaction (as the OP map in our example), drawing precise conclusions about the coordinated optimization principle from observed map structures is not possible for the analyzed models.

Part III: Dynamics and higher feature dimensions

So far, we presented an analytical treatment of the coordinated optimization of interacting pairs of maps. Our results demonstrate that various types of inter-map coupling energies can induce the formation of pinwheel-like singularities in the complex scalar map. In the solutions that are energetically favored by the interaction energy and can become global ground states of the model, singularities are arranged on regular periodic lattices (rPWCs, hPWCs). However, our perturbative treatment gives no information on the speed with which singularities that were initially generated during spontaneous symmetry breaking will crystallize into such highly ordered arrays. In principle, this process may occur on very long timescales. If this was the case, developmental optimization may lead to long-lived spatially irregular states that are transients towards regular patterns that would be reached after very long times or potentially never if the relevant time scale would be bigger than the critical period. In addition, we showed that for higher order inter-map coupling energies we could neglect the backreaction onto the OD map for a sufficiently small ratio r_z/r_o. Also this finding raises questions that cannot be addressed purely perturbatively. Do the observed local minima and ground states of the analyzed optimization principles persist when taking the backreaction into account or when considering map formation far from the pattern forming threshold? Besides the influence of the backreaction the full dynamical system receives additional corrections. There are higher order corrections to the uncoupled amplitude equations which can become important for finite bifurcation parameters r_z, r_o but which we neglected above. Finally, it seems appropriate to assess whether our main results might qualitatively depend on the relatively low number of feature maps considered. While our analysis so far was confined to two interacting maps such as OP and OD the visual cortex contains additional mapped representations. Theoretically, multiple interacting maps with conflicting design requirements may more easily lead to spatially aperiodic layouts that would be biologically more realistic than the regular pattern we found in the models considered so far. To assess these issues we solved the full field dynamics Eq. (10) numerically. The numerical integration scheme is detailed in the Methods part. Initial conditions for the OD map are stripe, hexagonal, or constant patterns plus white noise. Initial conditions for the OP map are either pinwheel-free OP stripes or band-pass filtered Gaussian random noise for which the average pinwheel density equals the mathematical constant π. For this numerical analysis we focus on the high order gradient-type inter-map coupling energy that can reproduce all qualitative relationships found between OP and OD maps, does not suffer from potential OP map suppression, and has a relatively simple phase diagram.

Kinetics of pinwheel crystallization

To characterize the process of pinwheel annihilation, preservation, and creation during progressive map optimization we calculated the pinwheel density as well as various other pinwheel statistics, see Methods, during the convergence of patterns to attractor states. The time evolution of the pinwheel density is shown in Fig. 17. In the uncoupled case ($\epsilon = 0$) most of the patterns decayed into a stripe solution and their pinwheel density dropped to a value near zero. At small coupling strengths ($\epsilon = 200$) the pinwheel density converged either to zero (stripes), to values near 3.5 for the rPWC, or to approximately 5.2 for the contra-center PWC. At high map coupling ($\epsilon = 2000$) pinwheel free stripe patterns formed neither from pinwheel rich nor from pinwheel free initial conditions. In this regime the dominant layout was the contra-center PWC. When starting from OD and OP stripes, see Fig. 17**C** (green lines), the random orientation between the stripes first evolved towards a perpendicular orientation ($T \approx 1$). This lead to a transient increase in the pinwheel density. At the time ($T \approx 10$) where the OD stripes dissolve towards OD hexagons hPWC solutions formed and the pinwheel density reached its final value.

Regions of hPWC layout can however be inter-digitated with long lived rPWC solutions and stripe domains. Figure 17**D** shows the time course of the normalized power $P_n(t) = \langle |z(\mathbf{x},t)_{\mathrm{dyn}}|^2 \rangle_{\mathbf{x}} / \langle |z(\mathbf{x},t)_{\mathrm{th}}|^2 \rangle_{\mathbf{x}}$, where $\langle \rangle_{\mathbf{x}}$ denotes spatial average. The field z_{th} is obtained from solution of the amplitude equations Eq. (42) while z_{dyn} is the field obtained from the simulations. Starting from a small but nonzero power the amplitudes grew and saturated after $T \approx 1$. When the amplitudes were saturated the selection of the final pattern started. Quantitatively, we found that with backreaction the critical coupling strengths were slightly increased compared to their values in the limit $r_z \ll r_o$. Snapshots of the simulation leading to hPWC solutions at three time frames are shown in Fig. 18. At $T \approx 0.8$ a broad rearrangement of the

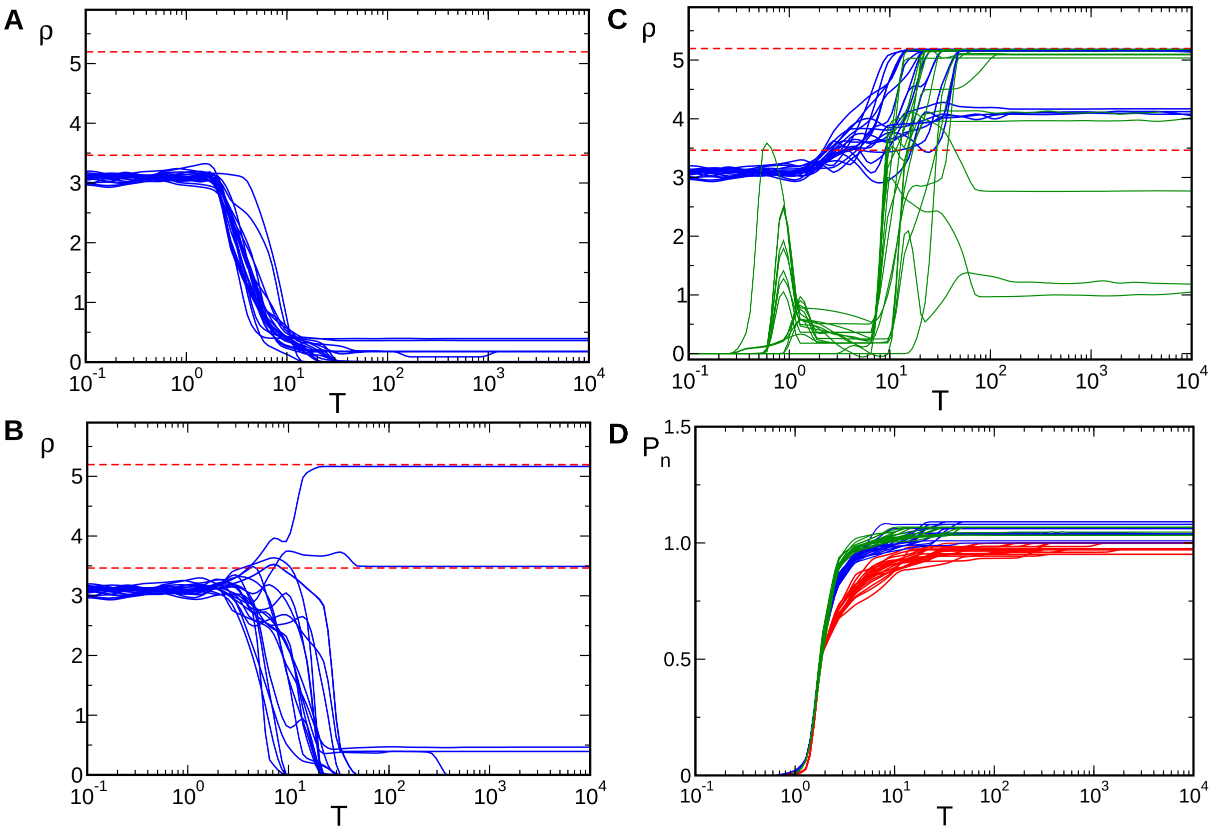

Figure 17. Time evolution of the pinwheel density, $U = \epsilon\, |\nabla z \nabla o|^4$, $r_z = 0.05, r_o = 0.25, \gamma = 0.15$. For each parameter set **A**-**C** simulations in blue started from an identical set of 20 initial conditions. Red dashed line: $\rho = 4\cos(\pi/6)$ and $\rho = 6\cos(\pi/6)$. **A** $\epsilon = 0$ **B** $\epsilon = 200$ **C** $\epsilon = 2000$. **D** Normalized power of OP map, $\epsilon = 0$ (red), $\epsilon = 200$ (blue), and $\epsilon = 2000$ (green). In green **C**: OD and OP stripes as initial conditions. Parameters: 128×128 mesh, $\Gamma = 22$.

pattern took place and we could identify different domains in the pattern.

During time evolution we further calculated the distributions of pinwheel next-neighbor distances d, measured in units of the column spacing Λ. The distributions of distances for simulations leading to rhombic and hPWC solutions are shown in Fig. 19. We could identify three stages in the evolution of the pinwheel distances. At early stages of the evolution ($T \approx 10^{-2}$) there was a continuous distribution starting approximately linearly from $d = 0$. At the time where the amplitudes saturated ($T \approx 1$) the distribution of pinwheels became very inhomogeneous. Different domains with stripe-like, rhombic, or hexagonal patterns appeared (see also Fig. 21**C,D**) until finally the rhombic or hexagonal pattern took over the whole area.

As pinwheels carry a topological charge we could divide the distributions according to distances between pinwheels of the same charge or according to distances between pinwheels of the opposite charge. In Fig. 20 we present pinwheel distances for the final states of the dynamics. In case of the rhombic solutions there is only a single pinwheel to pinwheel distance with $d = 1/\sqrt{3} \approx 0.58\,\Lambda$. In numerical simulations small variations in the amplitudes lead to a slightly larger distance between pinwheels of equal charge than between pinwheels of opposite charge. Therefore their distance distributions do not collapse exactly, see Fig. 20**A**. In case of the hPWC there are three peaks at $d \approx 0.28\,\Lambda, d \approx 0.36\,\Lambda$ and $d \approx 0.56\,\Lambda$

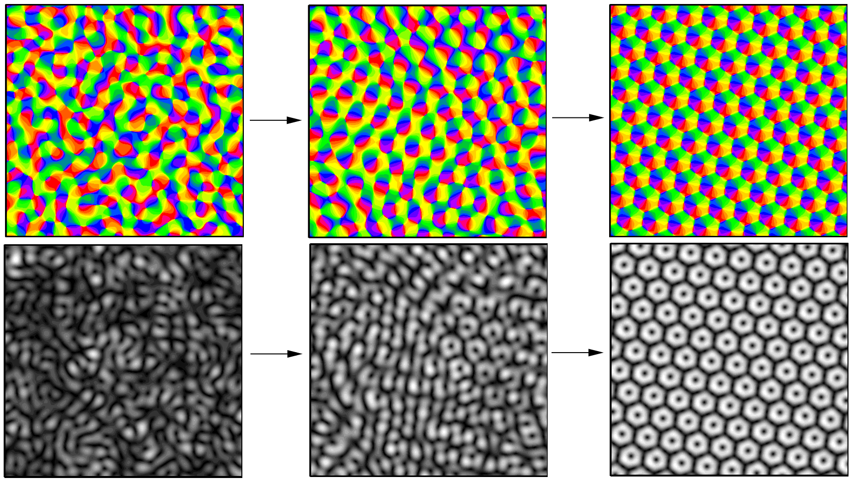

Figure 18. Snapshots of the pinwheel crystallization process. Top panel: OP map, bottom panel: selectivity $|z(\mathbf{x})|$. Left: $T = 0.01$, middle: $T = 0.8$, right: $T = T_f = 10^4$. Parameters as in Fig. 17(c).

in the pinwheel distance distribution of arbitrary charge, see Fig. 20**B**. These three peaks all result from distances between pinwheels carrying the opposite charge while the distance between pinwheels of the same charge shows two peaks at $d \approx 0.48\,\Lambda$ and $d \approx 0.64\,\Lambda$ in the distribution. The origin of the peaks is indicated in Fig. 20**C** and Fig. 20**D**.

We have shown that inter-map coupling leads to a stabilization of pinwheels in the OP pattern. This however does not mean that pinwheels initially generated by spontaneous symmetry breaking will be preserved during convergence of the map. To what extent are the pinwheels in the crystalline OP maps rearrangements of pinwheels of the initial OP pattern? To answer this question we calculated the pinwheel annihilation $a(t)$ and creation $c(t)$ rate during time evolution, see Methods. The time evolution of these rates, averaged over 20 simulations leading to a hPWC, is shown in Fig. 21**A**. We observe that both rates are fairly equal throughout the development, with a slightly higher creation rate in the later stage of development. During the initial stages of time evolution creation and annihilation rates decay algebraically. At $T \approx 3$ both rates deviate from this algebraic decay. From thereon annihilation and creation rates increase, reflecting a broad rearrangement of the pattern. After $T \approx 15$ no pinwheels are created or annihilated anymore and the pinwheels of the final pattern are present.

Pinwheels are created and annihilated until the crystal pattern is formed. How many pinwheels of the initial pattern are still present in the final pattern? For a given set of pinwheels at an initial time $T = T^*$ we further calculate the fraction $s(t)$ of those pinwheels surviving until time T. The fraction of pinwheels present at time T^* that survive up to the final time $T = T_f$ is given by $p(t)$. Both fractions are shown in Fig. 21**B** for $T^* = 0.01$ and in Fig. 21**C** for $T^* = 2$, a time where the power $P(t)$ has almost saturated, see Fig. 17**D**. We observed that about 20% of the initial pinwheels are preserved until the final time and therefore most of the pinwheels of the crystal pattern are created during development. From those pinwheels which are present when the power saturates about 65% are also present in the final pattern.

Detuning OD and OP wavelengths: OD stripes

The previous analytical as well as numerical results showed that OD stripes do not lead to spatially complex patterns and are not capable of stabilizing pinwheels. In case of gradient-type inter-map couplings the OP map consists of stripes which run perpendicular to the OD stripes, see Fig. 7 and Fig. 13**A**.

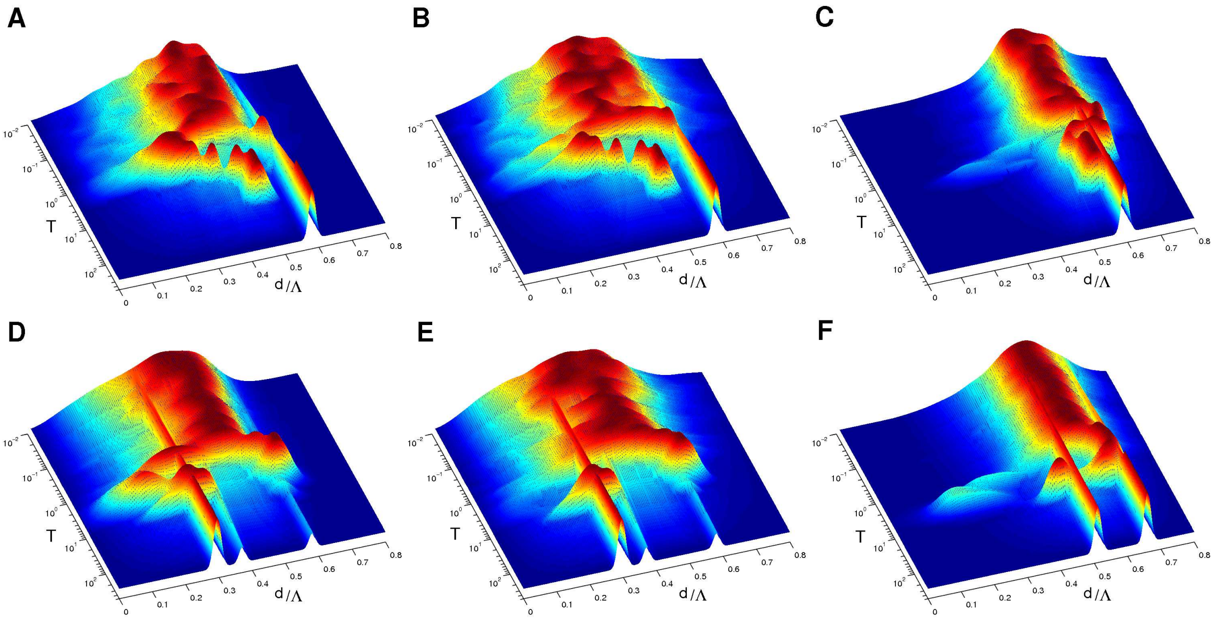

Figure 19. Distribution of nearest neighbor distances during development. **A**-**C** rPWC **D**-**F** hPWC. Distance to the next pinwheel of arbitrary **A,D**, opposite **B,E**, and equal **C,F** topological charge. Parameters as in Fig. 17**B**.

In case of the product-type inter-map coupling high gradient regions of both maps avoid each other by producing again OP stripes but now running in the same direction as the OD stripes, see Fig. 3**A** and Fig. 9**A**. In numerical simulations we also investigated the case of OD stripes of larger wavelength than OP columns, as is the case in macaque monkeys [20]. In case of a gradient-type inter-map coupling the OD bands are perpendicular to the OP bands independent of the ratio $\Lambda_o/\Lambda_z > 1$, see Fig. 22**A**-**C**. In case of the product-type inter-map coupling if the ratio $\Lambda_o/\Lambda_z > 1$ orientation representation does not collapse, as seen in Fig. 9**D**-**F**. The system, however, again finds a way to put a zero contour of z along the OD maximum which now is a fracture line, see Fig. 22. The angle between the active OP and OD modes is given by $\alpha = \arccos k_{c,o}/k_{c,z}$. This leads to the resonance relation $\vec{k}_{1,z} - \vec{k}_{2,z} - 2\vec{k}_{1,o} = 0$, see Fig. 22**A**. Interaction terms between OD and OP Fourier modes thus arise through amplitude equations of the form

$$\begin{aligned}\partial_t A_1 &= r_z A_1 - |A_1|^2 A_1 - 2|A_2|^2 A_1 - 6\tau |B|^4 \left(|A_1|^2 A_1 + 2|A_2|^2 A_1\right) \\ &\quad -4\tau B^3 \overline{B} \left(|A_2|^2 A_2 + 2|A_1|^2 A_2\right) - 4\tau \overline{B}^3 B A_1^2 \overline{A}_2 - \tau B^4 \overline{A}_1 A_2^2 \,, \end{aligned} \tag{85}$$

and a corresponding equation for the mode A_2.

Detuning OD and OP wavelengths: OD hexagons

In case of identical wavelengths $k_{c,o} = k_{c,z}$ strong interaction with OD hexagons leads to hPWC solutions. For these solutions pinwheel positions are correlated with OD extrema. For instance in case of the higher order gradient-type inter-map coupling energy, for which the contra-center PWC corresponds to the energetic ground state, half of the pinwheels are located at OD extrema. However, if the typical wavelengths of OD and OP patterns are detuned such a precise relationship cannot be fulfilled in general. We therefore studied whether a detuning of typical wavelengths can lead to spatially irregular and

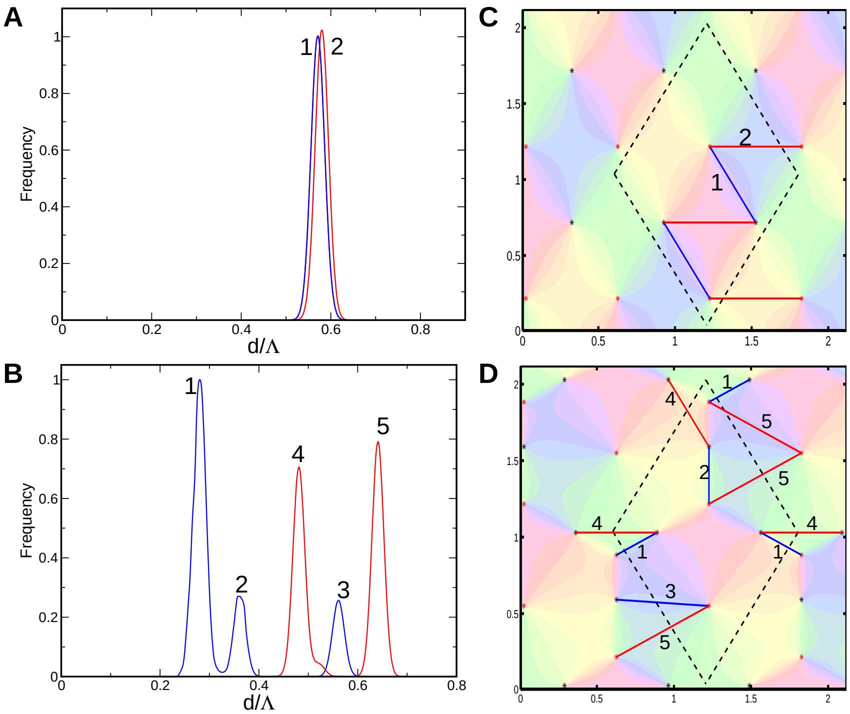

Figure 20. Distribution of nearest neighbor distances for final states ($T = T_f = 10^4$). **A** rPWC, **B** hPWC with pinwheels of equal (red) and opposite (blue) charge. **C** and **D** Illustration of occurring pinwheel distances. Pinwheels are marked with star symbols according to their charge. Units are given in Λ. Parameters as in Fig. 17**B**.

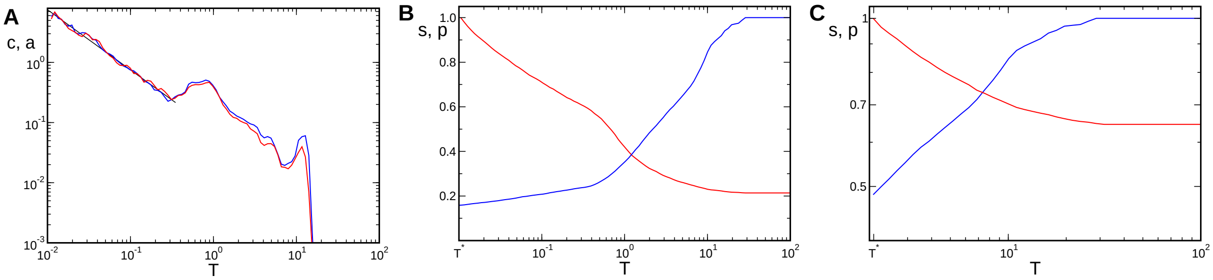

Figure 21. Pinwheel annihilation and creation. **A** Creation (blue) and annihilation (red) rates during time evolution. **B,C** Survival fraction (red) and fraction of preserved pinwheels (blue) compared to the initial time $T^* = 0.01$ **B** and $T^* = 2$ **C**. Parameters as in Fig. 17**C**.

pinwheel rich OP patterns. In numerical simulations which lead to OD hexagons with a fixed wavelength we varied the OP wavelength using identical initial conditions. Examples of final patterns of such simulations are shown in Fig. 23 using the high order gradient-type inter-map coupling energy. In all studied cases the final patterns are spatially regular. The observed patterns are either patterns with two active modes Fig. 23**A,C,D,E** or rPWC, see Fig. 23**B,F**. For a large ratio $k_{c,o}/k_{c,z}$ the patterns with two active modes are pinwheel free, see Fig. 23**A,C,D**. For smaller ratios $k_{c,o}/k_{c,z}$ the patterns are pinwheel rich, see Fig. 23**E**.

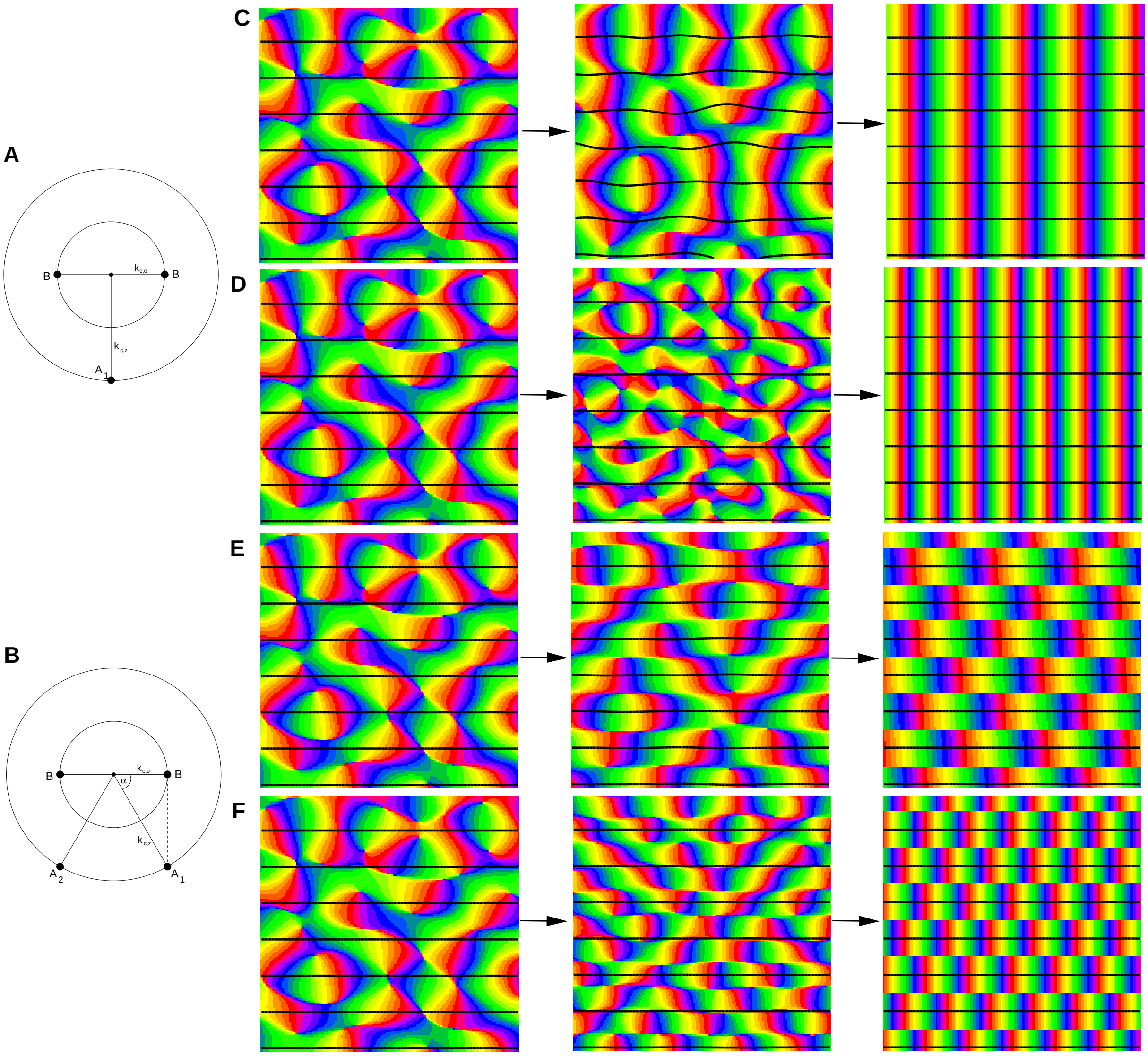

Figure 22. Map interactions with detuned wavelengths and OD stripes. OD stripes interacting with OP columns where $\Lambda_o/\Lambda_z > 1$. **A,B** Illustration of active modes in Fourier space with $k_{c,o} < k_{c,z}$, $\alpha = \arccos k_{c,o}/k_{c,z}$. **C,D** $U = \epsilon|\nabla z \nabla o|^4$, **E,F** $U = \tau o^4 |z|^4$. **C,E** $\Lambda_o/\Lambda_z = 1.3$, **D,F** $\Lambda_o/\Lambda_z = 2$. Left: initial condition, middle: $T = 1$, right: $T = 5 \cdot 10^4$. Parameters: $\tau = 2000, r_z = 0.05, r_o = 0.2, \Gamma_z = 20, 256 \times 256$ mesh. Initial condition identical in all simulations.

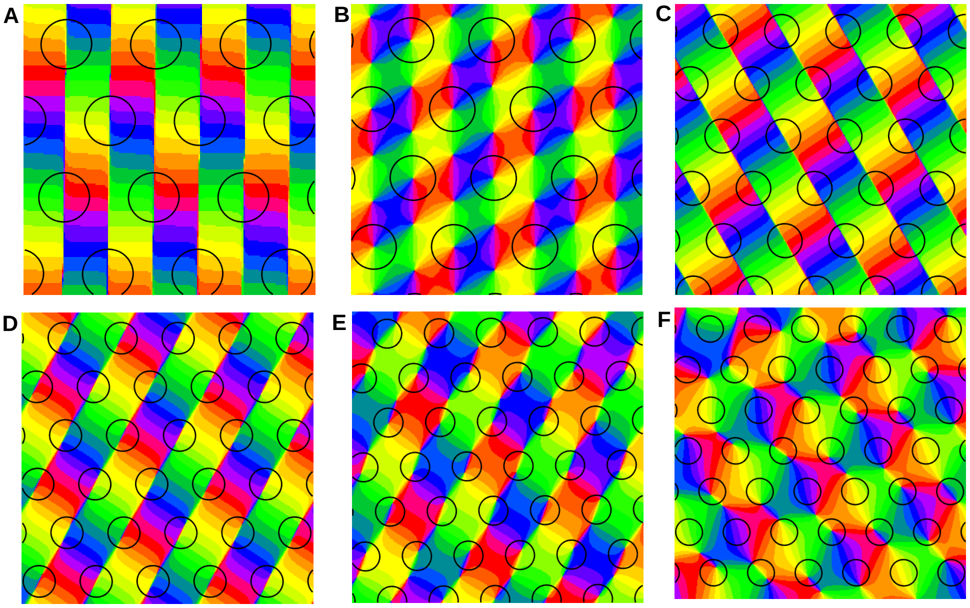

Figure 23. Map interactions with detuned wavelength and OD hexagons. $U = \epsilon\,|\nabla z \nabla o|^4$. **A** $\Lambda_o/\Lambda_z = 0.927$, **B** $\Lambda_o/\Lambda_z = 0.829$, **C** $\Lambda_o/\Lambda_z = 0.634$, **D** $\Lambda_o/\Lambda_z = 0.586$, **E** $\Lambda_o/\Lambda_z = 0.537$, **F** $\Lambda_o/\Lambda_z = 0.488$. Parameters: $\gamma = 0.15, r_z = 0.05, r_o = 0.2, \epsilon = 2000, \Gamma_o = 41, T_f = 10^4$, 256×256 mesh. Initial condition identical in all simulations.

Higher feature dimensions

The inclusion of more feature dimensions into the dynamics can be performed in a similar fashion as the geometric correlations between the maps seem to be universal [18]. To illustrate this we used the higher order gradient-type inter-map coupling with three and four cortical maps which are mutually coupled. Whereas in the case of two maps the coupling energy is zero if the two stripe solutions are perpendicular to each other the interactions between more maps potentially leads to a frustration as not all of the individual coupling energies can simultaneously vanish. Using the gradient coupling energy

$$U = U_1 + U_2 + U_3 = \epsilon_1 \left|\nabla z \nabla o_1\right|^4 + \epsilon_2 \left|\nabla z \nabla o_2\right|^4 + \epsilon_3 \left|\nabla o_1 \nabla o_2\right|^4 , \tag{86}$$

and no OD bias ($\gamma = 0$) we observed two types of stationary solutions, see Fig. 24. Here we used equal coupling strengths $\epsilon_1 = \epsilon_2 = \epsilon_3 = \epsilon$. In case all bifurcation parameters were equal the OP map consisted of stripes. Also the two real fields consisted of stripes, both perpendicular to the OP stripes i.e.

$$\begin{aligned} z(\mathbf{x}) &= A e^{\imath \vec{k}_1 \vec{x}} \\ o_1(\mathbf{x}) &= 2B_1 \cos(\vec{k}_2 \vec{x}) \\ o_2(\mathbf{x}) &= 2B_2 \cos(\vec{k}_2 \vec{x} + \psi) , \quad \vec{k}_1 \cdot \vec{k}_2 = 0 . \end{aligned} \tag{87}$$

The energy in this case is given by $U_1 = U_2 = 0$, $U_3 = \frac{B_1^4 B_2^4 \pi}{16} \left(18 + 16\cos(2\psi) + \cos(4\psi)\right)$ which is minimal for $\psi = \pi/2$, i.e. the energy is minimized by shifting one real field by half of the typical wavelength. When the bifurcation parameter of the OP map was smaller than that of the two real fields we obtained PWC patterns, see Fig. 24**B**. The pinwheels were arranged such that they are in the center of a square spanned by the two orthogonal real fields and the resulting pinwheel density is $\rho = 4$. All intersection angles between iso-orientation lines and borders of the real fields were perpendicular. When extending the system by another real field we observed a similar behavior. Figure 24**C,D** shows the stationary states of a complex field coupled to three real fields. In case of equal bifurcation parameters the stationary patterns were OP stripes, perpendicular to the stripe and meandering real solutions. In case the bifurcation parameter of the OP map was smaller than the other bifurcation parameters we again observed pinwheel crystallization. Note, that in this case all pinwheels were located at the border of one of the three real fields. To summarize, pinwheel crystallization was only observed if the OP is driven by the real field i.e. if the OP amplitudes are small. In all observed cases the patterns were spatially periodic.

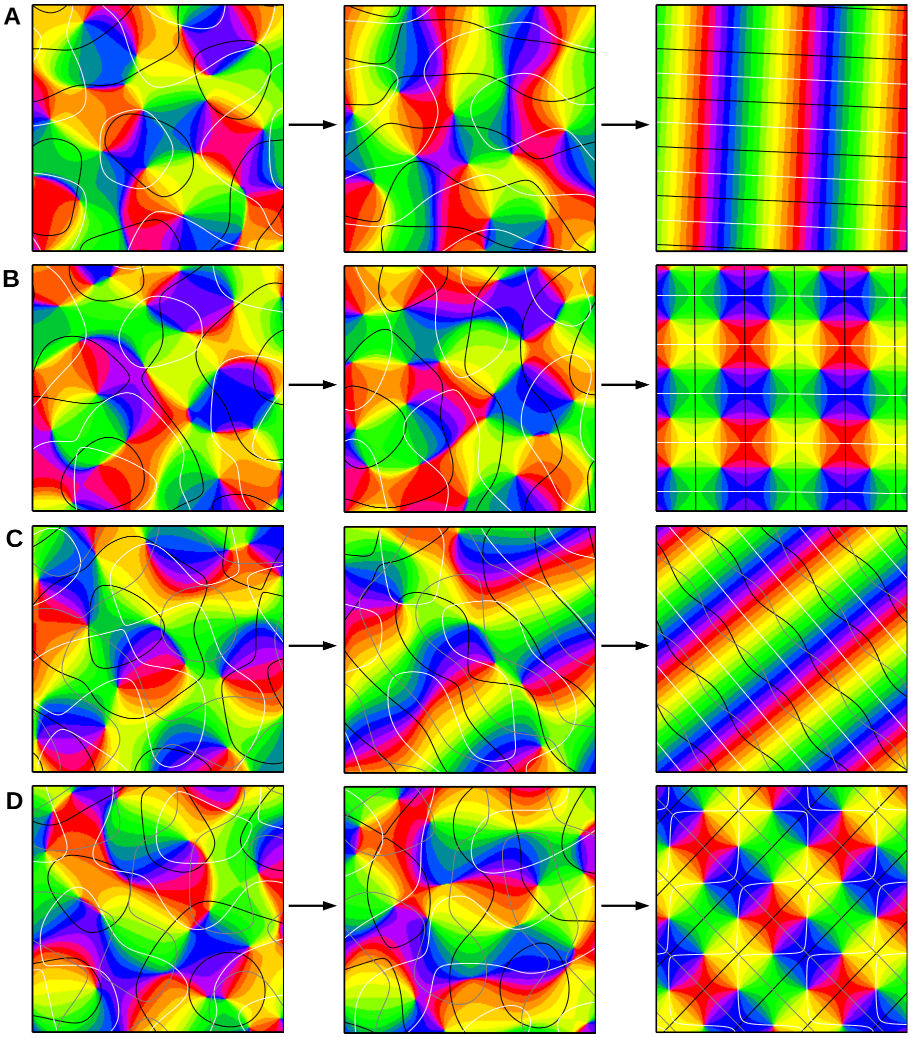

Figure 24. Map interactions in higher feature dimensions. **A,B** Map layout by interactions between three columnar systems $(z(\mathbf{x}), o_1(\mathbf{x}), o_2(\mathbf{x}))$. All maps are mutually coupled. Superimposed on the OP map there are the borders of two real fields (black, white). **A** $r_z = r_{o_1} = r_{o_2} = 0.1$ **B** $r_z = 0.01, r_{o_1} = r_{o_2} = 0.1$. **C,D** Interactions with four columnar systems $(z(\mathbf{x}), o_1(\mathbf{x}), o_2(\mathbf{x}, t), o_3(\mathbf{x}, t))$. **C** $r_z = r_{o_1} = r_{o_2} = r_{o_3} = 0.1$. **D** $r_z = 0.01, r_{o_1} = r_{o_2} = r_{o_3} = 0.1$. Superimposed on the OP map there are the borders the of three real fields (black, gray, white). Left panel: initial conditions, middle panel: $T = 10$, right panel: $T = T_f = 5 \cdot 10^4$. Parameters in all simulations: $\epsilon = 2000, \gamma = 0, \Gamma = 22$, 128×128 mesh.

Discussion

Summary of results

In this study we presented a symmetry-based analysis of the hypothesis that visual cortical architecture is shaped by the coordinated optimization of different functional maps. In particular, we focused on the question of how and whether different optimization principles impact on the spatial layout of functional maps in the primary visual cortex. Specifically, we identified different representative candidate optimization principles. We developed a dynamical systems approach for analyzing the simultaneous optimization of interacting maps and showed how their layout is influenced by coordinated optimization. In particular, we demonstrated that inter-map coupling can stabilize pinwheel-rich layouts even if pinwheels are intrinsically unstable in the uncoupled system. We calculated and analyzed the stability properties of solutions forming a spatially regular layout with pinwheels arranged in a crystalline array. We analyzed the structure of these pinwheel crystals in terms of their stability properties, spatial layout, and geometric inter-map relationships. For all models, we calculated phase diagrams showing the stability of the pinwheel crystals depending on the OD bias and the inter-map coupling strength. The main phenomena characterizing all considered models, crystallization induced by coordinated optimization and inter-map coupling, was found to be robust to a substantial degree of backreaction between the maps and persisted in models with higher feature space dimensionality.

Comparison to previous work

Our results rigorously establish that models of interacting OP and OD maps in principle offer a solution to the problem of pinwheel stability [31, 52]. This problem and other aspects of the influence of OD segregation on OP maps have previously been studied in a series of models such as elastic net models [12–15, 31, 33], self-organizing map models [8, 10, 11, 16, 17], spin-like Hamiltonian models [32, 61], spectral filter models [62], correlation based models [63], and evolving field models [64]. Several of these simulation studies found a higher number of pinwheels per hypercolumn if the OP map is influenced by strong OD segregation compared to the OP layout in isolation or the influence of weak OD segregation [31, 61, 64]. In such models, high gradients of OP and OD avoid each other [10, 16]. As a result, pinwheel centers tend to be located at centers of OD columns as seen in experiments [18, 19, 63, 65, 66]. By this mechanism, pinwheels are spatially trapped and pinwheel annihilation is reduced [31]. Moreover, many models appear capable of reproducing realistic geometric inter-map relationships such as perpendicular intersection angles between OD borders and iso-orientation lines [33, 62, 63]. Furthermore, Tanaka et al. have reported that the relative positioning of orientation pinwheels and OD columns was dependent on model details [63]. Informative as they were, one must note that almost all of these previous studies entirely relied on numerical approaches using methodologies that do not easily permit to assess the progress and convergence of solutions. Whether the reported solutions are attractors or just transient states and whether the solutions further develop towards pinwheel-free solutions or other states thus remained unclear. Moreover, in almost all previous models, a continuous variation of the inter-map coupling strength was not possible which makes it hard to disentangle the contribution of inter-map interactions from intrinsic mechanisms. Our results consistently show that coordinated optimization models exhibit a complex dynamics that persistently reorganizes maps over a broad range of timescales before attractors or optimized ground states are reached. Although our models exhibit various different attractor states none of them was able to directly converge to the final layout. Rather all of them were found to require substantial rearrangement of orientation columns after initial symmetry breaking. The only prior simulation study of a coordinated optimization model that tracked the number of pinwheels during the optimization process did not provide evidence that pinwheel annihilation could be stopped but only reported a reduction in annihilation speed [31]. In view of these findings, the prior evidence for coordination induced pinwheel stabilization appears rather limited. Our analytical calculations of attractor and ground states thus close a fundamental gap in the theory of visual cortical architecture and its development.

The mathematical structure of interaction models

To the best of our knowledge our study for the first time describes an analytical approach for examining the coordinated optimization of OP and OD maps. To achieve this we mapped the optimization problem to a dynamical systems problem which allows for a perturbative expansion of fixed points, metastable states, and ground states. Extending standard weakly nonlinear analysis to fifth order, we derived amplitude equations as an approximate description near the symmetry breaking threshold. We identified fixed points and study their stability properties using different types of inter-map coupling energies. For the low order version of these energies, a strong inter-map coupling often leads to OP map suppression, causing the orientation selectivity of all neurons to vanish. In contrast, the higher order variants of the coupling energies do not lead to map suppression but only influence pattern selection. In addition, high order coupling energies exhibit a limit in which the inter-map coupling becomes unidirectional enabling the use of the uncoupled OD patterns. We did not consider an interaction with the retinotopic map. Compared to other feature maps, the retinotopic map seems to be exceptional concerning its geometric relationships. It has been observed that the correlations between OP and retinotopic map are such that high gradient regions do not avoid each other [67]. Such correlations cannot be easily treated with dimension reduction models, see [68]. It is noteworthy that our phenomenological analysis identified coupling terms that could induce an attraction of high gradient regions. Such terms contain the gradient of only one field and can thus be considered as a mixture of the gradient and the product-type energy.

To confirm our results and to study the impact of a finite backreaction on the OD map we solved the full field dynamics numerically. In particular, we studied the dynamics of pinwheel crystallization. With the presented analytical approach we were able to show that pinwheel rich solutions correspond to the energetic ground state of the system for large inter-map coupling. This is reflected by the fact that in simulations, pinwheels can actually be created from an initial OP stripe pattern. Assessing pinwheel creation from pinwheel-free initial conditions can in general serve as a simple test of a pinwheel-rich energetic ground state in models of OP development. Taken together our results and approaches thus provide a formal basis and general methodology for the rigorous characterization of coordinated optimization models.

Modeling experimentally induced heterogeneities and areal borders

The presented map interaction model offers the possibility to study the impact of spatial inhomogeneities in the visual cortex on OP map structure. In such an application, the co-evolving field does not represent a feature map but would be designed to describe a real or artificial areal border or a disruption of local circuitry, which can be induced also experimentally [69]. To this end, the OP map is coupled to the field describing the areal border using low order coupling energies. At the areal border a strong inter-map coupling can lead to complete suppression of orientation selectivity. Using a gradient-type inter-map coupling energy inter-map coupling can furthermore lead to perpendicular crossings of iso-orientation lines with the areal borders as observed in experiments [70]. While in the past artificial heterogeneities and areal borders could only be induced by ablation of local surgical interventions, viral approaches now make it possible to impose them with minimal intervention and potentially in a reversible fashion.

Conditions for pinwheel stabilization

Our results indicate that a patchy layout of a second visual map interacting with the OP map is important for the effectiveness of pinwheel stabilization by inter-map coupling. Such a patchy layout can be easily induced by an asymmetry in the representation of a stimulus feature such as eye dominance or spatial frequency preference. In spatial frequency maps, for instance, low spatial frequency patches tend to form islands in a sea of high spatial frequency preference [18]. In our model, the patchy layout results from the overall dominance of one eye. In this case, OD domains form a system of hexagonal patches rather than stripes enabling the capture and stabilization of pinwheels by inter-map coupling. The results from all models question the view that OD stripes are capable of stabilizing pinwheels [31, 61, 64]. Our analysis shows that OD stripes are indeed not able to stabilize pinwheels, a result that appears to be independent of the specific type of map interaction and further independent of a detuning of typical wavelength. In line with this, several other theoretical studies, using numerical simulations [31, 61, 64], in fact indicated that more banded OD patterns lead to less pinwheel rich OP maps. For instance, in simulations using an elastic net model, the average pinwheel density of OP maps interacting with a patchy OD layout is substantially higher (about 2.5 pinwheels per hypercolumn) than for OP maps interacting with a more stripe-like OD layout (about 2 pinwheels per hypercolumn) [31].

We showed that our framework can be generalized to include any additional number of columnar systems and thus is not restricted to interactions among OD and OP maps. One reason to consider additional visual cortical maps originates from the finding that the removal of the OD map in experiments does not completely destabilize pinwheels [11]. In additions, higher feature dimensions are often treated with dimension reduction models [10, 71]. Moreover, in tree shrews, animals which completely lack OD columns, OP maps contain pinwheels and exhibit a pinwheel arrangement essentially indistinguishable from species with columnar OD segregation [70]. This might reflect the influence of additional columnar systems like spatial frequency columns that can be expected to interact with the OP map in a similar fashion as OD columns [18]. We also extended the map interaction model to more than two feature dimensions. In numerical simulations we explored coordinated optimization with three and four columnar systems. Although in this case, pinwheel stabilization is possible even without an OD bias, the resulting stationary OP patterns are either stripes or PWC solutions. Asymmetry of one feature dimension is thus not a necessary condition for pinwheel stabilization by coordinated optimization.

Experimental evidence for pinwheel stabilization by inter-map coupling

Supporting the notion that pinwheels might be stabilized by the interaction with patchy OD columns, visual cortex is indeed dominated by one eye in early postnatal development and has a pronounced patchy layout of OD domains [72–74]. Further support for the potential relevance of this picture comes from experiments in which the OD map was artificially removed resulting apparently in a significantly smoother OP map [11]. In this respect it is noteworthy that macaque visual cortex appears to exhibit all three fundamental solutions of our model for OD maps: stripes, hexagons, and a constant solution, which are stable depending on the OD bias. In the visual cortex of macaque monkeys, all three types of patterns are found to coexist [74]. Here, OD domains form bands in the binocular region and a system of ipsilateral eye patches at the transition zone to the monocular region where the contralateral eye gradually becomes more dominant, see Fig. (25) and [75]. If pinwheel stability depends on a geometric coupling to the system of OD columns one predicts systematic differences in pinwheel density between these three zones of macaque primary visual cortex.

The geometry of interaction induced pinwheel crystals

We analyzed the stationary patterns with respect to intersection angles and pinwheel positions. Remarkably, all analyzed PWC solutions and models show the tendency for iso-orientation lines to intersect OD borders perpendicularly, even in the case of the product-type energy which is not explicitly dependent on intersection angles. For the low order versions of the coupling energy the distribution of intersection angles is not continuous. Half of the pinwheels in the analyzed PWC solutions are located at OD extrema, as expected from the used coupling energies. Some pinwheels, however, are located at OD saddle-points. Remarkably, such correlations, which are expected from the gradient-type coupling energies, occur also in the case of the product-type energies. Such correlations are not expected in product-type energies per se and presumably result from the periodic layout of OP and OD maps. Correlations between pinwheels and OD saddle-points have not yet been studied quantitatively in experiments and may thus provide valuable information on the principles shaping cortical functional architecture.

How informative is map structure?

In the past numerous studies have attempted to identify signatures of coordinated optimization in the layout of visual cortical maps and to infer the validity of specific optimization models from aspects of their coordinated geometry [8, 10–17, 31–33, 61]. It was, however, never clarified theoretically in which respect and to which degree map layout and geometrical factors of inter-map relations are informative of an underlying optimization principle. Because our analysis provides complete information of the detailed relation between map geometry and optimization principle for our different models our results enable to critically assess whether different choices of energy functionals impact on the predicted map structure and conversely what can be learned about the underlying optimization principle from observations of map structures. The stabilization of pinwheel crystals for strong inter-map coupling appears to be universal and provides per se no specific information about the underlying optimization principle. In fact, the general structure of the amplitude equations is universal and only the coupling coefficients change when changing the coupling energy. It is thus expected that also for other coupling energies, respecting the proposed set of symmetries, PWC solutions can become stable for large inter-map coupling. As pointed out before, preferentially orthogonal intersection angles between iso-orientation lines and OD borders appear to be a general feature of coordinated optimization models in the strong coupling regime. Although the detailed form of the intersection angle histogram is solution and thus model specific, our analysis does not corroborate attempts to use this feature to support specific optimization principles, see also [24, 76, 77]. We identified a class of PWC solutions which become stable for large inter-map coupling. This class depends on a single parameter which is specific to the used inter-map coupling energy. This demonstrates that, although pinwheel stabilization is not restricted to a particular choice of the interaction term, each analyzed phase diagram is specific to the used coupling energy. In the strong coupling regime substantial information can thus be obtained from a detailed inspection of solutions. In the case of the product-type coupling energies, the resulting phase diagrams are relatively complex as stationary solutions and stability borders explicitly depend on the OD bias. Here, even quantitative values of model parameters could in principle be constrained by analysis of map layout. In contrast, for the gradient-type coupling energies, the bias dependence can be absorbed into the coupling strength and only selects the stationary OD pattern. This leads to rather simple phase diagrams. For these models map layout is thus uninformative of quantitative model parameters. We identified several biologically implausible OP patterns. In the case of the product-type energies, we found orientation scotoma solutions which are selective to only two preferred orientations. In the case of the low order gradient-type energy, we found OP patterns containing pinwheels with a topological charge of 1 which have not yet been observed in experiments. If the relevant terms in the coupling energy were known by other means, the parameter regions in which these patterns occur could be used to constrain model parameters by theoretical bounds. From a practical point of view, the analyzed phase diagrams and pattern properties indicate that the higher order gradient-type coupling energy is the simplest and most convenient choice for constructing models that reflect the correlations of map layouts in the visual cortex. For this coupling, intersection angle statistics is reproduced well, pinwheels can be stabilized, and pattern collapse cannot occur.

Periodic and aperiodic solutions of optimization

We presented a complete characterization of the stable OP and OD patterns, stripe-like solutions, rhombic and hexagonal crystal patterns predicted by the coordinated optimization models. The pinwheel crystals we obtained, although beautiful and easy to characterize, deviate from experimentally obtained maps in several respects. All PWC solutions that we found have a large pinwheel density of about 3.5 or even 5.2 pinwheels per hypercolumn. Densities obtained from experiments, although somewhat variable, are in the range of 3 pinwheels per hypercolumn [1, 78]. Moreover, other pinwheel statistics such as the distribution of minimal pinwheel distances have been shown to be continuous [1] whereas such distributions have distinct peaks in case of PWC solutions. In contrast to the large variability of local map layouts in experimentally observed maps, the pinwheel crystals show a regular and stereotyped structure. The reason for this difference might be the presence of biological factors neglected in the models examined here. Such factors might be realistic boundary conditions, biological noise in the system or long-range neuronal interactions. We examined whether the non-crystalline layout of visual cortical maps can result from a detuning of OP and OD wavelengths. However, while destabilizing hPWC solutions, a detuning leads to spatially regular solutions in all studied cases. Given the close agreement of model solutions and actual cortical architecture that can be achieved by including long-range interactions the latter possibility appears quite plausible [1, 52, 79]. Another relevant aspect in this respect might be the developmental stage which is represented by the maps of our model. PWC solutions represent attractor states and thus must be compared to late stages of development potentially only comparable to very late adult patterns. One might therefore expect that later in development, a crystallization of the pinwheel pattern, along with an increase in the pinwheel density takes place. With regard to this one should note that pinwheel crystals have been previously reported in several abstract [5, 36] as well as detailed synaptic plasticity based models [80–82]. Remarkably, in a model of receptive field development based on a detailed dynamics of synaptic connections the resulting OP map showed a striking similarity to the hPWC presented above, see Fig. (15) and [81]. These observations indicate that pinwheel crystallization is not an artefact of the highly idealized mathematical approach used here. In fact, the first OP map predicted ever by a synaptically based self-organization model exhibited a clearly hexagonal column arrangement [80]. Very late or very long term chronic studies of map layout are needed to assess this possibility systematically. In our models, however, crystallization is not intrinsically a process that would be restricted to very long timescales.

Conclusions

Our analysis conclusively demonstrates that OD segregation can stabilize pinwheels and induce pinwheel-rich ground states in models for the coordinated optimization of OP and OD maps even if pinwheels are intrinsically unstable in the uncoupled dynamics of the OP map. This allows to systematically assess the possibility that inter-map coupling might be the mechanism of pinwheel stabilization in the visual cortex. The analytical approach developed here is independent of the specific optimization principle and thus allowed to systematically analyze how different optimization principles impact on map layout. Moreover, our analysis clarifies to which extend the observation of the layout in physiological maps can provide information about optimization principles shaping visual cortical organization. To clarify the question of pinwheel stabilization by inter-map interaction the current study focused on models in which the scalar (OD-like) map is dominant. Recent work strongly suggests that the aperiodic pinwheel-rich layout of pinwheels and orientation columns in the visual cortex can be reproduced very well by models that represent only the orientation map but include long-range interactions [1, 31, 52]. Using the general approach developed here it is possible to construct a complementary type of models in which the complex OP map is dominant. Such models, using non-local terms in the energy functional, thus reduce to the model in [1, 31, 52] in the weak coupling limit. Because of their mathematical transparency and tractability such models are expected to provide powerful tools for examining to which extend long-range interaction models are robust against coupling to other cortical maps and how coupling to an aperiodic orientation map can shape other visual cortical representations.

Methods

Tracking and counting pinwheels

During the evolution of OD and OP maps we monitored the states from the initial time $T = 0$ to the final time $T = T_f$ using about 150 time frames. To account for the various temporal scales the dynamics encounters the time frames were separated by exponentially increasing time intervals. Pinwheel centers were identified as the crossing of the zero contour lines of the real and imaginary parts of $z(\mathbf{x})$. During time evolution we tracked all the pinwheel positions and, as the pinwheels carry a topological charge, we divided the pinwheels according to their charge. The distribution of pinwheel distances indicates the regularity and periodicity of the maps. Therefore we calculated the minimal distance between pinwheels, measured in units of the column spacing Λ during time evolution. In simulations we used periodic boundary conditions. We accounted for a 'wrap around' effect by searching also for corresponding pinwheels in periodically continued maps.

The rearrangement of OP maps leads to annihilation and creation of pinwheels in pairs. Between two time frames at T_i and T_{i+1} we identified a pinwheel to move if two pinwheels differ in position less than

$\Delta x = 0.2\Lambda$ and carry the same topological charge. If no corresponding pinwheel was found within Δx it was considered as annihilated. If a pinwheel at T_{i+1} could not be assigned to one at T_i it was considered as created. We define the pinwheel creation $c(t)$ and annihilation $a(t)$ rates per hypercolumn as

$$c(t) = \frac{dN_c}{\Lambda^2 dt}, \quad a(t) = \frac{dN_a}{\Lambda^2 dt}, \tag{88}$$

where N_c and N_a are the numbers of created and annihilated pinwheels. Creation and annihilation rates were confirmed by doubling the number of time frames.

To what extend are the pinwheels of the final pattern just rearrangements of pinwheels at some given time T? To answer this question for a given set of pinwheels at an initial time $T = T^*$ we further calculated the fraction $s(t)$ of those pinwheels surviving until time T. Finally, the fraction of pinwheels present at time T^* that survive up to the final time $T = T_f$ is given by $p(t)$.

Intersection angles

We studied the intersection angles between iso-orientation lines and OD borders. The distribution of intersection angles is given by

$$\alpha(\mathbf{x}) = \cos^{-1}\left(\frac{\nabla o(\mathbf{x}) \cdot \nabla\vartheta(\mathbf{x})}{|\nabla o(\mathbf{x})||\nabla\vartheta(\mathbf{x})|}\right), \tag{89}$$

where $\mathbf{x}$ denotes the position of the OD zero-contour lines. A continuous expression for the OP gradient is given by $\nabla\vartheta = \operatorname{Im}\nabla z/z$. We emphasized those parts of the maps from which the most significant information about the intersection angles can be obtained [19, 20]. These are the regions where the OP gradient is high and thus every intersection angle receives a statistical weight according to $|\nabla\vartheta|$.

The transition from OD stripes to OD blobs

We studied how the emerging OD map depends on the overall eye dominance. To this end we mapped the uncoupled OD dynamics to a Swift-Hohenberg equation containing a quadratic interaction term instead of a constant bias. This allowed for the use of weakly nonlinear analysis to derive amplitude equations as an approximate description of the shifted OD dynamics near the bifurcation point. We identified the stationary solutions and studied their stability properties. Finally, we derived expressions for the fraction of contralateral eye dominance for the stable solutions.

Mapping to a dynamics with a quadratic term

Here we describe how to map the Swift-Hohenberg equation

$$\partial_t\, o(\mathbf{x},t) = \hat{L}\, o(\mathbf{x},t) - o(\mathbf{x},t)^3 + \gamma\,, \tag{90}$$

to one with a quadratic interaction term. To eliminate the constant term we shift the field by a constant amount $o(\mathbf{x},t) = \widetilde{o}(\mathbf{x},t) + \delta$. This changes the linear and nonlinear terms as

$$\begin{aligned} \hat{L}\, o \quad &\rightarrow \quad \hat{L}\,\widetilde{o} - \left(k_c^4 - r_o\right)\delta \\ o^3 \quad &\rightarrow \quad -\widetilde{o}^3 + 3\delta\widetilde{o}^2 + 3\delta^2\widetilde{o} + \delta^3\,. \end{aligned} \tag{91}$$

We define the new parameters $\widetilde{r}_o = r_o - 3\delta^2$ and $\widetilde{\gamma} = -3\delta$. This leads to the new dynamics

$$\partial_t\,\widetilde{o} = \widetilde{r}_o\,\widetilde{o} - \left(k_c^2 + \Delta\right)^2\widetilde{o} + \widetilde{\gamma}\widetilde{o}^2 - \widetilde{o}^3 - \delta^3 - \left(k_{c,o}^4 - r_o\right)\delta + \gamma\,. \tag{92}$$

The condition that the constant part is zero is thus given by

$$-\,\delta^3 - \left(k_c^4 - r_o\right)\delta + \gamma = 0\,. \tag{93}$$

For $r_o < 1$ the real solution to Eq. (93) is given by

$$\delta = \frac{2^{1/3}\,(k_c - r_o)}{\beta} - \frac{\beta}{3\,2^{1/3}}\,, \tag{94}$$

with $\beta = \left(-27\gamma + \sqrt{108\,(r_o - k_c)^3 + 729\gamma^2}\right)^{1/3}$. For small γ this formula is approximated as

$$\delta \approx \gamma \frac{1}{k_c^4 - r_o} - \gamma^3 \frac{1}{(k_c^4 - r_o)^4} + 3\gamma^5 \frac{1}{(k_c^4 - r_o)^7} + \ldots \tag{95}$$

The uncoupled OD dynamics we consider in the following is therefore given by

$$\partial_t\, \widetilde{o} = \widetilde{r}_o \widetilde{o} - \left(k_c^2 + \Delta\right)^2 \widetilde{o} + \widetilde{\gamma} \widetilde{o}^2 - \widetilde{o}^3\,. \tag{96}$$

This equation has been extensively studied in pattern formation literature [50].

Amplitude equations for OD patterns

We studied Eq. (96) using weakly nonlinear analysis. This method leads to amplitude equation as an approximate description of the full field dynamics Eq. (96) near the bifurcation point $\widetilde{r}_o = 0$. We summarize the derivation of the amplitude equations for the OD dynamics which is of the form

$$\partial_t\, o(\mathbf{x}, t) = \hat{L}\, o(\mathbf{x}, t) + N_2[o, o] - N_3[o, o, o]\,, \tag{97}$$

with the linear operator $\hat{L} = r_o - \left(k_{c,o}^2 + \Delta\right)^2$. In this section we use for simplicity the variables (o, r_o, γ) instead of $(\tilde{o}, \tilde{r}_o, \tilde{\gamma})$. The derivation is performed for general quadratic and cubic nonlinearities but are specified later according to Eq. (10) as $N_3[o, o, o] = o^3$ and $N_2[o, o] = \gamma\, o^2$. For the calculations in the following, it is useful to separate r_o from the linear operator

$$\hat{L} = r_o + \hat{L}^0\,, \tag{98}$$

therefore the largest eigenvalue of $\hat{L}^0$ is zero. The amplitude of the field $o(\mathbf{x}, t)$ is assumed to be small near the onset $r_o = 0$ and thus the nonlinearities are small. We therefore expand both the field $o(\mathbf{x}, t)$ and the control parameter r_o in powers of a small expansion parameter μ as

$$o(\mathbf{x}, t) = \mu\, o_1(\mathbf{x}, t) + \mu^2 o_2(\mathbf{x}, t) + \mu^3 o_3(\mathbf{x}, t) + \ldots\,, \tag{99}$$

and

$$r_o = \mu r_1 + \mu^2 r_2 + \mu^3 r_3 + \ldots \tag{100}$$

The dynamics at the critical point $r_o = 0$ becomes arbitrarily slow since the intrinsic timescale $\tau = r_o^{-1}$ diverges at the critical point. To compensate we introduce a rescaled time scale T as

$$T = r_o\, t, \quad \partial_t = r_o\, \partial_T\,. \tag{101}$$

In order for all terms in Eq. (97) to be of the same order the quadratic interaction term N_2 must be small. We therefore rescale N_2 as $\sqrt{r_o} N_2$. This preserves the nature of the bifurcation compared to the case $N_2 = 0$.

We insert the expansion Eq. (99) and Eq. (100) in the dynamics Eq. (97) and get

$$\begin{aligned} 0 \;&=\; \mu\, \hat{L}^0 o_1 \\ &+\; \mu^2 \left(-\hat{L}^0 o_2 - r_1 \partial_T o_1 + r_1 o_1 + \sqrt{\mu r_1 + \mu^2 r_2 + \ldots}\, N_2[o_1, o_1]\right) \\ &+\; \mu^3 \left(-\hat{L}^0 o_3 + r_1\,(o_2 - \partial_T o_2) + r_2\,(o_1 - \partial_T o_1) - N_3[o_1, o_1, o_1]\right) \\ &\;\;\vdots \end{aligned} \tag{102}$$

We sort and collect all terms in order of their power in μ. The equation can be fulfilled for $\mu > 0$ only if each of these terms is zero. We therefore solve the equation order by order. In the leading order we get the homogeneous equation

$$\hat{L}^0 o_1 = 0\,. \tag{103}$$

Thus o_1 is an element of the kernel of $\hat{L}^0$. The kernel contains linear combinations of modes with wavevector $\vec{k}_j$ on the critical circle $|\vec{k}_j| = k_{c,o}$. At this level any of such wavevectors is possible. We choose

$$o_1 = \sum_j^n B_j(T) e^{\imath \vec{k}_j \vec{x}} + \sum_j^n \overline{B}_j(T) e^{-\imath \vec{k}_j \vec{x}}\,, \tag{104}$$

where the wavevectors are chosen to be equally spaced $\vec{k}_j = k_{c,o}\,(\cos(j\pi/n), \sin(j\pi/n))$ and the complex amplitudes $B_j = \mathcal{B}_j e^{\imath\psi_j}$. The homogeneous equation leaves the amplitudes B_j undetermined. These amplitudes are fixed by the higher order equations. Besides the leading order homogeneous equation we get inhomogeneous equations of the form

$$\hat{L}^0 o_m = F_m \tag{105}$$

To solve this inhomogeneous equation we first apply a solvability condition. We thus apply the *Fredholm Alternative theorem* to Eq. (105). Since the operator $\hat{L}^0$ is self-adjoint $\hat{L}^0 = \hat{L}^{0\,\dagger}$, the equation is solvable if and only if F_m is orthogonal to the kernel of $\hat{L}^0$ i.e.

$$\langle F_m, \tilde{o}\rangle = 0, \quad \forall\, \hat{L}^0 \tilde{o} = 0 \tag{106}$$

The orthogonality to the kernel can be expressed by a projection operator $\hat{P}_c$ onto the kernel and the condition $\langle F, \tilde{o}\rangle = 0$ can be rewritten as $\hat{P}_c F = 0$.
At second order we get

$$\hat{L}^0 o_2 = r_1\,(o_1 - \partial_T o_1)\;. \tag{107}$$

Applying the solvability condition Eq. (106) we see that this equation can be fulfilled only for $r_1 = 0$. At third order we get

$$\hat{L}^0 o_3 = r_2\,(o_1 - \partial_T o_1) + N_2[o_1, o_1] - N_3[o_1, o_1, o_1]\,. \tag{108}$$

The parameter r_2 sets the scale in which o_1 is measured and we can set $r_2 = 1$. We apply the solvability condition and get

$$\partial_T\, o_1 = o_1 + \hat{P}_c N_2[o_1, o_1] - \hat{P}_c N_3[o_1, o_1, o_1]\,. \tag{109}$$

We insert our ansatz Eq. (104) which leads to the amplitude equations at third order

$$\partial_T B_i = B_i + \hat{P}_i \sum_{j,k} B_j B_k e^{-\imath\vec{k}_i\vec{x}} N_2[e^{\imath\vec{k}_j\vec{x}}, e^{\imath\vec{k}_k\vec{x}}] - \hat{P}_i \sum_{j,k} B_j B_k B_l e^{-\imath\vec{k}_i\vec{x}} N_3[e^{\imath\vec{k}_j\vec{x}}, e^{\imath\vec{k}_k\vec{x}}, e^{\imath\vec{k}_l\vec{x}}]\,, \tag{110}$$

where $\hat{P}_i$ is the projection operator onto the subspace $\{e^{\imath\vec{k}_i\vec{x}}\}$ of the kernel. $\hat{P}_i$ picks out all combinations of the modes which have their wavevector equal to $\vec{k}_i$. In our case the three active modes form a so called triad resonance $\vec{k}_1 + \vec{k}_2 + \vec{k}_3 = 0$. The quadratic coupling terms which are resonant to the mode B_1 are therefore given by

$$\overline{B}_2 \overline{B}_3 e^{-\imath\vec{k}_1\vec{x}} \left(N_2[e^{-\imath\vec{k}_2\vec{x}}, e^{-\imath\vec{k}_3\vec{x}}] + N_2[e^{-\imath\vec{k}_3\vec{x}}, e^{-\imath\vec{k}_2\vec{x}}] \right)\,. \tag{111}$$

Resonant contributions from the cubic nonlinearity result from terms of the form $|B_j|^2 B_i$. Their coupling coefficients are given by

$$\begin{aligned} \widetilde{g}_{ij} \;=\; & N_3[e^{\imath\vec{k}_i\vec{x}}, e^{\imath\vec{k}_j\vec{x}}, e^{-\imath\vec{k}_j\vec{x}}] + N_3[e^{\imath\vec{k}_i\vec{x}}, e^{-\imath\vec{k}_j\vec{x}}, e^{\imath\vec{k}_j\vec{x}}] + N_3[e^{\imath\vec{k}_j\vec{x}}, e^{\imath\vec{k}_i\vec{x}}, e^{-\imath\vec{k}_j\vec{x}}] + \\ & N_3[e^{-\imath\vec{k}_j\vec{x}}, e^{\imath\vec{k}_i\vec{x}}, e^{\imath\vec{k}_j\vec{x}}] + N_3[e^{\imath\vec{k}_j\vec{x}}, e^{-\imath\vec{k}_j\vec{x}}, e^{\imath\vec{k}_i\vec{x}}] + N_3[e^{-\imath\vec{k}_j\vec{x}}, e^{\imath\vec{k}_j\vec{x}}, e^{\imath\vec{k}_i\vec{x}}]\,, \end{aligned} \tag{112}$$

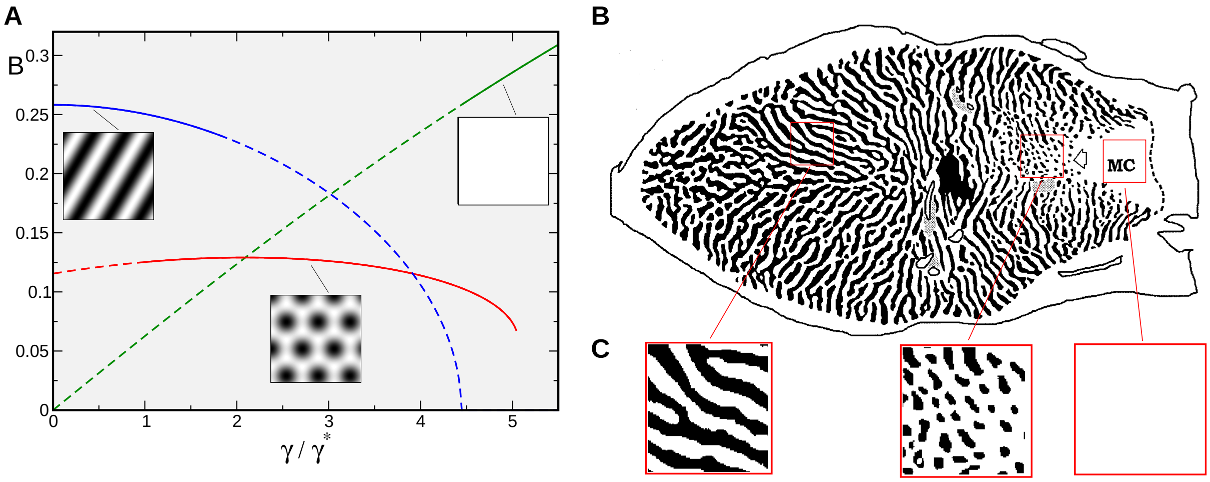

Figure 25. OD patterns. **A** Stationary amplitudes of the OD dynamics. The course of $\mathcal{B}_{st}(\gamma)$ Eq. (115) (blue), $\mathcal{B}_{hex}(\gamma)$ Eq. (116) (red), and of $\delta(\gamma)$ Eq. (94) (green) for $r_o = 0.2$. The solutions are plotted in solid lines within their stability ranges. **B** OD map of macaque monkey. Adapted from [74]. **C** Details of **B** with stripe-like, patchy, and homogeneous layout.

and

$$\widetilde{g}_{ii} = N_3[e^{\imath\vec{k}_i\vec{x}}, e^{\imath\vec{k}_i\vec{x}}, e^{-\imath\vec{k}_i\vec{x}}] + N_3[e^{\imath\vec{k}_i\vec{x}}, e^{-\imath\vec{k}_i\vec{x}}, e^{\imath\vec{k}_i\vec{x}}] + N_3[e^{-\imath\vec{k}_i\vec{x}}, e^{\imath\vec{k}_i\vec{x}}, e^{\imath\vec{k}_i\vec{x}}]\,. \tag{113}$$

When specifying the nonlinearities Eq. (10) the coupling coefficients are given by $\widetilde{g}_{ij} = 6, \widetilde{g}_{ii} = 3$. Finally, the amplitude equations (here in the shifted variables $(\tilde{r}_o, \tilde{\gamma})$ are given by

$$\partial_t B_1 = \widetilde{r}_o B_1 - 3|B_1|^2 B_1 - 6\left(|B_2|^2 + |B_3|^2\right) B_1 + 2\widetilde{\gamma}\overline{B}_2\overline{B}_3\,, \tag{114}$$

where we scaled back to the original time variable t. Equations for B_2 and B_3 are given by cyclic permutation of the indices.

Stationary solutions

The amplitude equations (114) have three types of stationary solutions, namely OD stripes

$$o_{st}(\mathbf{x}) = 2\mathcal{B}_{st}\cos\left(x + \psi\right) + \delta, \tag{115}$$

with $\mathcal{B}_{st} = \sqrt{\tilde{r}/3}$, hexagons

$$o_{hex}(\mathbf{x}) = \mathcal{B}_{hex}\sum_{j=1}^{3} e^{\imath\psi_j} e^{\imath\vec{k}_j\vec{x}} + c.c. + \delta, \tag{116}$$

with the resonance condition $\sum_j^3 \vec{k}_j = 0$ and $\mathcal{B}_{hex} = -\tilde{\gamma}/15 + \sqrt{(\tilde{\gamma}/15)^2 + \tilde{r}/15}$. Finally, there is a homogeneous solution with spatially constant eye dominance

$$o_c(\mathbf{x}) = \delta. \tag{117}$$

The spatial average of all solutions is $\langle o(\mathbf{x})\rangle = \delta$. The course of $\mathcal{B}_{st}$, $\mathcal{B}_{hex}$, and of $\delta(\gamma)$ is shown in Fig. 25**A**.

Linear stability analysis for OD patterns

We decomposed the amplitude equations (114) into the real and imaginary parts. From the imaginary part we get the phase equation

$$\partial_t \psi_1 = -2\widetilde{\gamma} \sin\left(\psi_1 + \psi_2 + \psi_3\right) \,, \tag{118}$$

and equations for ψ_2, ψ_3 by cyclic permutation of the indices. The stationary phases are given by $\psi_1 + \psi_2 + \psi_3 = \{0, \pi\}$. The phase equation can be derived from the potential $V[\psi] = -2\widetilde{\gamma} \cos(\psi_1 + \psi_2 + \psi_3)$. We see that the solution $\psi_1 + \psi_2 + \psi_3 = 0$ is stable for $\widetilde{\gamma} > 0 (\gamma < 0)$ and the solution $\psi_1 + \psi_2 + \psi_3 = \pi$ is stable for $\widetilde{\gamma} < 0 (\gamma > 0)$.

We calculate the stability borders of the OD stripe, hexagon, and constant solution in the uncoupled case. This treatment follows [50]. In case of stripes the three modes of the amplitude equations are perturbed as

$$B_1 \rightarrow B_{st} + b_1 \,, \quad B_2 \rightarrow b_2 \,, \quad B_3 \rightarrow b_3, \tag{119}$$

assuming small perturbations b_1, b_2, and b_3. This leads to the linear equations $\partial_t \vec{b} = M\vec{b}$ with the stability matrix

$$M = \begin{pmatrix} \widetilde{r} - 9B_{st}^2 & 0 & 0 \\ 0 & \widetilde{r} - 6B_{st}^2 & 2\widetilde{\gamma} B_{st} \\ 0 & 2\widetilde{\gamma} B_{st} & \widetilde{r} - 6B_{st}^2 \end{pmatrix} . \tag{120}$$

The corresponding eigenvalues are given by

$$\lambda = \left(-2\widetilde{r}, -\widetilde{r} - 2\sqrt{\widetilde{r}/3}\widetilde{\gamma}, -\widetilde{r} + 2\sqrt{\widetilde{r}/3}\widetilde{\gamma}\right) . \tag{121}$$

This leads to the two borders for the stripe stability

$$\widetilde{r} = 0, \quad \widetilde{r} = \frac{4}{3}\widetilde{\gamma}^2 . \tag{122}$$

In terms of the original variables r_o, γ the borders are given by $(0 < r_o < 1)$

$$\gamma_3^* = \frac{(3 - 2r_o)\sqrt{r_o}}{3^{3/2}}, \quad \gamma_2^* = \frac{(15 - 14r_o)\sqrt{r_o}}{15^{3/2}} . \tag{123}$$

To derive the stability borders for the hexagon solution $o_{hex}(\mathbf{x})$ we perturb the amplitudes as

$$B_1 \rightarrow B_{hex} + b_1 \,, \quad B_2 \rightarrow B_{hex} + b_2 \,, \quad B_3 \rightarrow B_{hex} + b_3 \,. \tag{124}$$

The stability matrix is then given by

$$M = \begin{pmatrix} -21B_{hex} + \widetilde{r} & -12B_{hex}^2 - 2B_{hex}\widetilde{\gamma} & -12B_{hex}^2 - 2B_{hex}\widetilde{\gamma} \\ -12B_{hex}^2 - 2B_{hex}\widetilde{\gamma} & -21B_{hex} + \widetilde{r} & -12B_{hex}^2 - 2B_{hex}\widetilde{\gamma} \\ -12B_{hex}^2 - 2B_{hex}\widetilde{\gamma} & -12B_{hex}^2 - 2B_{hex}\widetilde{\gamma} & -21B_{hex} + \widetilde{r} \end{pmatrix} , \tag{125}$$

and the corresponding eigenvalues are given by

$$\lambda = \left(-45B_h^2 + \widetilde{r} - 4B_h\widetilde{\gamma}, -9B_h^2 + \widetilde{r} + 2B_h\widetilde{\gamma}, -9B_h^2 + \widetilde{r} + 2B_h\widetilde{\gamma}\right) . \tag{126}$$

The stability borders for the hexagon solution are given by

$$\widetilde{r} = -\frac{1}{15}\widetilde{\gamma}^2, \quad \widetilde{r} = \frac{16}{3}\widetilde{\gamma}^2 . \tag{127}$$

In terms of the original variables we finally get

$$\gamma_4^* = \frac{(12 - 7r_o)\sqrt{r_o}\sqrt{5}}{24\sqrt{3}}, \quad \gamma^* = \frac{(51 - 50r_o)\sqrt{r_o}}{51^{3/2}} . \tag{128}$$

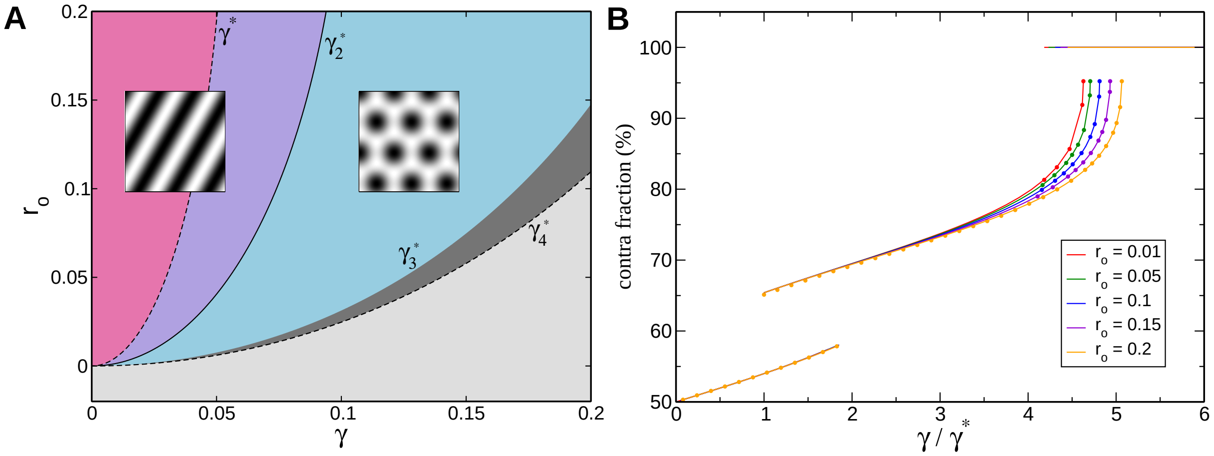

Figure 26. The uncoupled OD dynamics. A Phase diagram of the OD model Eq. (90). Dashed lines: stability border of hexagon solutions, solid line: stability border of stripe solution, gray regions: stability region of constant solution **B** Percentage of neurons dominated by the contralateral eye plotted for the three stationary solutions. Circles: numerically obtained values, solid lines: C_{st} and C_{hex}.

The phase diagram of this model is depicted in Fig. 26**A**. It shows the stability borders $\gamma^*, \gamma_2^*, \gamma_3^*$, and γ_4^* for the three solutions obtained by linear stability analysis. Without a bias term the OD map is either constant, for $r_o < 0$, or has a stripe layout, for $r_o > 0$. For positive r_o and increasing bias term there are two transition regions, first a transition region from stripes to hexagons and second a transition region from hexagons to the constant solution.
The spatial layout of the OD hexagons consists of hexagonal arrays of ipsilateral eye dominance blobs in a sea of contralateral eye dominance, see Fig. 26**A**.

Contralateral eye fraction

To compare the obtained solutions with physiological OD maps we quantified the fraction of neurons selective to the contralateral eye inputs. For stripe and hexagon solutions we thus calculated the fraction of contralateral eye dominated territory C_{st} and C_{hex}. In case of stripes this is a purely one-dimensional problem. The zeros of the field are given by

$$o_{st}(x) = 2\mathcal{B}_{st}\cos(x+\psi) + \delta = 0\,, \tag{129}$$

with the solution

$$x = \arccos\left(\frac{-\delta}{2\mathcal{B}_{st}}\right)\,. \tag{130}$$

As the field has a periodicity of π the area fraction is given by

$$C_{st} = \arccos\left(\frac{-\delta}{2\mathcal{B}_{st}}\right)/\pi\,. \tag{131}$$

In case of hexagons we observe that the territory of negative $o(\mathbf{x})$ values is approximately a circular area. We obtain the fraction of negative $o(\mathbf{x})$ values by relating this area to the area of the whole hexagonal lattice. In case of hexagons the field is given by

$$o_{hex}(\mathbf{x}) = 2\mathcal{B}_{hex}\sum_j \cos\left(\vec{k}_j\vec{x} + \psi_j\right) + \delta\,. \tag{132}$$

As an approximation we project the field onto the x-axis and choose for simplicity $\psi_j = 0, \forall j$. The field has its maximum at the origin $o_{hex}(0,0) = 6 + \delta$. The projection leads to

$$f(x) = 2\mathcal{B}_{hex} \left(\cos x + 2\cos(1/2)x\right) + \delta \,. \tag{133}$$

The zeros $f(x_1) = 0$ are located at

$$x_1 = 2 \arccos\left(\frac{1}{2}\left(-1 + \sqrt{3 + \frac{\delta}{\mathcal{B}_{hex}}}\right)\right) \,. \tag{134}$$

The circular area of positive $o_{hex}(\mathbf{x})$ values is now given by $A_c = \pi x_1^2$. The periodicity of the hexagonal pattern is given by $f(x_2)_{\delta=0} = \min(f)_{\delta=0} = -3$. This leads to $x_2 = 4\pi/3$. The area of the hexagon is therefore given by $A_{hex} = 3x_2^2\sqrt{3}/2$. The contra fraction is finally given by

$$1 - C_{hex} \approx \frac{A_c}{A_{hex}} = \frac{\sqrt{3}}{2\pi} \arccos\left(\frac{1}{2}\left(-1 + \sqrt{3 + \frac{\delta}{\mathcal{B}_{hex}}}\right)\right)^2 \,. \tag{135}$$

The course of the fractions C_{st} and C_{hex} is shown in Fig. 26**B**. At the border $\gamma = \gamma^*$, where hexagons become stable $C_{hex} \approx 65.4\%$. At the border $\gamma = \gamma_4^*$, where hexagons loose stability $C_{hex} \approx 95.2\%$. Both quantities are independent of r_o. We confirmed our results by direct numerical calculation of the fraction of positive $o_{hex}(\mathbf{x})$ pixel values. Deviations from the result Eq. (135) are small. For $\gamma/\gamma^* \approx 1$ the zeros of Eq. (133) are not that well approximated with a circular shape and the projection described above leads to the small deviations which decrease with increasing bias γ.

Numerical integration scheme

As the Swift-Hohenberg equation is a stiff partial differential equation we used a fully implicit integrator [83]. Such an integration scheme avoids numerical instabilities and enables the use of increasing step sizes when approaching an attractor state. The equation

$$\partial_t \, z(\mathbf{x}, t) = \hat{L} z(\mathbf{x}, t) - N[z(\mathbf{x}, t)] \,, \quad \hat{L} = r - \left(k_c^2 + \Delta\right)^2 \,, \tag{136}$$

is discretized in time. Using a Crank-Nicolson scheme this differential equation is approximated by the nonlinear difference equation

$$\frac{z_{t+1} - z_t}{\Delta t} = \frac{\left(\hat{L} z_{t+1} + N[z_{t+1}]\right) + \left(\hat{L} z_t + N[z_t]\right)}{2}. \tag{137}$$

This equation is solved iteratively for z_{t+1} with the help of the Newton method which finds the root of the function

$$G[z_{t+1}] = \left(-\hat{L} + \frac{2}{\Delta t}\right) z_{t+1} - N[z_{t+1}] - \left(\left(\hat{L} + \frac{2}{\Delta t}\right) z_t + N[z_t]\right) \,. \tag{138}$$

The field $z(\mathbf{x})$ is discretized. For a grid with N meshpoints in x-direction and M meshpoints in y-direction this leads to a $M \times N$ dimensional state vector $\mathbf{u}$. Discretization is performed in Fourier space. The Newton iteration at step k is then given by

$$DG(u^k)\Delta\mathbf{u}^k = -G(\mathbf{u}^k), \quad \mathbf{u}^{k+1} = \mathbf{u}^k + \Delta\mathbf{u}^k \,, \tag{139}$$

with DG the Jacobian of G. Instead of calculating the matrix DG explicitly a matrix free method is used, where the action of the matrix is approximated using finite differences. To solve the linear system

$A\mathbf{x} = \mathbf{b}$ with $A = DG(\mathbf{u}^k)$, $\mathbf{b} = -G(\mathbf{u}^k)$ we used the Krylov subspace method [83]. The Krylov subspace of dimensionality k is defined as

$$\mathcal{K}_k(A, \mathbf{v}_1) = \text{span}\{\mathbf{v}_1, A\mathbf{v}_1, A^2\mathbf{v}_1, \ldots, A^{k-1}\mathbf{v}_1\}\,. \tag{140}$$

In the *Generalized Minimum Residual* (GMRES) algorithm the Krylov subspace is generated by $\mathbf{v}_1 = \mathbf{r}_0/|\mathbf{r}_0|$ with $\mathbf{r}_0 = A\mathbf{x}_0 - \mathbf{b}$, and $\mathbf{x}_0$ an initial guess, see [83]. After k iterations, the refined solution is given by

$$\mathbf{x}_k = \mathbf{x}_0 + V_k\mathbf{y}\,, \tag{141}$$

where the matrix $V_k = (\mathbf{v}_1, \ldots, \mathbf{v}_k)$ has the base vectors of the Krylov subspace as its columns. The vector $\mathbf{y}$ is chosen by minimizing the residuum

$$\|b - A\mathbf{x}_k\|_2 = \|r_0 - AV_k\mathbf{y}\|_2 \overset{!}{=} \min\,, \tag{142}$$

where $\|.\|_2$ denotes the Euclidean norm. For this procedure an orthonormal basis of the Krylov subspace is generated with an Arnoldi process. With the use of the similarity transformation

$$AV_k = V_{k+1}\tilde{H}_k\,, \tag{143}$$

where $\tilde{H}_k$ is an upper Hessenberg matrix, $\mathbf{v}_1 = \mathbf{r}_0/|\mathbf{r}_0|$, and the orthogonality of V_k, the optimality condition Eq. (142) becomes

$$\|\tilde{H}_k\mathbf{y} - |\mathbf{b}|\mathbf{e}_1\|_2 \overset{!}{=} \min\,, \tag{144}$$

with $\mathbf{e}_1 = (1, 0, \ldots, 0)$ the first unit vector of dimension $k + 1$. For a $\mathbf{y}$ that minimizes this norm the approximate solution is given by $\mathbf{x}_k = \mathbf{x}_0 + V_k\mathbf{y}$. To improve the convergence of this iterative method preconditioning was used. A preconditioner M is multiplied to $A\mathbf{x} = \mathbf{b}$ such that $M^{-1}A$ is close to unity. A preconditioner suitable for our model is the inverse of the linear operator in Fourier space with a small shift $0 < \epsilon \ll 1$ in order to avoid singularities i.e.

$$M = \left(\epsilon + \left(k^2 - k_c^2\right)^2 + \frac{2}{\Delta t}\right)^{-1}\,. \tag{145}$$

The convergence of Newton's method is only guaranteed from a starting point close enough to a solution. In the integration scheme we use a line search method to ensure also a global convergence [84]. Newton's method Eq. (139) is thus modified as

$$\mathbf{u}^{k+1} = \mathbf{u}^k + \lambda\Delta\mathbf{u}^k\,, \tag{146}$$

where the function

$$f(\mathbf{u}^k) = \frac{1}{2}G(\mathbf{u}^k)G(\mathbf{u}^k), \tag{147}$$

is iteratively minimized with respect to λ.

This integrator was implemented using the *PetSc* library [85]. As the dynamics converges towards an attractor an adaptive stepsize control is very efficient. The employed adaptive stepsize control was implemented as described in [86]. The described integration scheme has been generalized for an arbitrary number of real or complex fields. The coupling terms are treated as additional nonlinearities in N. As a common intrinsic timescale we choose $T = tr_z$ with r_z the bifurcation parameter of the OP map. Due to the spatial discretization not all points of the critical circle lie on the grid. Thus, the maximal growth rate on the discretized circle is not exactly equal to r, the theoretical growth rate. In particular, some modes may be suppressed or even become unstable. Due to this we expect deviations from analytical solutions. To minimize such deviations the size of the critical circle was chosen such that this disbalance between the active modes was minimized. Periodic boundary conditions were applied to account for the translation invariance of the spatial pattern.

Acknowledgments

We thank Ghazaleh Afshar, Eberhard Bodenschatz, Theo Geisel, Min Huang, Wolfgang Keil, Michael Schnabel, Dmitry Tsigankov, and Juan Daniel Flórez Weidinger for discussions. This work was supported by the HFSP, BMBF, and the MPG.

Appendix

Coupling coefficients

In this appendix we list the explicit form of the coupling tensor $l^{(u)}_{ijlk}$ of the coupled amplitude equations (71). They have the symmetry $h^{(u)}_{ijlk} = h^{(u)}_{iljk}, u = 1, 2, 4, 5$.

$$
\begin{aligned}
h^{(1)}_{iiii} &= 40.5\,\epsilon + 90\,\tau, & h^{(1)}_{iiij} &= (16.125\,\epsilon + 48\,\tau)\; e^{\imath(\psi_j - \psi_i)},\\
h^{(1)}_{ijjj} &= (16.125\,\epsilon + 48\,\tau)\; e^{\imath(\psi_i - \psi_j)}, & h^{(1)}_{iijj} &= 40.5\,\epsilon + 180\,\tau,\\
h^{(1)}_{iiji} &= (32.25\,\epsilon + 96\,\tau)\; e^{\imath(\psi_i - \psi_j)}, & h^{(1)}_{ijji} &= (4.125\,\epsilon + 6\,\tau)\; e^{\imath 2(\psi_i - \psi_j)},\\
h^{(1)}_{iijl} &= -\,(16.5\,\epsilon + 96\,\tau)\; e^{\imath(\psi_l - \psi_j)}, & h^{(1)}_{ijli} &= (7.5\,\epsilon + 24\,\tau)\; e^{\imath(2\psi_i - \psi_j - \psi_l)},\\
h^{(1)}_{ijll} &= (16.5\,\epsilon + 96\,\tau)\; e^{\imath(\psi_i - \psi_j)}, & h^{(1)}_{ijjl} &= (3.75\,\epsilon + 12\,\tau)\; e^{\imath(\psi_l + \psi_i - 2\psi_j)}
\end{aligned}
$$

In terms containing also the opposite wavevectors A_{j^-} triad resonances $\vec{k}_1 + \vec{k}_2 + \vec{k}_3$ appear. They lead to the phase relation $\psi_1 + \psi_2 + \psi_3 = \pi$ for the modes B_j and therefore the coupling coefficients depend only on two of the three phases.

$$
\begin{aligned}
h^{(2)}_{iiii} &= (19.25\,\epsilon + 34\,\tau)\; e^{2\imath\psi_i}, & h^{(2)}_{ijjj} &= (15.75\,\epsilon + 60\,\tau)\; e^{\imath(\psi_i + \psi_j)},\\
h^{(2)}_{iiij} &= (3.5\,\epsilon + 4\,\tau)\; e^{\imath(3\psi_i - \psi_j)}, & h^{(2)}_{iiji} &= (31.5\,\epsilon + 120\,\tau)\; e^{\imath(\psi_i + \psi_j)},\\
h^{(2)}_{ijji} &= (9.875\,\epsilon + 34\,\tau)\; e^{\imath\psi_j}, & h^{(2)}_{iijj} &= (19.75\,\epsilon + 68\,\tau)\; e^{2\imath\psi_i},\\
h^{(2)}_{iijl} &= -\,(7.25\,\epsilon + 32\,\tau)\; e^{\imath(3\psi_i + 2\psi_j)}, & h^{(2)}_{ijli} &= (9\,\epsilon + 120\,\tau)\; e^{\imath\psi_i},\\
h^{(2)}_{ijll} &= (9\,\epsilon + 120\,\tau)\; e^{\imath(\psi_i + \psi_j)}, & h^{(2)}_{ijjl} &= -\,(3.625\,\epsilon + 16\,\tau)\; e^{\imath(2\psi_i + 3\psi_j)}
\end{aligned}
$$

$$
\begin{aligned}
h^{(3)}_{iiii} &= (38.5\,\epsilon + 68\,\tau)\; e^{2\imath\psi_i}, & h^{(3)}_{ijjj} = h^{(3)}_{iiij} = h^{(3)}_{iiji} &= (31.5\,\epsilon + 120\,\tau)\; e^{\imath(\psi_i + \psi_j)}\\
h^{(3)}_{ijii} &= (7\,\epsilon + 8\,\tau)\; e^{\imath(3\psi_i - \psi_j)}, & h^{(3)}_{iijj} &= (19.75\,\epsilon + 68\,\tau)\; e^{2\imath\psi_j},\\
h^{(3)}_{ijji} = h^{(3)}_{ijij} &= (19.75\,\epsilon + 68\,\tau)\; e^{2\imath\psi_i}, & h^{(3)}_{iijl} &= -\,(9\,\epsilon + 120\,\tau)\; e^{\imath\psi_i},\\
h^{(3)}_{ijil} = h^{(3)}_{ijli} &= -\,(7.25\,\epsilon + 32\,\tau)\; e^{\imath(\psi_i - 2\psi_j)}, & h^{(3)}_{ijll} &= (7.25\,\epsilon + 32\,\tau)\; e^{-\imath(\psi_i + 3\psi_j)},\\
h^{(3)}_{iljl} &= (9\,\epsilon + 120\,\tau)\; e^{\imath(\psi_i + \psi_j)}, & h^{(3)}_{ijjl} &= -\,(9\,\epsilon + 120\,\tau)\; e^{-\imath\psi_j}
\end{aligned}
$$

$$
\begin{aligned}
h^{(4)}_{iiii} &= (2\,\epsilon + \tau)\; e^{4\imath\psi_i}, & h^{(4)}_{ijjj} &= (3.125\,\epsilon + 16\,\tau)\; e^{\imath(\psi_i + 3\psi_j)},\\
h^{(4)}_{iiij} &= (3.125\,\epsilon + 16\,\tau)\; e^{\imath(3\psi_i + \psi_j)}, & h^{(4)}_{iiji} &= 2\,h^{(4)}_{iiij},\\
h^{(4)}_{ijji} &= (5.125\,\epsilon + 34\,\tau)\; e^{2\imath(\psi_i + \psi_j)}, & h^{(4)}_{iijj} &= 2\,h^{(4)}_{ijji},\\
h^{(4)}_{iijl} = h^{(4)}_{ijli} &= (9\,\epsilon - 120\,\tau)\; e^{\imath\psi_i}, & h^{(4)}_{ijll} &= (-9\,\epsilon + 120\,\tau)\; e^{-\imath(\psi_i + \psi_j)},\\
h^{(4)}_{ijjl} &= (4.5\,\epsilon - 60\,\tau)\; e^{\imath\psi_j}
\end{aligned}
$$

$$\begin{aligned}
h^{(5)}_{iiii} &= (19.25\,\epsilon + 34\,\tau)\ e^{-2\imath\psi_i}, & h^{(5)}_{ijjj} &= (3.5\,\epsilon + 4\,\tau)\ e^{\imath(\psi_i - 3\psi_j)},\\
h^{(5)}_{iiij} &= (15.75\,\epsilon + 60\,\tau)\ e^{-\imath(\psi_i + \psi_j)}, & h^{(5)}_{iiji} &= 2\,h^{(5)}_{iiij},\\
h^{(5)}_{ijji} &= (9.875\,\epsilon + 34\,\tau)\ e^{-2\imath\psi_j}, & h^{(5)}_{iijj} &= 2\,h^{(5)}_{ijji},\\
h^{(5)}_{ijll} &= (7.25\,\epsilon + 32\,\tau)\ e^{\imath(3\psi_i + \psi_j)}, & h^{(5)}_{ijjl} &= -\,(3.625\,\epsilon + 16\,\tau)\ e^{\imath(2\psi_i - \psi_j)},\\
h^{(5)}_{iijl} = h^{(5)}_{ijli} &= -\,(9\,\epsilon + 120\,\tau)\ e^{\imath\psi_i}
\end{aligned}$$

$$\begin{aligned}
h^{(6)}_{iiii} &= (2\,\epsilon + 180\,\tau)\,e^{\imath\psi_i}, & h^{(6)}_{iiji} &= (32.25\,\epsilon + 96\,\tau)\ e^{\imath(-\psi_i + \psi_j)},\\
h^{(6)}_{ijjj} = h^{(6)}_{iiij} = h^{(6)}_{ijii} &= (32.25\,\epsilon + 96\,\tau)\ e^{\imath(\psi_i - \psi_j)},\\
h^{(6)}_{ijji} = h^{(6)}_{iijj} &= (40.5\,\epsilon + 180\,\tau)\,, & h^{(6)}_{ijij} &= (8.25\,\epsilon + 12\,\tau)\ e^{2\imath(\psi_i - \psi_j)},\\
h^{(6)}_{ijil} &= -\,(7.5\,\epsilon + 24\,\tau)\ e^{\imath 3\psi_i}, & h^{(6)}_{iljl} &= (7.5\,\epsilon + 24\,\tau)\ e^{3\imath(\psi_i + \psi_j)},\\
h^{(6)}_{ijll} &= (16.5\,\epsilon + 96\,\tau)\ e^{\imath(\psi_i - \psi_j)}, & h^{(6)}_{ijjl} &= -\,(16.5\,\epsilon + 96\,\tau)\ e^{-\imath(2\psi_i + \psi_j)}\\
h^{(6)}_{iijl} = h^{(6)}_{ijli} &= -\,(16.5\,\epsilon + 96\,\tau)\ e^{\imath(\psi_i + 2\psi_j)}
\end{aligned}$$

Stability matrix

In this appendix we state the stability matrix M, defined by

$$\partial_t \begin{pmatrix} \mathrm{Re}A_i \\ \mathrm{Re}A_{i^-} \\ \mathrm{Im}A_i \\ \mathrm{Im}A_{i^-} \end{pmatrix} = M \begin{pmatrix} \mathrm{Re}A_i \\ \mathrm{Re}A_{i^-} \\ \mathrm{Im}A_i \\ \mathrm{Im}A_{i^-} \end{pmatrix} = \begin{pmatrix} M1 & M2 \\ M3 & M4 \end{pmatrix} \begin{pmatrix} \mathrm{Re}A_i \\ \mathrm{Re}A_{i^-} \\ \mathrm{Im}A_i \\ \mathrm{Im}A_{i^-} \end{pmatrix}$$

for the uniform solutions Eq. (60). We separate the uncoupled contributions from the inter-map coupling contributions i.e. $M1 = M1^{(u)} + M1^{(\alpha)}$. The uncoupled contributions are given by

$$M1^{(u)} = r_z\mathbf{I} + \mathcal{A}^2 \begin{pmatrix}
-13 & -3 & 3 & -2c & -3c - \sqrt{3}s & 3c - \sqrt{3}s \\
-3 & -23/2 & 0 & -3c - \sqrt{3}s & -2c & 0 \\
3 & 0 & -23/2 & 3c - \sqrt{3}s & 0 & -2c \\
-2c & -3c - \sqrt{3}s & 3c - \sqrt{3}s & -12 - \cos 2\Delta & -2 - 2u & 2 + 2v \\
-3d + \sqrt{3}s & -2d & 0 & -2 - 2u & -12 - \cos(2\Delta + 10\pi/3) & -4d^2 \\
3c - \sqrt{3}s & 0 & -2c & -2 - 2v & -4s^2 & -12 + u
\end{pmatrix}$$

$$M2^{(u)} = \mathcal{A}^2 \begin{pmatrix}
0 & \sqrt{3} & \sqrt{3} & 2s & 2\cos(\Delta - \pi/6) & 2\cos(\Delta + \pi/6) \\
\sqrt{3} & \sqrt{3}/2 & 0 & 2\cos(\Delta - \pi/6) & 2s & 4s \\
\sqrt{3} & 0 & -\sqrt{3}/2 & 2\cos(\Delta + \pi/6) & 4s & 2s \\
-2s & \sqrt{3}d - 3s & \sqrt{3}d + 3s & -\sin 2\Delta & 2x & 2y \\
\sqrt{3}d - 2s & -2d & 0 & 2x & y & 2\sin 2\Delta \\
\sqrt{3}d + 3s & 0 & -2s & 2y & 2\sin 2\Delta & -x
\end{pmatrix}$$

$$M3^{(u)} = \mathcal{A}^2 \begin{pmatrix}
0 & \sqrt{3} & \sqrt{3} & 2s & 2\cos(\Delta - \pi/6) & 2\cos(\Delta + \pi/6) \\
\sqrt{3} & \sqrt{3}/2 & 0 & 2\cos(\Delta - \pi/6) & 2s & 4s \\
\sqrt{3} & 0 & -\sqrt{3}/2 & 2\cos(\Delta + \pi/6) & 4s & 2s \\
-2s & \sqrt{3}c - 3s & \sqrt{3}c + 3s & -\sin 2\Delta & 2x & 2y \\
\sqrt{3}d - 3s & -2s & 0 & 2x & y & 2\sin 2\Delta \\
\sqrt{3}c + 3s & 0 & -2s & 2y & 2\sin 2\Delta & -x
\end{pmatrix}$$

$$M4^{(u)} = r_z\mathbf{I}{+}\mathcal{A}^2 \begin{pmatrix} -11 & -1 & 1 & -2c & 2w & 2z \\ -1 & -25/2 & -4 & 2w & -2c & -4c \\ 1 & -4 & -25/2 & 2z & -4c & -2c \\ -2c & 2w & 2z & -12+\cos 2\Delta & 2(u-1) & 2(1+v) \\ 2w & -2c & -4c & 2(u-1) & -12+\cos(2\Delta+10\pi/3) & -4c^2 \\ 2z & -4c & -2c & 2(v+1) & -4c^2 & -12+\cos(2\Delta+8\pi/3)\,, \end{pmatrix}$$

where $\mathbf{I}$ denotes the 6×6 identity matrix and $s = \sin\Delta, c = \cos\Delta, u = \sin(2\Delta+, \pi/6), v = \sin(2\Delta - \pi/6), x = \cos(2\Delta + \pi/6), y = \cos(2\Delta - \pi/6), w = \sin(\Delta - \pi/6), z = \sin(\Delta + \pi/6)$.
The coupling part in case of the low order product-type inter-map coupling energy is given by

$$M1^{(\alpha)} = \alpha \begin{pmatrix} -(6\mathcal{B}^2+\delta^2) & 2\mathcal{B}^2 & -2\mathcal{B}^2 & -\mathcal{B}^2 & 2\mathcal{B}(\mathcal{B}-\delta) & -2\mathcal{B}(\mathcal{B}-\delta) \\ 2\mathcal{B}^2 & -(6\mathcal{B}^2+\delta^2) & 2\mathcal{B}^2 & 2\mathcal{B}(\mathcal{B}-\delta) & -\mathcal{B}^2 & 2\mathcal{B}(\mathcal{B}-\delta) \\ -2\mathcal{B}^2 & 2\mathcal{B}^2 & -(6\mathcal{B}^2+\delta^2) & 2\mathcal{B}(-\mathcal{B}+\delta) & 2\mathcal{B}(\mathcal{B}-\delta) & -\mathcal{B}^2 \\ -\mathcal{B}^2 & 2\mathcal{B}(\mathcal{B}-\delta) & -2\mathcal{B}(\mathcal{B}-\delta) & -(6\mathcal{B}^2+\delta^2) & 2\mathcal{B}^2 & -2\mathcal{B}^2 \\ 2\mathcal{B}^2(\mathcal{B}-\delta) & -\mathcal{B}^2 & 2\mathcal{B}(\mathcal{B}-\delta) & 2\mathcal{B}^2 & -(6\mathcal{B}^2+\delta^2) & 2\mathcal{B}^2 \\ 2\mathcal{B}(-\mathcal{B}+\delta) & 2\mathcal{B}(\mathcal{B}-\delta) & -\mathcal{B}^2 & -2\mathcal{B}^2 & 2\mathcal{B}^2 & -(6\mathcal{B}^2+\delta^2) \end{pmatrix}$$

$M4^{(\alpha)} = M1^{(\alpha)}, M2^{(\alpha)} = M3^{(\alpha)} = 0$.
The coupling part in case of the low order gradient-type inter-map coupling energy is given by

$$M1^{(\beta)} = \beta\mathcal{B}^2 \begin{pmatrix} 3 & -5/4 & 5/4 & 1 & -5/4 & 5/4 \\ -5/4 & 3 & -5/4 & -5/4 & 1 & -5/4 \\ 5/4 & -5/4 & 3 & 5/4 & -5/4 & 1 \\ 1 & -5/4 & 5/4 & 3 & -5/4 & 5/4 \\ -5/4 & 1 & -5/4 & -5/4 & 3 & -5/4 \\ 5/4 & -5/4 & 1 & 5/4 & -5/4 & 3 \end{pmatrix}$$

$M4^{(\beta)} = M1^{(\beta)}, M2^{(\beta)} = M3^{(\beta)} = 0$.
The coupling part of the high order gradient-type coupling energy is given by
The stationary amplitudes $\mathcal{A}$ are given in Eq. (63), Eq. (68), Eq. (81), and Eq. (83). The stationary amplitudes $\mathcal{B}$ and the constant δ are given by Eq. (116) and Eq. (94), respectively.

References

1. Kaschube M, Schnabel M, Löwel S, Coppola DM, White LE, et al. (2010) Universality in the evolution of orientation columns in the visual cortex. Science 330: 1113–1116.

2. Swindale NV (1982) A model for the formation of orientation columns. Proc R Soc Lond B 215: 211–230.

3. Adams DL, Horton JC (2003) Capricious expression of cortical columns in the primate brain. Nature Neuroscience 6.

4. Horton JC, Adams DL (2005) The cortical column: a structure without a function. Phil Trans R Soc B 360: 837–862.

5. Koulakov AA, Chklovskii DB (2001) Orientation preference patterns in mammalian visual cortex: A wire length minimization approach. Neuron 29: 519–527.

6. Koulakov AA, Chklovskii DB (2002) Direction of motion maps in the visual cortex: a wire length minimization approach. Neurocomputing 44-46: 489–494.
7. Swindale NV (1991) Coverage and the design of striate cortex. Biol Cybern 65: 415–424.
8. Swindale NV (2000) How many maps are there in visual cortex? Cereb Cortex 10: 633–634.
9. Swindale NV (1996) The development of topography in the visual cortex: A review of models. Network 7.
10. Swindale NV (2004) How different feature spaces may be represented in cortical maps. Network: Comput Neural Syst 15: 217–242.
11. Farley BJ, Yu H, Jin DZ, Sur M (2007) Alteration of visual input results in a coordinated reorganization of multiple visual cortex maps. J Neurosci 27: 10299–10310.
12. Yu H, Farley BJ, Jin DZ, Sur M (2005) The coordinated mapping of visual space and response features in visual cortex. Neuron 47: 267–280.
13. Goodhill GJ, Cimponeriu A (2000) Analysis of the elastic net model applied to the formation of ocular dominance and orientation columns. Comput Neural Syst 11: 153–168.
14. Carreira-Perpinan MA, Lister RJ, Goodhill GJ (2005) A computational model for the development of multiple maps in primary visual cortex. Cereb Cortex 15: 1222–1233.
15. Erwin E, Obermayer K, Schulten K (1995) Models of orientation and ocular dominance columns in the visual cortex: A critical comparison. Neural Computation 7: 425–468.
16. Obermayer K, Blasdel GG, Schulten K (1992) Statistical-mechanical analysis of self-organization and pattern formation during the development of visual maps. Phys Rev A 45: 7568–7589.
17. Bednar JA, Miikkulainen R (2006) Joint maps for orientation, eye, and direction preference in a self-organizing model of V1. Neurocomputing 69: 1272–1276.
18. Hübener M, Shoham D, Grinwald A, Bonhoeffer T (1997) Spatial relationships among three columnar systems in cat area 17. J Neurosci 17: 9270–9284.
19. Löwel S, Schmidt KE, Kim DS, Wolf F, Hoffsümmer F, et al. (1998) The layout of orientation and ocular dominance domains in area 17 of strabismic cats. Eur J Neurosci 10: 2629–2643.
20. Obermayer K, Blasdel GG (1993) Geometry of orientation and ocular dominance columns in monkey striate cortex. J Neurosci 13: 4114–4129.
21. Bartfeld E, Grinwald A (1992) Relationships between orientation-preference pinwheels, cytochrome oxidase blobs, and ocular-dominance columns in primate striate cortex. PNAS 89: 11905–11909.
22. Engelmann R, Crook JM, Löwel S (2002) Optical imaging of orientation and ocular dominance maps in area 17 of cats with convergent strabismus. Visual Neuroscience 19: 39–49.
23. Xu X, Bosking WH, White LE, Fitzpatrick D, Casagrande VA (2005) Functional organization of visual cortex in the prosimian bush baby revealed by optical imaging of intrinsic signals. J Neurophysiol 94: 2748–2762.
24. Carreira-Perpinan MA, Goodhill GJ (2002) Are visual cortex maps optimized for coverage? Neural Computation 14: 1545–1560.

25. Ohki K, Chung S, Kara P, Hübener M, Bonhoeffer T, et al. (2006) Highly ordered arrangement of single neurons in orientation pinwheels. Nature 442: 925.

26. Shmuel A, Grinwald A (2000) Coexistence of linear zones and pinwheels within orientation maps in cat visual cortex. PNAS 97: 5568–5573.

27. Rao SC, Toth LJ, Sur M (1997) Optically imaged maps of orientation preference in primary visual cortex of cats and ferrets. J Comp Neurol 387: 358–370.

28. Obermayer K, Blasdel GG (1997) Singularities in primate orientation maps. Neural Computation 9: 555–575.

29. Müller T, Stetter M, Hübener M, Sengpiel F, Bonhoeffer T, et al. (2000) An analysis of orientation and ocular dominance patterns in the visual cortex of cats and ferrets. Neural Computation 12: 2573–2595.

30. Bonhoeffer T, Kim DS, Malonek D, Shoham D, Grinwald A (1995) Optical imaging of the layout of functional domains in area 17 and across the area 17/18 border in cat visual cortex. Eur J Neurosci 7: 1973–1988.

31. Wolf F, Geisel T (1998) Spontaneous pinwheel annihilation during visual development. Nature 395: 73–78.

32. Cho MW, Kim S (2004) Understanding visual map formation through vortex dynamics of spin hamiltonian models. Phys Rev Lett 92: 018101.

33. Hoffsümmer F, Wolf F, Geisel T, Löwel S, Schmidt KE (1996) Sequential bifurcation and dynamical rearrangement of columnar patterns during cortical development. Comput Neural Syst .

34. Hoffsümmer F, Wolf F, Geisel T, Löwel S, Schmidt KE (1995) Sequential bifurcation of orientation– and ocular dominance maps. Paris: EC2 & Cie, p. 535.

35. Hoffsümmer F, Wolf F, Geisel T, Schmidt KE, Löwel S (1997) Sequential emergence of orientation– and ocular dominance maps. In: Elsner N, Menzel R, editors, Learning and Memory, Proceedings of the 23rd Göttingen Neurobiology Conference 1995. Stutttgart: Thieme Verlag, p. 97.

36. Lee HY, Yahyanejad M, Kardar M (2003) Symmetry considerations and development of pinwheels in visual maps. PNAS 100: 16036–16040.

37. Reichl L, Löwel S, Wolf F (2009) Pinwheel stabilization by ocular dominance segregation. Phys Rev Lett 102: 208101.

38. Cross MC, Hohenberg PC (1993) Pattern formation outside of equilibrium. Rev Mod Phys 65: 851–1112.

39. Cross MC, Greenside H (2009) Pattern Formation and Dynamics in Nonequilibrium Systems. Cambride University Press.

40. Braitenberg V, Schütz A (1998) Cortex: Statistics and Geometry of Neuronal Connectivity. Berlin: Springer.

41. Bressloff PC, Cowan JD, Golubitsky M, Thomas PJ, Wiener MC (2002) What geometric visual hallucinations tell us about the visual cortex. Neural Computation 14: 473–491.

42. Thomas PJ, Cowan JD (2004) Symmetry induced coupling of cortical feature maps. Phys Rev Lett 92: 188101.

43. Shmuel A, Grinwald A (1996) Functional organization for direction of motion and its relationship to orientation maps in cat area 18. J Neurosci 16: 6945–6964.

44. Li Y, Fitzpatrick D, White LE (2006) The development of direction selectivity in ferret visual cortex requires early visual experience. Nature Neuroscience 9: 676–681.

45. Hubel DH, Wiesel TN (1977) Functional architecture of macaque monkey visual cortex. Proc R Soc London 198: 1–59.

46. Issa NP, Trepel C, Stryker MP (2000) Spatial frequency maps in cat visual cortex. J Neurosci 15: 8504–8514.

47. Chapman B, Gödeke I (2002) No On-Off maps in supragranular layers of ferret visual cortex. J Neurophysiol 88: 2163–2166.

48. Busse FH (1978) Non-linear properties of thermal convection. Rep Prog Phys 41: 1929–1967.

49. Bodenschatz E, Pesch W, Ahlers G (2000) Recent developments in Rayleigh-Bénard convection. Annu Rev Fluid Mech 32: 709–778.

50. Soward A (1985) Bifurcation and stability of finite amplitude convection in a rotating layer. Physica D 14: 227–241.

51. Zhang W, Vinals J (1997) Pattern formation in weakly damped parametric surface waves. J Fluid Mech 336: 301–330.

52. Wolf F (2005) Symmetry breaking and pattern selection in visual cortical development. Les houches 2003 lecture notes. Methods and Models in neurophysics. Amsterdam: Elsevier.

53. Mermin ND (1979) The topological theory of defects in ordered media. Rev Mod Phys 51: 591–648.

54. Wolf F, Pawelzik K, Scherf O, Geisel T, Löwel S (2000) How can squint change the spacing of ocular dominance columns? J Physiol 94: 525–537.

55. Swift JB, Hohenberg PC (1977) Hydrodynamic fluctuations at the convective instability. Phys Rev A 15: 319–328.

56. Mannevile P (1990) Dissipative Structures and Weak Turbulence. Academic Press.

57. Schnabel M (2008) A Symmetry of the Visual World in the Architecture of the Visual Cortex. Ph.D. thesis, Göttingen University.

58. Kaschube M, Wolf F, Geisel T, Löwel S (2002) Genetic influence on quantitative features of neocortical architecture. J Neurosci 22: 7206–7217.

59. Kaschube M, Wolf F, Puhlmann M, Rathjen S, Schmidt KE, et al. (2003.) The pattern of ocular dominance columns in cat primary visual cortex: Intra- and interindividual variability of column spacing and its dependence on genetic background. Eur J Neurosci 18: 3251–3266.

60. Braitenberg V, Braitenberg C (1979) Geometry of orientation columns in the visual cortex. Biol Cybern : 179–186.

61. Cho MW, Kim S (2005) Different ocular dominance map formation influenced by orientation preference columns in visual cortices. Phys Rev Lett 94: 068701.

62. Grossberg S, Olson SJ (1994) Rules for the cortical map of ocular dominance and orientation columns. Neural Networks 7: 883–894.

63. Nakagama H, Tani T, Tanaka S (2006) Theoretical and experimental studies of relationship between pinwheel centers and ocular dominance columns in the visual cortex. Neuroscience Research 55: 370–382.

64. Pierre DM (1997) Modeling Orientation and Ocular Dominance Columns in the Visual Cortex. Ph.D. thesis, MIT.

65. Crair MC, Ruthazer ES, Gillespie DC, Stryker MP (1997) Ocular dominance peaks at pinwheel center singularities of the orientation map in cat visual cortex. J Neurophysiol 77: 3381–3385.

66. Matsuda Y, Ohki K, Saito T, Ajima A, Kim DS (2000) Coincidence of ipsilateral ocular dominance peaks with orientation pinwheel centers in cat visual cortex. NeuroReport 11: 3337–3343.

67. Das A, Gilbert CD (1997) Distortions of visuotopic map match orientation singularities in primary visual cortex. Nature 387: 594–598.

68. Mitchison GJ, Swindale NV (1999) Can hebbian volume learning explain discontinuities in cortical maps? Neural Computation 11: 1519–1526.

69. Löwel S, Singer W (1990) Tangential intracortical pathways and the development of iso-orientation bands in cat striate cortex. Brain Research 56: 99–106.

70. Bosking WH, Zhang Y, Schofield B, Fitzpatrick D (1997) Orientation selectivity and the arrangement of horizontal connections in tree shrew striate cortex. J Neurosci 17: 2112–2127.

71. Durbin R, Mitchison GJ (1990) A dimension reduction framework for understanding cortical maps. Nature 343: 644–647.

72. Crair MC, Gillespie DC, Stryker MP (1998) The role of visual experience in the development of columns in cat visual cortex. Science 279: 556–570.

73. Issa NP, Trachtenberg JT, Chapman B, Zahs KR, Stryker MP (1999) The critical period for ocular dominance plasticity in the ferret's visual cortex. J Neurosci 19: 6965–6978.

74. Horton JC, Hocking DR (1996) Intrinsic variability of ocular dominance column periodicity in normal macaque monkeys. J Neurosci 16: 7228–7339.

75. Chklovskii DB, Koulakov AA (2000) A wire length minimization approach to ocular dominance patterns in mammalian visual cortex. Physica A 284: 318–334.

76. Swindale NV, Shoham D, Grinwald A, Bonhoeffer T, Hübener M (2000) Visual cortex maps are optimized for uniform coverage. Nature Neuroscience 3: 822–826.

77. Swindale NV, Shoham D, Grinwald A, Bonhoeffer T, Hübener M (2002) Reply to carreira-perpinan and goodhill. are visual cortex maps optimized for coverage? Neural Computation 14: 2053–2056.

78. Miller KD (2010) $\pi =$ visual cortex. Science 330: 1059–1060.

79. Wolf F (2005) Symmetry, multistability and long-range interactions in brain development. Phys Rev Lett 95: 208701.

80. von der Malsburg C (1973) Self-organization of orientation sensitive cells in the striate cortex. Kybernetik 14: 85–100.

81. Brabska-Barwinska A, von der Malsburg C (2008) Establishment of a scaffold for orientation maps in primary visual cortex of higher mammals. J Neurosci 28: 249–257.

82. Huang M (2009) Spatio-Temporal Dynamics of Pattern Formation in the Cerebral Cortex. Ph.D. thesis, Göttingen University.

83. Brown PN, Saad Y (1990) Hybrid Krylov methods for nonlinear systems of equations. J Sci and Stat Comput 11: 450–481.

84. E DJ, Schnabel RB (1983) Numerical Methods for Unconstrained Optimization and Nonlinear Equations. Prentice-Hall.

85. Balay S, Buschelman K, Gropp WD, Kaushik D, Knepley MG, et al. (2001). PETSc Web page. URL `http://www.mcs.anl.gov/petsc/petsc-as/`.

86. Press WH (1992) Numerical recipes in C: The art of scientific computing. Cambridge University Press.

List of Figures